Real-time scanning tunneling microscopy studies of thin film deposition and ion erosion

Fokkema, V.

Citation

Fokkema, V. (2011, November 10). *Real-time scanning tunneling microscopy studies of thin film deposition and ion erosion*. Retrieved from https://hdl.handle.net/1887/18057

Version:	Not Applicable (or Unknown)
License:	[Leiden University Non-exclusive license](#)
Downloaded from:	[https://hdl.handle.net/1887/18057](#)

Real-time Scanning Tunneling Microscopy Studies

of

Thin Film Deposition and Ion Erosion

Real-time Scanning Tunneling Microscopy Studies
of
Thin Film Deposition and Ion Erosion

Proefschrift

ter verkrijging van
de graad van Doctor aan de Universiteit Leiden,
op gezag van Rector Magnificus prof. mr. P. F. van der Heijden,
volgens besluit van het College voor Promoties
te verdedigen op donderdag 10 november 2011
klokke 12.30 uur

door

Vincent Fokkema

geboren te Vlaardingen
in 1982

Promotiecommissie

Promotor:
Prof. dr. J. W. M. Frenken
Universiteit Leiden

Co-promotor:
Dr. M. J. Rost
Universiteit Leiden

Overige leden:
Prof. dr. F. Bijkerk
FOM-Instituut voor Plasmafysica Rijnhuizen / Universiteit Twente

Prof. dr. E. R. Eliel
Universiteit Leiden

Prof. dr. T. Michely
Universität zu Köln, Duitsland

Dr. ir. S. J. van der Molen
Universiteit Leiden

Dr. G. Palasantzas
Rijksuniversiteit Groningen

Prof. dr. ing. A. J. H. M. Rijnders
Universiteit Twente

Prof. dr. ir. M. C. M. van de Sanden
FOM-Instituut voor Plasmafysica Rijnhuizen / Technische Universiteit Eindhoven

Prof. dr. ir. H. J. W. Zandvliet
Universiteit Twente

aan mijn ouders, aan Caroline

Contents

Introduction and outline

A *thin film* [1] is a layer of material, of which the thickness ranges between atomic dimensions, i.e. a fraction of a nanometer, and several micrometers. The variety of unique electrical, optical, mechanical, and magnetic properties of thin film systems is reflected in the broad spectrum of their applications. As examples, anti-reflection coatings on glasses and telescopes are thin film systems [2] and so are the gold coloured titanium-nitride films applied to harden the surface of special tools [3]. Thin film technology is also important for the fabrication of interconnects in integrated circuits [4] and for mass storage devices [5].

The suitability of a thin film for a certain application depends not only on the choice of the material, but also on its morphology: the microstructure of the film determines important properties, such as the electrical conductivity, the hardness, and the smoothness of the surface. The morphology of a thin film depends critically on the specific production process, which includes both the deposition and the post-deposition processing of the film. Ideally, by controlling the morphology of a thin film, one would like to tune its properties for each specific application.

The research described in this thesis was focused on two processes that are important for thin film technology:

- the growth of thin films by material deposition onto a substrate, and
- the modification of thin films and substrates induced by ion bombardment.

The thin film system that plays a central role in this thesis, is the layered structure of alternating molybdenum and silicon thin films. Mo-Si *multilayer* systems are used as reflective optics for applications, in which conventional lenses and mirrors cannot be used due to the small wavelength of the radiation [2]. The thickness of a single layer in a Mo-Si multilayer structure is only a few nanometers; the total number of layers is typically 100. The critical properties of a layer in a multilayer mirror are its precise thickness, which is closely related to the wavelength of the radiation, and its density, which determines the refractive index of the film. Furthermore, the optimal reflectivity of Mo-Si multilayer optics requires sharp transitions between the layers, which is compromised by the following. During the deposition of a layer, the deposited material reacts with the material onto which it is deposited. This results in the formation of a molybdenum-silicide interlayer. Additionally, the reflectivity of a multilayer system is lower than the theoretical optimum due the roughness of the interfaces between the layers, which is the result of the surface roughness that evolves during the deposition of a single layer.

To study the morphology of a thin film, there are a number of analytical methods, such as various microscopy and X-ray techniques. The experiments described in this thesis were performed by using a microscope, which ranks amongst the highest in terms of the level of magnification in real-space: the *scanning tunneling microscope* (STM). This type of microscope enables its user to visualize a surface at the scale of single atoms.

If one seeks to control the morphology of a thin film, it is of great help if one has a fundamental understanding of the production process. In principle, the STM is suited to investigate the atomic processes that govern the evolution of the film morphology, but there is one major drawback. Due to the specific architecture and operating principle of the STM, it is difficult to study the key steps of the production of thin films *during* the process. Hence, almost all STM studies of thin films are executed by using a *post-process* type of approach, i.e. an image of the surface of the film is obtained *after* its fabrication. A disadvantage of this *modus operandi* is that it does not yield direct insight into the atomic details of the process. If thin film growth or modification is studied with the STM at various stages by interrupting the process, it is almost impossible to follow the changes of the exact same area, so that information is obtained only about how the statistics of the surface evolve, rather than how specific features change during the process. Furthermore, the morphology can change between the production of the film and the STM investigation.

To be able to directly investigate the atomic processes that determine the morphology of thin films, a novel STM setup dedicated to imaging thin film deposition and ion erosion *during* these processes, has been developed. The application of this new instrument resulted in a series of unique, *real-time STM studies of thin film deposition and ion erosion*. The microscope and the research it has enabled, are presented in this thesis.

Chapter 1 provides some background information on concepts that are relevant for the research described in this thesis.

In Chapters 2 and 3 the focus is on the instrumentation development. Chapter 2 serves to present the new setup as a whole, which includes the STM, the UHV chamber, and the peripheral equipment, required for the real-time experiments. Within the boundaries set by the required ability to image during growth and erosion, the STM was optimized for fast data acquisition, by using finite element analysis calculations of the structural mechanics of the design. An account of the calculations of the mechanical rigidity of the STM scanner, which is required for high-speed, stable imaging, is given in Chapter 3.

The new STM was put to the test in a series of growth and erosion experiments, which are presented in Chapters 4 to 7. These experiments demonstrate the power of real-time STM, as we have been able to draw conclusions on the basis of analyses that would not have been possible from post-process studies.

We report on the *live* observation of the deposition of Mo onto Si, focusing on the initial stages in Chapter 4. This offers insight into the atomic processes that govern Mo-silicide formation, the knowledge of which is important for Mo-Si multilayer optics. The growth of a complete Mo layer, including the determination of the fundamental origin of the evolution of its roughness, is the subject of Chapter 5.

In Chapter 6 the study of an ion induced surface erosion of a Si substrate is presented. To our knowledge this is the very first STM investigation executed *during* ion bombardment. This particular experiment, in which we recorded the erosion on a single-ion-impact level, may lead the way to a detailed understanding of ion induced pattern formation. Finally, we have used the new STM to investigate, again in a *real-time* experiment, the smoothing of a Mo film by means of ion bombardment, which is the subject of Chapter 7. The roughness of the film can be significantly and efficiently reduced when the ions strike the surface at a large angle with respect to the surface normal. Therefore, the conclusion is reached that the post-deposition, grazing incidence ion bombardment of the Mo layers in Mo-Si multilayer optics may very well be a reflectivity enhancing step in the multilayer production process.

CHAPTER 1

Background

Some general concepts that are important throughout this thesis, are introduced in this chapter. Selected methods and techniques in thin film technology are presented, followed by a short introduction to Mo-Si multilayer optics. The operation principle of scanning tunneling microscopy, the main experimental technique that was used in the experiments described in this thesis, is briefly explained in the final section of the chapter.

1.1 Thin film technology

Thin films are commonly produced by the deposition of material onto a substrate. Physical vapour deposition (PVD) requires the generation of a vapour from a target, which is directed at the substrate [6]. Deposition by evaporation is done by heating the target in vacuum, thereby increasing its vapour pressure. A widely used form of thermal deposition is e-beam evaporation, in which an electron beam, originating from a hot cathode, is directed at the target, the anode. Due to a high anode-cathode voltage, the target is locally heated very efficiently. The deposition experiments in this thesis were performed by using this technique. Another important PVD process is sputter deposition, which follows from the ejection of atoms from a target as a result of the impact of energetic ions onto the target. A third PVD technique is pulsed laser deposition (PLD). In the process of PLD, an intense laser pulse with a duration of nanoseconds and a *fluence* of ~ 1 J cm^{-2}, is used to ablate material from a target. Other thin film deposition techniques include electroplating [7], which is the deposition of metals from an electrolyte, and chemical vapour deposition (CVD) [8]. The latter involves the decomposition reaction of a precursor gas, e.g. a hydride or halide of the material to be deposited, on a substrate at elevated temperatures.

Most thin films have a polycrystalline morphology and hence comprise many crystalline *grains* [9]. Where these crystallites meet, *grain boundaries* are formed. The properties of a grain boundary depend on the difference in crystallographic orientation of the two adjacent grains. Often there is one dominating grain orientation in a polycrystalline thin film, which defines the *texture* of the film. Many properties of a polycrystalline film, such as its electrical conductivity, hardness, ductility, and surface roughness are strongly influenced by the texture of the film, the grain size, and the grain boundary network.

The morphology of a polycrystalline film, does not only depend on the specific deposition method, but also on the deposition rate, the substrate temperature, and the vacuum conditions during fabrication, as well as on the choice of the specific substrate. A phenomenological classification of the structure of polycrystalline films on the basis of the deposition conditions is provided by the so-called *zone models* [10–13], which only limitedly shed light on the atomic processes that determine the specific morphology.

After the deposition of a thin film, its morphology may be altered by the *annealing* of the film, which is a heat treatment that induces grain growth and reorientation, changes the internal stress of the film, and alters the surface roughness [14]. Another important means of modifying the properties of thin films is achieved by ion induced erosion [15]. Ion erosion is the result of the bombardment of the film with energetic ions. Following the impact, a certain amount of energy is dissipated in a thin region below the surface. The consequence of this energy release are structural changes to the morphology, by rearrangement and removal of material. The details of the erosion process depend on the type of ions, their

energy, the angle of incidence, and on the substrate temperature.

The properties of thin films can be optimized for a certain application by varying the parameters of the deposition and post-deposition processes. A trial-and-error type of optimization can yield significant improvements, but the 'perfect' production routine often requires the understanding of the various processes and underlying mechanisms on a fundamental level. An example of a thin film system, of which the fabrication procedure has been optimized by engineers and scientists over the passed decades, both by trial-and-error, as well as through fundamental research, is the Mo-Si multilayer mirror. The state of the art of the production of this type of optical coating is such that its performance nears perfection, but in order to be able to produce the ultimate Mo-Si multilayer mirror some issues need to be resolved.

1.2   Mo-Si multilayer optics

The continual downscaling of the size of integrated circuits requires ongoing improvement of the (nano)lithographic production process in order to be able to produce the ever-smaller features [16]. The prime *next-generation lithography* technology is a photolithographic technique that relies on extreme ultraviolet (EUV) radiation with a wavelength of 13.5 nm for the illumination [17]. This technique requires the use of special reflective optics: Mo-Si multilayer mirrors [2, 18]. The multilayer stacks are produced layer by layer by alternating the deposition of Mo and Si by PVD, commonly by using e-beam or sputter deposition. Some fabrication routines incorporate the use of ion bombardment to modify deposited layers at selected stages in the production process to increase the reflectivity of the finished mirror. The typical thickness of the Mo layers is between 2.5 nm and 3.0 nm; the thickness of the Si layers is commonly larger and ranges between 3.9 nm and 4.4 nm.

A multilayer mirror is a *Bragg reflector* that relies on the constructive interference of the reflections from the layer interfaces, see Figure 1.1(a) [2]. The period p, which is the Mo-Si bilayer thickness, is given by [19]:

$$p = nK\frac{\lambda}{2\cos\theta},$$
(1.1)

in which θ is the angle of incidence with respect to the normal, λ is the wavelength, n is the order of interference, and K is a constant, which depends on the refractive indices of both materials and on the ratio between the thickness of the Mo and Si layers. For the optimal, first-order, normal incidence Mo-Si multilayer reflector the Mo layer is ~2/3 of the thickness of the Si layer, K is slightly larger than unity, and $p \approx 6.9$ nm. In general, the reflectivity of a Mo-Si multilayer mirror increases by increasing the number of bilayers. However, above ~50 bilayers, the gain in reflectivity is negligible.

The reflectivity of a multilayer system can be calculated in a straightforward manner by computing, at every interface, the amplitude of the reflected and transmitted radiation using the Fresnel equations [20, 21]. The theoretical maximum reflectivity of a Mo-Si multilayer mirror for 13.5 nm radiation, taking into account losses through absorption, is determined to be 0.74 [22, 23], see Figure 1.1(b).

In practice the reflectivity is lower, due to the fact that the boundaries between the layers are not infinitely sharp and smooth. During the fabrication process a Mo-silicide interlayer is formed that diminishes the optical contrast between the Mo and Si. In addition, the performance is reduced by the roughness of the interfaces. The reflectivity of a real multilayer can be can be calculated, again by using the Fresnel equations, but incorporating a *Debye-Waller* factor for the reflection at each interface [24]. The intensity of the reflection r at the boundaries is:

$$r = r_0 \exp\left(\frac{-16\pi^2 w^2 \cos^2\theta}{\lambda^2}\right),\tag{1.2}$$

where r_0 is the lossless reflectivity and w is either the thickness of the silicide interlayer, the root-mean-square roughness of the interface, or in the case of both being present an 'effective thickness' of the transition zone that captures both degrading effects. Another negative side effect of interface roughness is the loss of imaging contrast due to additional scattering that produces a background halo [25]. The effect of $w = 0.7$ nm, which is a typical value, leads to a reduction of the reflectivity to 0.67. Although this loss of reflectivity may seem modest, the total reflectivity of 11 mirrors in series, which is a typical configuration in an EUV lithography machine, is reduced by a factor 3 from the theoretical attainable value. Hence, a gain in reflectivity of the multilayer optics can seriously increase the throughput of a lithography machine, as the illumination time is reduced. In this thesis new light is shed on the origin of the non-idealities of the Mo-Si system, which may lead the way to an enhanced performance of Mo-Si multilayer optics.

1.3   Scanning tunneling microscopy

Scanning tunneling microscopy (STM[*]) is a microscopy technique, with which it is possible to visualize (semi-)conducting surfaces with atomic-scale resolution. The STM was invented by Binnig and Rohrer in 1981 [26, 27]; the power of the technique was quickly recognized, and in 1986 its inventors were awarded the Nobel Prize in physics[†]. The STM is part of the family of scanning probe microscopes (SPM), in which a probe, commonly termed the *tip*, is scanned

---

[*]The abbreviation STM is used for both the technique (microscopy), as well as for the instrument (microscope).

[†]Gerd Binnig and Heinrich Rohrer share their Nobel Prize with the inventor of the electron microscope, Ernst Ruska [28].
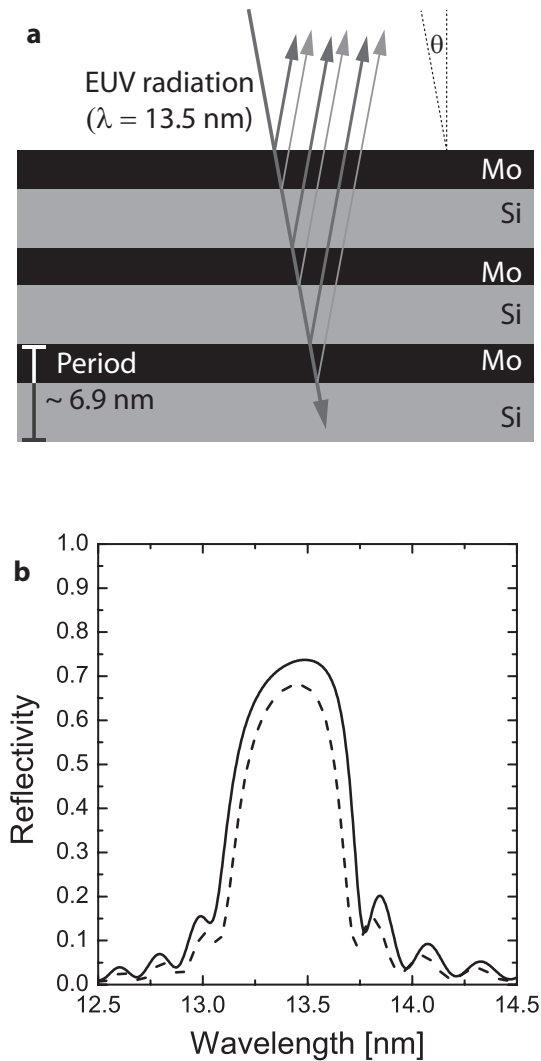
Figure 1.1: (a) A Mo-Si multilayer system is a Bragg reflector: the total reflectivity is the result of the (constructive) interference of the reflections from the boundaries of the layers. The angle of incidence of the radiation is θ. (b) The calculated reflectivity of a Mo-Si multilayer as a function of the wavelength of the reflected radiation, using [22, 23]. The solid line represents the theoretical maximum of a 6.9 nm period multilayer stack of 50 bilayers, and a volumetric Si content of 60%. The reflectivity at $\lambda = 13.5$ nm is 0.74. The dashed line shows the reduced performance, due to the fact that the interfaces are not infinitely sharp. A value for w of 0.7 nm (Equation 1.2), results in a peak reflectivity of 0.67.

across the substrate to be imaged[*]. This scanning is realized by mounting the tip on a piezoelectric scanner, which can move in all three spatial directions with great accuracy. The performance of SPM relies on the sharpness of the tip. Therefore, for STM performed in a vacuum, the tip is often made of a tungsten wire that can be etched to form a very fine tip, but oxidizes under atmospheric conditions. Alternatively, an inert, cut platinum(-iridium) wire can be used. The choice of the tip material depends on the specific application of the STM.

An image of the topography of the surface is formed on the basis of the interaction between the tip and the surface. In the case of STM, this interaction is a quantum tunneling current I_t between the tip and the sample: when the tip is brought into close proximity to the surface[†] a bias voltage V_b, applied between the tip and the sample, leads to tunneling of electrons from the tip to the sample, or *vice versa* depending on the polarity of V_b. The tunneling current depends on the tip-sample separation δ. The following equation holds approximately:

$$I_t \propto V_b \exp(-C\delta), \tag{1.3}$$

in which C is a constant that depends on both the tip and sample material. In part, the superb resolution of STM is due to the strong dependency of I_t on δ; in a typical situation the tunneling current changes by one order of magnitude if δ is changed by 0.1 nm. Although quantum tunneling does not require vacuum conditions, STM experiments are often performed in an ultra-high vacuum (UHV)[‡] to keep the surface clean during experiments.

An STM image can be acquired in various ways. The first involves a raster scan of the tip at a *constant-height* above the surface, while measuring the tunneling current as a function of the in-plane coordinates, $I_t(x, y)$. From the variations in I_t, the variations in δ can be derived that reflect the surface profile. As δ is not controlled in constant-height STM, an 'unexpected' close encounter of the tip and the sample can occur, which damages both the tip and the sample. If the tip is blunt after a *tip crash*, the resolution is lost. In addition, I_t is small for those regions where δ is large, which corresponds to a small signal-to-noise ratio and distorted images, as well as the possible loss of the tunneling junction.

More commonly, STM is operated in *constant-current* mode. Again the tip is scanned parallel to the sample, but now I_t and δ are kept constant by performing feedback on I_t. The required movement of the tip in the z-direction, to keep a constant tunneling current, reflects the height variations of the surface: the tip tracks the surface morphology. Figure 1.2 shows the principle of operation of constant-current mode STM schematically. In this mode the risks of tip crashes and the loss of the tunneling junction are minimized. In addition, as the tunneling current is constant, so is the signal-to-noise ratio during imaging. The downside of this mode of operation as opposed to constant-height STM, is that

---

[*]Alternatively, the tip is stationary and the scanning is performed by moving the sample.
[†]The typical separation between the tip and the sample during tunneling is ∼0.7 nm.
[‡]Ultra-high vacuum corresponds to a residual gas pressure below 10^{-9} mbar.
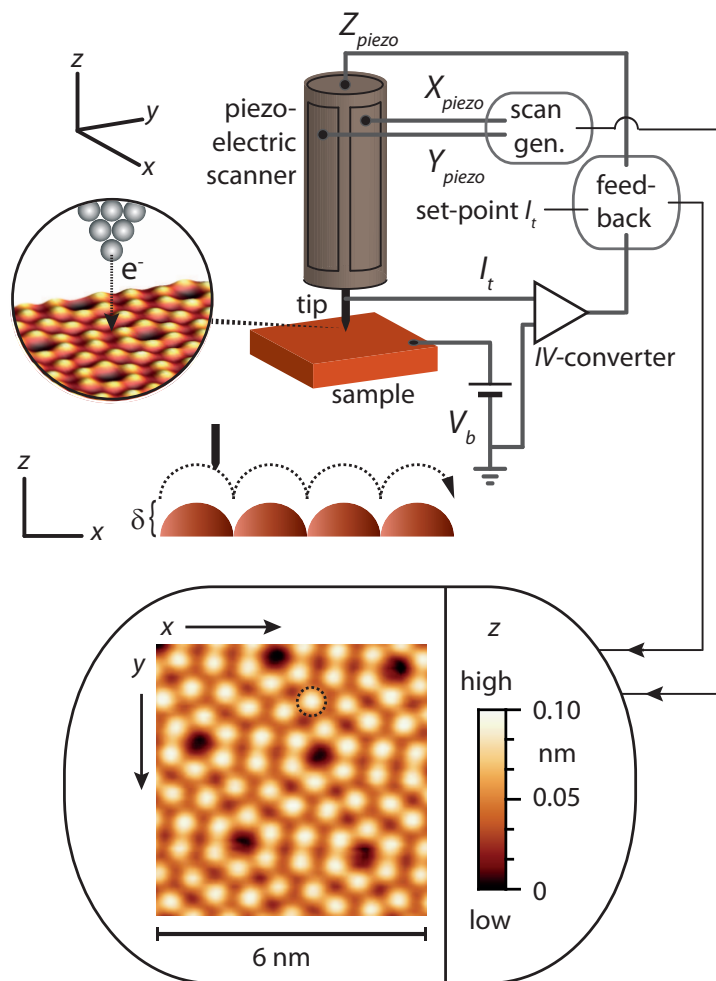
Figure 1.2: Principle of operation of STM. A sharp tip is brought near the surface to be imaged. The bias voltage V_b between tip and sample leads to a tunneling current I_t, which depends on the tip-sample separation δ. In the constant-current mode, the tip is scanned across the surface by a piezoelectric scanner, while a feedback system keeps I_t, and thus also δ, constant by adjusting the position of the tip in the z-direction. An image is formed on the basis of the x, y, z motion of the tip, and displayed most commonly as $z(x, y)$ indicated by a false colour scale. The dimensions of the image depicted here are: $6 \times 6 \times 0.1 \text{ nm}^3$. This STM image shows the surface of crystalline silicon and was obtained during one of the experiments described in this thesis; a single Si atom is encircled.

the need of z-movement of the tip slows down the imaging speed. Unless stated otherwise, the STM measurements presented in this thesis were performed in the constant-current mode.

A third STM mode, which combines the benefits of both the constant-height and constant-current mode, is the so-called *hybrid* mode [29]. This way of operation relies on a low-frequency feedback on I_t to track the global, possibly large variations of the surface height. The height 'error' that is made in this way of feedback operation can be measured accurately by measuring the high-frequency 'error' in I_t through a logarithmic amplifier. The addition of the low-frequency and the high-frequency signals provides the real surface topography with atomic resolution. The hybrid mode is ideal for high-speed STM on rough surfaces, as no high-frequency actuation of the position of the tip in the z-direction is required, while the risk of tip crashes is minimized. The challenges of the application of this relatively new technique lie in the correct choice of separating the low-frequency and high-frequency components of the tunneling current, as well as in the image forming on the basis of the different nature of the inputs.

Prior to imaging the tip and the sample must be brought within a separation of less than ~ 1 μm, which is the typical range of the piezoelectric scanner in the z-direction. This *coarse approach* procedure needs to be performed without the tip ever making contact with the sample, in order to avoid damage to either the tip or the sample. Typically, the coarse approach is done by using a stepper-motor, with a step size that is considerably smaller than the range of the piezoelectric scanner.

The difficulty of performing STM during thin film deposition and ion erosion is having access to the sample. The path from the deposition and ion sources to the part of the sample that is imaged by the tip can be obstructed by parts of the microscope, which depends on the specific architecture of the microscope. In any case, it is difficult to ensure that the tip does not block the impinging atoms or ions. The newly developed STM introduces several special 'tricks' to optimize the accessibility of the sample.

CHAPTER 2

A novel, fast STM for real-time studies

An ultra-high vacuum scanning tunneling microscope (UHV-STM), dedicated to imaging thin film deposition and ion erosion *during* these processes, has been developed. The STM has the unique property that the polar and azimuthal angles of incidence of the atoms and ions can be changed, without breaking the vacuum. Additionally, the STM was designed for fast image acquisition. The new STM and the peripheral equipment required to image during film growth and surface erosion, are presented in this chapter.

2.1   Introduction

Since its invention, the scanning tunneling microscope (STM, see Section 1.3) has been the most popular instrument to probe (semi-)conducting surfaces on the atomic-scale, in real space. Although STMs are commercially available [30], research focused on a specific topic, may require modification of an existing setup or the complete development of a new STM. In turn, these specialized instruments sometimes also find their way to the commercial market. Examples of STM setups with special features are those dedicated to the study of thermally activated processes and exhibit the capability of steady imaging at variable temperatures [31] or even during large temperature changes [32]. Other STMs have a sample stage that can be cooled to cryogenic temperatures, suited for spectroscopic studies and atom manipulation [33, 34]. Most STMs operate in ultra-high vacuum (UHV) to maintain a clean and well-defined surface and a stable tip during experiments. Other instruments are optimized for studying the evolution of surfaces under high pressure conditions to investigate catalysts in action [35], or to operate in a liquid [36], for example to investigate electro-chemistry [37].

Here, we report on the development of an STM, dedicated to studying thin film deposition and the effects of ion bombardment *during* these processes. Both film growth and ion erosion have been studied extensively with STM, but seldom in a real-time fashion. For examples of *live* observations of material deposition we refer to Refs. 38–40. To our knowledge there are no real-time STM experiments on ion bombardment induced surface erosion. The main difficulty of STM imaging during deposition or erosion is the possibility that the tip blocks the path of the atoms or ions to the sample; the design of our STM allows the optimization of the accessibility of the sample.

In contrast to the superb spatial resolution of STM stands its inherently poor temporal resolution, which originates from the scanning nature of the technique. The speed, at which the tip is moved over the surface is limited, amongst other factors, by the fact that a stable tunnel junction must be maintained throughout the imaging. This makes STM much slower than, e.g. optical microscopy, electron microscopy, or X-ray techniques; a typical STM images requires 1 minute of acquisition time. If STM is applied to studying fast surface processes that occur during deposition and erosion, evidently much is gained if the STM is optimized for fast imaging. In this chapter we present a novel, fast STM for investigating film growth and ion erosion, including the required peripheral equipment.

2.2   Fast scanning and imaging stability

Speeding up STM (and other scanning probe techniques) has been the focus of numerous studies; a recent overview of these efforts is presented in Ref. 41. The challenges one faces in increasing the imaging rate include: the finite bandwidth
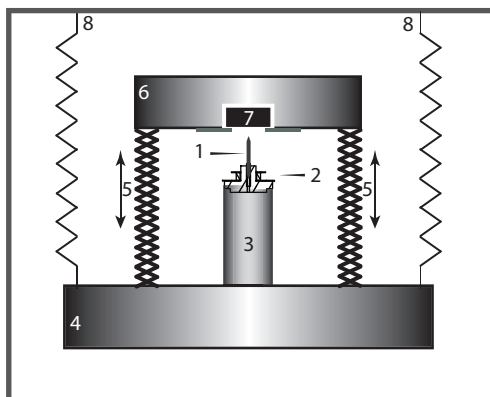
Figure 2.1: Schematic of a basic STM configuration, consisting of (1) the tip, (2) the tip-holder, (3) the piezoelectric scanner, (4) the support, (5) the coarse approach mechanism, (6) the sample-holder, and (7) the sample. The coarse approach is done by lowering the sample-holder to bring the tip and the sample within the control range of the piezoelectric scanner. For stable imaging the STM must be isolated from the environmental vibrations, which can be attained by suspending it from springs (8), thereby creating a mechanical low-pass filter. Often a series of decoupling stages is required to be able to obtain atomic resolution.

of the *IV*-converter, of the feedback system, and of the amplifiers that are used to drive the (piezoelectric) actuators, as well as the limited speed of the data acquisition, and mechanical resonances in the microscope. As the issues of electronic nature have been largely resolved [29], we will focus on the limitations that are imposed on the scanning speed by the mechanical properties.

Figure 2.1 shows a schematic drawing of a typical STM setup with the sample facing downwards; this particular orientation is required for high flux evaporation experiments, as will be explained later. Vibrations that couple into the mechanical loop, which consists of those parts of the microscope that mechanically couple the tip and the sample, can result in image distortions and, in a more dramatic case, in the loss of the tunneling junction and possibly a tip crash.

In discussing the mechanical stability of an STM, it is important to distinguish between vibrations that are introduced in the microscope internally, i.e. originating from the scanning motion of the piezoelectric scanner and those that arise from external sources, such as running pumps, building vibrations, and acoustic noise. External vibrations may constitute a problem if they result in the motion of the sample and the tip at different amplitudes or phases.

A number of solutions exists to decouple an STM from its surroundings, usually in multiple steps. The first decoupling stage is often achieved by placing the setup on a very heavy foundation [42], or on its own foundation detached from the main foundation of the laboratory [43]. In order to isolate it from mechanical

and acoustical interference, the STM descibed in Ref. 33 is even placed in a separate room that neither contains the STM control electronics nor the majority of the mechanical pumps. The second vibration isolation stage consists of the setup itself, e.g. a heavy vacuum chamber or a cryostat containing the STM, suspended from extension springs or placed on pneumatic isolators to create a mass-spring system with a low resonance frequency. This mass-spring system acts as a mechanical low-pass filter above its resonance frequency [44].

A third decoupling stage is often required to further isolate the STM from vibrations, especially when the source of these vibrations is coupled directly to the setup, as is the case for mechanical pumps in vacuum STMs. For low-temperature STMs, also the boil-off of cryogenic fluids may introduce vibrations. The first STM of Binnig *et al.* was magnetically levitated on a superconductor [26] and energy introduced into the system by environmental disturbances, was dissipated in the form of eddy-currents induced in a conductor. In modern STMs, this type of eddy-current damping is widely employed, although the STM is usually suspended from springs, rather than magnetically levitated [44].

The decoupling of an STM from its surroundings is an important step to ensure the required resolution of the microscope, but if one seeks to increase the imaging rate, the internal vibrations must be dealt with. Here it is important to distinguish between active resonances, i.e. those that occur in the piezoelectric scanner itself, and vibrations that are induced in other parts of the microscope by the scanning motion.

Controlling the scan behaviour is increasingly difficult if the resonance frequencies of the scanner are approached. The (commonly) anharmonic* nature of the scanning signal causes these resonance to become problematic at line frequencies far below the natural frequencies of the scanner [29]. It is thus clearly beneficial to raise the resonance frequencies of the scanner.

A number of important steps in this direction have been taken since the first STM that used a tripod arrangement, with 5 kHz as a lowest resonance frequency, to generate the scanning motion [27]. The introduction of the piezoelectric tube scanner [45] raised the resonance frequencies to 8 kHz in the direction parallel to the surface and to 40 kHz in the perpendicular direction. To date, the piezoelectric tube scanner is still the most applied scan-actuator in the field. The resonance frequencies of a tube can be increased by decreasing its size, but as a consequence the scan range is also reduced. A derivative of the tube scanner is the conical piezoelectric scanner [46, 47] that has optimized rigidity and maximized resonance frequencies, whilst maintaining a reasonable scan range. Rather than avoiding mechanical resonances, one could scan *at* resonance [48]. In that case, the improvement in imaging rate is accompanied by limitations on the used drive signal: only a harmonic signal at a fixed frequency is allowed.

Increasing the resonance frequencies of the piezoelectric scanner is obviously very

---

*A triangular scanning signal is commonly supplied to the scanner.

important to obtain high line frequencies, but the mechanical properties of other parts of the microscope are of importance too. The scanning motion may excite vibrations in these components. If these are part of the mechanical loop, the images become distorted and, if the amplitudes are large enough, the imaging can even become unstable. Avoiding such problems requires an integral approach, in which the vibrational characteristics are optimized of the complete mechanical loop, including the tip, the tip-holder, the piezoelectric scanner, the support on which it is mounted, the approach mechanism, the sample-holder, and the sample (see Figure 2.1). To minimize the effect of the vibrations induced by the scanning motion, as well as from external sources, the mechanical loop is best kept as compact and stiff as possible. The least rigid part in the mechanical loop is generally the approach mechanism, owing to the fact that moving parts are required. Much can be gained, if a stiff and compact mechanism is implemented. To further minimize the coupling between the piezoelectric scanner and the sample it is wise to minimize the mass ratio $m_{scanner}/m_{support}$, as the amplitude of the coupling depends on this factor. In the next sections we will present the design of our STM, which is based on these design-rules and on finite element analysis (FEA) calculations of the structural mechanics of the mechanical loop. The FEA calculations are the presented in Chapter 3.

2.3   STM scanner body and sample-holder

The newly developed STM was designed as an instrument for real-time film growth and ion erosion studies, which imposed some restrictions on the design, such as the necessity of an open structure of the microscope. This, in fact, compromises the rigidity of the mechanical loop. Furthermore, the STM must be suited for high flux deposition experiments, which leads to another boundary condition for the design, as is explained in the following. Some materials, e.g. Au, must be heated significantly above their melting point in order to have a sufficiently high vapour pressure, required for high flux deposition. Hence the preferred orientation for the deposition source is upwards and, consequently, the sample must face downwards. To optimize the rigidity and ultimately the performance of the STM, FEA calculations of the structural mechanics of the STM were performed throughout the design stage. These calculations are discussed in Chapter 3. Figure 2.2 shows the final design of the heart of the STM setup: the scanner body and sample-holder assembly; photographs of the scanner and sample-holder are shown in Figure 2.3.

The piezoelectric scanner is a tube made from EBL#2 (PZT-5A) material [49], with four outer electrodes and a single inner electrode. The outer diameter of the tube is 6.35 mm, the inner diameter is 4.83 mm, and the length is 12.7 mm. A tip-holder is glued on top of the tube. With the added length of the tip-holder and tip of ~8 mm the lateral scan range is 3×3 μm^2. The maximum deflection of the tip in the x-direction or the y-direction is attained when on one of the outer
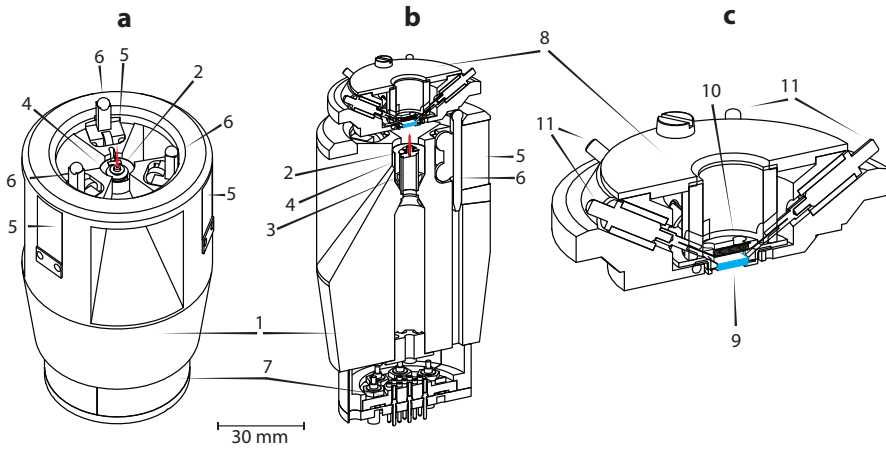
Figure 2.2: (a) Scanner body, (b) cross-section of the body and sample-holder, and (c) cross-section of the sample-holder. The components are: (1) body, (2) tip-holder and tip, (3) piezoelectric scanner, (4) shield to protect the piezoelectric scanner from the evaporation and sputtering sources, (5) approach motors, (6) moving bars of (5), (7) connector, (8) sample-holder, (9) sample, (10) filament to heat (9) from the back, and (11) electrical connections to the sample-holder.
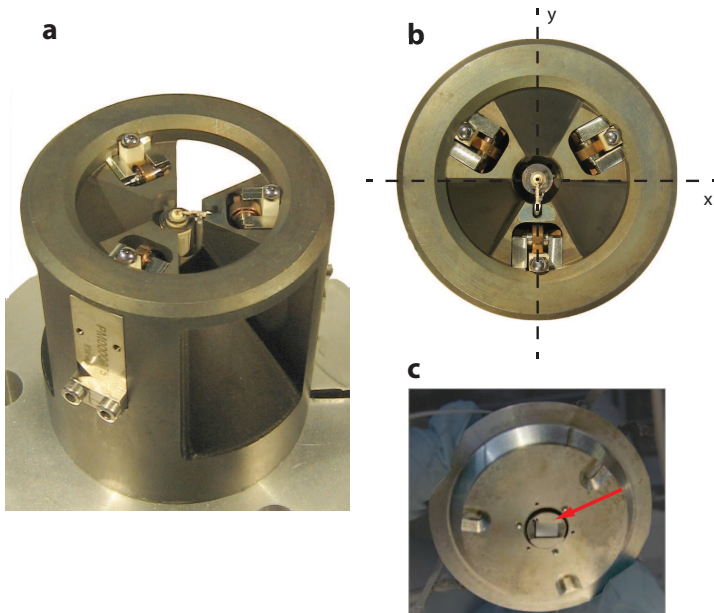
Figure 2.3: (a) Photograph of the STM scanner body. (b) Top-view of the scanner body. (c) Photograph of the bottom of the sample-holder; the sample is placed in a 'cup' (indicated by the arrow), which is electrically isolated from the sample-holder.
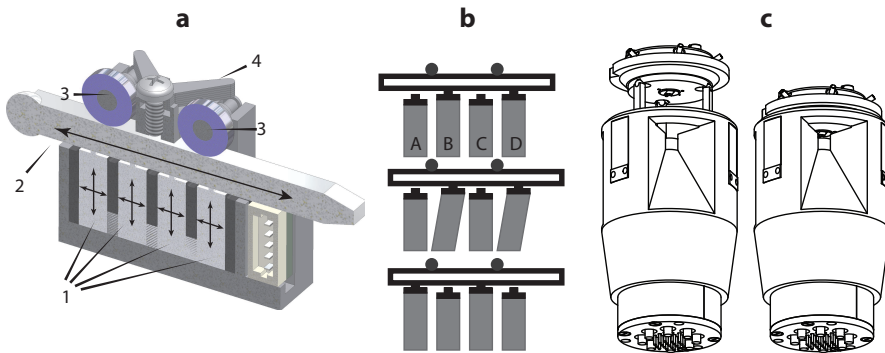
Figure 2.4: (a) Drawing of the piezoelectric motor that is used as an approach motor in the STM scanner body. Four piezoelectric elements (1) can move up-down and left-right independently. A ceramic bar (2) is positioned between (1) and two rolling bearings (3); Components (1), (2), and (3) are pressed together by a spring (4). (b) Example of operation: elements (B) and (D) transfer the bar to the right, while the other elements are not touching the bar. As elements (B) and (D) are retracted, (A) and (C) hold the bar in place. After that, the situation is reversed and elements (A) and (C) can transfer the bar. Other ways of operation exist, see Refs. 50 and 51. (c) The sample-holder is placed on top of the bars of the motors, before it is lowered towards the tip to get into the tunneling regime for imaging.

electrodes the applied voltage is varied between -200 V and +200 V, while on the opposite electrode a voltage of equal absolute value, but with reverse polarity, is applied. The range in the z-direction is 1 μm, which corresponds to applying a voltage between -200 V to +200 V to the inner electrode of the tube. The piezoelectric scanner is mounted in the center of the scanner body. To ensure a small ratio between the mass of the scanner and the mass of the body, the latter was made from molybdenum, which is not only a dense material but also UHV compatible. The body has three openings for access to the sample. In between the openings three approach motors are placed. These commercially available piezoelectric motors were selected because of their small size, large holding force of 7 N, and corresponding stiffness [50]. The working principle of the approach motor is depicted in Figure 2.4. Although such a motor was never used as an approach motor for scanning probe microscopes, the reported minimum step size ($\sim$1 nm) and the large travel range (depending on the length of the bar) made it a promising candidate*. Another important feature of the approach motor is its UHV-compatibility.

On top of the moving bars of the approach motors the sample-holder is placed. The coarse approach is done by moving the three bars downwards until the tip

---

*In practice however, when operated with the commercial driver electronics, the motors made unpredictable steps larger than 1 μm. These 'jumps' would render the motors useless as approach motors (see Section 1.3). The development of a smart drive signal and home-built, low-noise drivers were required to eliminate the problem [51].
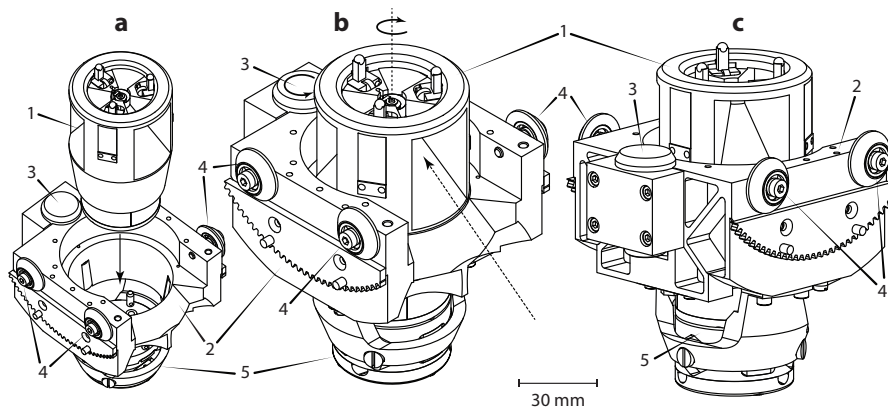
Figure 2.5: (a) The scanner body is placed into the cradle. (b) By using a piezoelectric motor the body can be rotated about the axis through the tip to change the azimuthal angle of incidence atoms and ions. The dashed arrow indicates the deposition and/or ion flux. (c) The cradle as viewed from the other side. The most important components are: (1) scanner body, (2) cradle, (3) piezoelectric rotary motor, (4) wheels, and (5) electrical connections.

and the sample are within the range of the piezoelectric scanner. As the motors can be operated independently, the sample can be positioned perfectly parallel to the imaging plane, which is important for fast imaging.

2.4   STM insert

To be able to change the angle of incidence of the deposition flux and the ion beam, the scanner body is placed in an aluminium cradle with four wheels. A precise fit of the tapered bottom part of the body into the cradle ensures a stable positioning of the body during scanning. A piezoelectric motor [52] can be used to rotate the body, including the sample if placed on top, as a whole about the axis through the tip to change the azimuthal angle of incidence, see Figure 2.5. The wheels of the cradle are placed on two curved, parallel tracks, on which it can ride to change the polar angle of incidence, as shown in Figure 2.6.

Figure 2.7 shows the STM insert. The tracks are mounted on a heavy stainless steel base, which is suspended by four extension springs. The total suspended mass exceeds 18 kg. The springs run through pipes, which are mounted on a UHV flange. The suspended assembly has an eddy-current damping system, consisting of copper brackets mounted on the base and magnets installed on the flange. The amount of damping can be tuned by changing the number of magnets. To compensate the change in the position of the center of gravity of the suspended mass when the cradle is put under an angle, counter weights are
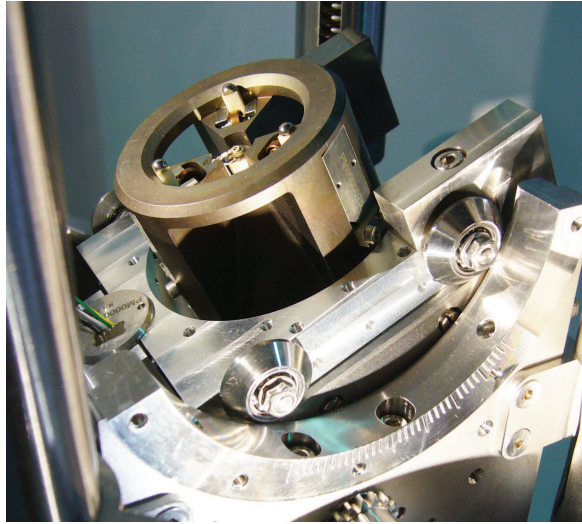
Figure 2.6: Photograph of the scanner body and cradle assembly, positioned on the tracks of the base. In the middle, top part of the image, one of the springs is visible.

installed that rotate in the opposite direction, see (7) in Figure 2.7. Electrical feedthroughs as well as mechanical drives, including one to drive the cradle on its rails, are located on the flange.

The STM insert, see Figure 2.7, is larger than in most other STM setups. First of all, the base is quite tall, which is required to fit the counter weights and cogwheels for the tilting of the scanner body. In addition, we have chosen to maximize the extension of the springs for the following reason. The suspended mass and spring assembly act as a mechanical filter above the resonance frequency f_{res}, given by:

$$f_{res} = \frac{1}{2\pi}\sqrt{\frac{k}{m}} = \frac{1}{2\pi}\sqrt{\frac{g}{\Delta l_e}}, \tag{2.1}$$

in which m is the mass, k is the combined spring constant of the four springs, g is the gravitational acceleration and Δl_e is the effective extension of the springs[*]. A low f_{res} corresponds to a large Δl[†]. In our case, the effective spring extension of 0.15 m results in a resonance frequency of 1.3 Hz. The total length of the extended springs is 0.26 m. Note that also the resonance frequency of the 'pendulum-mode' of the suspended base decreases for an increasing spring length.

The filtering effect of the mass-spring system depends on the resonance frequency and on the amount of damping in the system. Although the response of the mass to external vibrations around f_{res} decreases for larger system damping, the filtering

---

[*]For springs with a pretension F_t, the real spring extension is smaller, as $mg - F_t = k\Delta l$.
[†]For $\Delta l_e = 0.25$ m, $f_{res} = 1$ Hz.
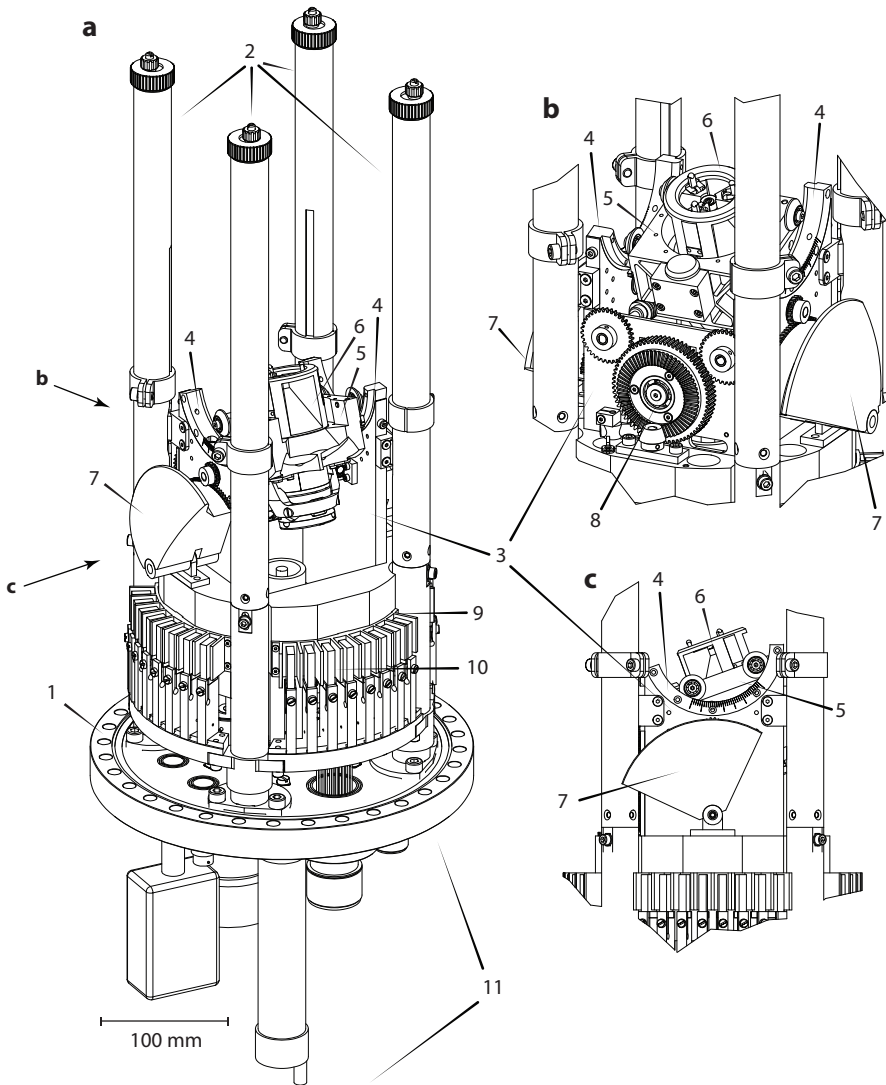
Figure 2.7:   (a) STM insert and (b,c) details of the suspended base. The most important components are: (1) UHV flange (NW250CF), (2) spring pipes, (3) base, (4) tracks, (5) cradle, (6) scanner body, (7) counter weights, (8) cogwheel assembly for cradle drive, (9) copper brackets for eddy-current damping, (10) magnet assembly for eddy-current damping, and (11) electrical feedthroughs and mechanical drives.

effect for $f \gg f_{res}$ is stronger in the absence of damping. The amplitude of transferred vibrations decreases as $1/f$ if the system is heavily damped, whereas in the limit of no damping the transfer $\propto 1/f^2$ [44]. As the first resonance frequency of the mechanical loop of our STM is much larger than the resonance frequency of our suspension system, see Chapter 3, vibrations around 1 Hz are not expected to form a problem for imaging. Hence, we decided to keep the damping as low as possible for more effective filtering at higher frequencies. For example, imaging during ion sputtering requires the operation of turbomolecular pumps, which introduces vibrations to the system at ∼1 kHz. All experiments, described in this thesis, were conducted without the magnets installed*.

Finally, we note that we have maximized the mass of the base. Although the transfer function of the suspension system, when normalized to the static response, is independent of the suspended mass, the amplitudes of the unwanted vibrations are smaller for a larger mass for the same level of external excitation. The design of the STM insert is the result of an optimization of the mechanical properties of the suspension system, within the boundaries set by the required functionalities of the STM.

2.5 UHV chamber and peripheral equipment

The STM is inserted into a custom-made UHV chamber [53], onto which also the deposition and ion sources are mounted; the UHV vessel is placed on a sand-filled frame. The STM is isolated from its environment by placing the frame on pneumatic isolators [54] that stand on an own foundation, which is detached from the main laboratory foundation. The setup is depicted in Figure 2.8. Figure 2.9 shows photographs of the STM inside the UHV chamber.

The system is evacuated by a magnetically levitated turbomolecular pump (backed by a rotary pump), an ionization pump, and a titanium sublimation pump (TSP) [55–57]. The pressure gauge is a Bayard-Alpert type ionization gauge, which provides accurate pressure readings between 10^{-3} mbar and its X-ray limit of approximately 3×10^{-11} mbar [58]. The residual gas composition can be determined by using a quadrupole mass spectrometer (QMS) [59]. To obtain UHV, the system is baked in a custom-made tent by a heater fan [60]. After production and before installation, the stainless steel UHV chamber was baked in a vacuum oven at ∼900 °C for several hours. This *vacuum firing* leads to a reduced outgassing and a smooth surface finish [61].

The deposition source is a 4-pocket e-beam evaporator, which allows the

---

*The suspension system is in reality not a simple mass-spring system, e.g. the springs are not massless. It may be required to damp higher order modes if these, at some point, result in image distortion. This depends on the level (and nature) of the environmental vibrations, which may change over time, as well as on the stability requirements for the specific STM experiment. The magnets can be installed at any time.
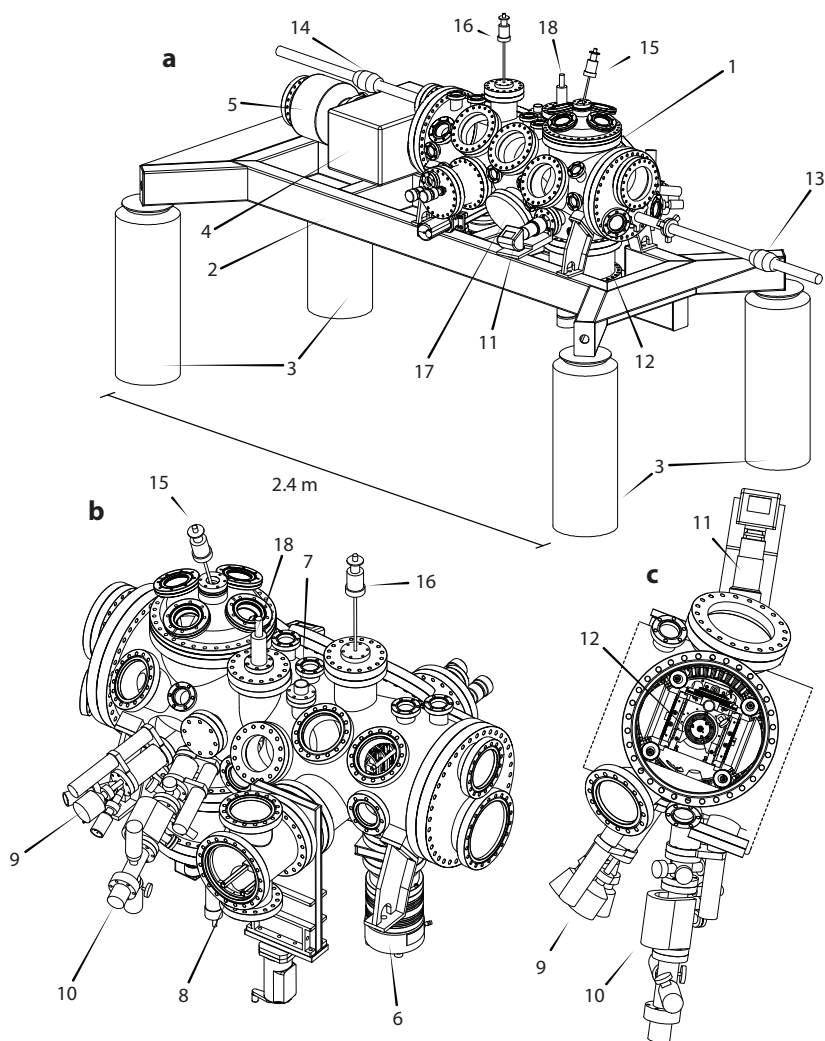
Figure 2.8: (a) Full setup, (b) UHV chamber viewed from the side of the deposition and ion sources (backside in (a)), and (c) segment of the UHV chamber with the top flange removed showing the STM insert. The components that are presently installed include: (1) main UHV chamber, (2) frame, (3) pneumatic isolators, (4) ionization pump, (5) TSP with cryo-shield, (6) turbomolecular pump, (7) pressure gauge, (8) load-lock, (9) e-beam evaporator, (10) ion source, (11) microscope-camera for optical approach, (12) STM insert, and (13) magnet drive for sample transport and direct deposition and evaporation (without STM), under almost any angle of incidence. Not shown, but mounted on the bottom of (1) is a quadrupole mass spectrometer. The components that have not yet been installed include: (14) magnet drive for scanner body transport, (15,16) wobble-sticks, (17) LEED/AES, and (18) He/N_2 flow cryostat.
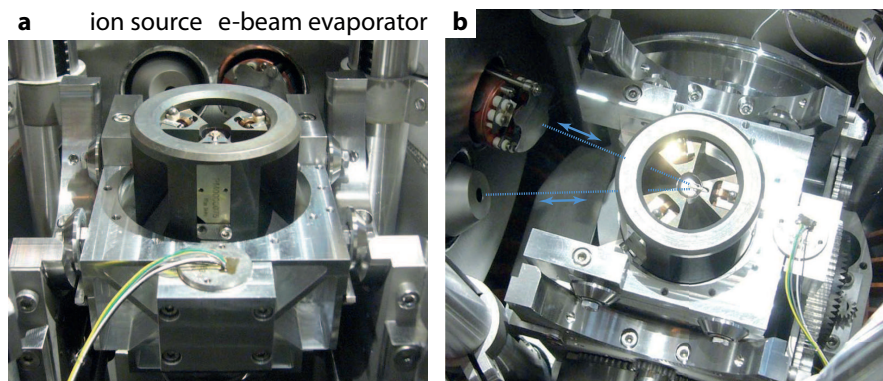
Figure 2.9: Photographs taken of the STM insert inside the UHV chamber. The ion source and the e-beam evaporator are pointed towards the tip-sample position. Both sources can move to and from the tip-sample position to change, respectively, the beam intensity and deposition rate.

(co-)evaporation of 4 different materials from a rod or a crucible [62]. During evaporation a small fraction of the vapour is ionized. The ions, which are undesired for pure e-beam evaporation, are extracted from the vapour to a charged electrode, which leads to an ion current that is proportional to the vapour pressure. When gauged, this ion current can be used to monitor the deposition rate during evaporation.

The ion source is a differentially pumped sputtering gun [63]. The typical pressure inside the ionization stage of the source is between 10^{-4} and 10^{-5} mbar, while in the main chamber UHV conditions can be maintained. The ion beam can be focused to a spot size of ~100 μm in diameter and can be scanned over a 10×10 mm^2 area[*]. The ion source is equipped with a Wien-filter to select the ions with the proper mass and charge. The ion energy can be chosen between 0.2 and 5 keV. Both the e-beam evaporator and the ion source are mounted on a linear transfer mechanism, so that they can be moved to and from the tip-sample position to respectively change the deposition rate and the ion beam intensity or profile[†].

If the sample-holder is not on the STM scanner body, it is placed in a holder/carrier that is mounted on a magnetically operated linear-and-rotary-drive, which enables the transport of the sample-holder through the chamber. In addition, the sample-holder can be placed in front of the sources to sputter the sample or deposit material onto it, without the presence of the STM, under al-

---

[*]The reported values of the spot size and scan range are valid for a working distance of 23 mm. The ion beam can also be used out of focus to sputter a larger area without scanning.

[†]Additionally, the deposition rate can be controlled by the power settings on the e-beam evaporator controller and the ion beam properties can be tuned by the gas pressure and the settings of the electromagnetic lenses.

most any angle of incidence. From the moment that the sample-holder is placed on top of the STM, tunneling conditions can be reached within 10 minutes. An optical microscope is used to bring the tip and sample within 100 μm [64], before the automated coarse approach is started. A special STM control-electronics set with analogue scan generation, suited for high-speed scanning and fast data acquisition, is used to control the STM [29, 65].

2.6 Performance

The base pressure of the UHV system is below the detection limit of the pressure gauge: $P < 3 \times 10^{-11}$ mbar. On a side note: this vacuum level is achieved after a bake-out of the system to a mere 90-100 °C, whereas normally 150 °C is required*. The bake-out temperature is limited by the maximum temperature the piezoelectric motors [50, 52] can stand. The fact that nonetheless excellent vacuum conditions are reached is attributed to vacuum firing procedure of the UHV chamber.

The new STM has proven to be a reliable instrument; atomic resolution is routinely obtained. Figure 2.10(a) shows an STM image of Si(111)-7×7, taken with two turbomolecular pumps running on the setup, of which one has conventional mechanical bearings. Figure 2.10(b) is an STM image of highly oriented pyrolytic graphite (HOPG) obtained with a high temporal resolution. The approach motors exhibit good stability, show very little drift ($<$2 nm h^{-1}), and can even be operated during scanning, without crashing the tip.

The instrument is suited for real-time growth and erosion experiments, for which the results presented in Chapters 4-7 provide a testimonial. The fact that the angles of incidence can be altered does not only allow experiments at different experimental conditions, it also offers the possibility of optimizing the access to the sample, which is crucial for a successful real-time experiment. The accessibility of the sample has also been successfully improved by *in situ* sharpening of the tip by an ion bombardment of its apex. The fact that the angles of incidence of the ions onto the tip can be altered, provides the possibility of sharpening of the tip from various sides.

The sample-holder is equipped with a filament, so that the sample can be heated from the backside by thermal radiation and by e-beam. Up to now, the heating option has only been used for sample preparation, but in principle, it is also possible to image at elevated substrate temperatures.

The system has been prepared for future additions, such as an *in vacuo* sample and scanner body storage, with the required transport and manipulation hardware. In addition, it will be possible to transfer sample-holders and scanners

---

*The relatively low bake-out temperature does not necessitate a prolonged bake-out time: 24-36 hours suffices.
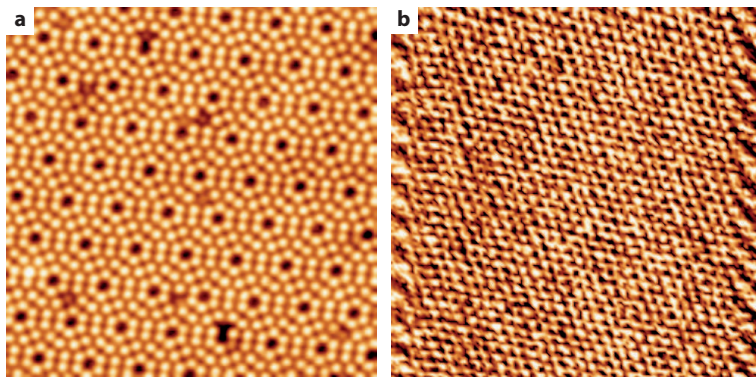
Figure 2.10: (a) STM image (raw data) of Si(111)-7 $\times$ 7 (20×20 nm^2) acquired in constant-current mode, showing atomic resolution. The image was taken while a turbomolecular pump with mechanical bearings, which is mounted directly on the setup, was in operation. (b) Constant-current STM image of graphite (HOPG) (10×10 nm^2), with atomic resolution. This image was acquired in 0.24 s, which corresponds to a line frequency of 533 Hz. The distortion at the edges is due to the use of a rounded triangle scan signal [29] and hysteresis in the piezoelectric material. As the image shows the height data, i.e. not the data of the 'error' signal of the hybrid mode, its acquisition required the actuation of the piezoelectric scanner in the z-direction at a frequency of $\sim$15 kHz.

bodies into and out of the UHV chamber via a load-lock, without breaking the vacuum in the main chamber. The required components have been designed and fabricated. In addition to STM, a combined low-energy electron diffraction (LEED) and Auger electron spectroscopy (AES) system [66] will be installed as an analytical instrument. Studies of growth and erosion processes at cryogenic substrate temperatures will become available with the installation of a He/N$_2$ flow cryostat [67].

2.7 Summary

To study the changing surface morphology of a substrate during deposition and erosion experiments with atomic-scale resolution, we have developed a dedicated UHV-STM setup. The heart of the instrument, the STM scanner body, has an open structure, so that there is line-of-sight access to the tip-sample position, towards which an e-beam evaporator and an ion source are pointed. The STM scanner body is placed in a cradle that can ride on curved tracks in order to tilt the microscope and change the polar angle of incidence. Using a piezoelectric rotary motor mounted in the cradle, the STM scanner body can be rotated about the axis through the tip to change the azimuthal angle of incidence. Besides the fact that the tilting and the rotation of the STM can be used to perform experiments

at different angles of incidence, it also enables an optimization of the accessibility of the sample. Additionally, the configuration naturally offers the possibility to sputter the tip to sharpen it.

The cradle with the STM scanner body is placed on a heavy base that is suspended by extension springs. This mass-spring system creates a very effective mechanical filter, which enables us to perform stable STM experiments even when the level of the environmental vibrations is considerable. The suspension system is mounted on a UHV flange and is inserted into a custom-made UHV chamber, onto which also the e-beam evaporator and ion source are mounted.

To be able to follow fast surface processes during film growth and ion erosion, the STM has been designed as a fast scanning microscope. In part, the specific design of the STM is the result of FEA calculations of the structural mechanics of the scanner body. These calculations are presented in the next chapter.

CHAPTER 3

Towards faster STM with finite element analysis

This chapter is devoted to the extensive finite element analysis calculations that we performed to evaluate and optimize the mechanical properties of the special-purpose STM of Chapter 2 prior to its construction. The calculations were used to determine the most rigid configuration of the microscope in order to maximize its imaging speed. The modelling was done in 3D, by using detailed computer-aided design drawings. Not only did we determine the eigenfrequencies and eigenmodes of the full system, we also calculated the amplitudes of the vibrations of the sample, which are excited by the motion of the piezoelectric scanner. After the microscope was constructed, the calculations were compared with optical measurements of the motion of the sample, while harmonically driving the piezoelectric scanner. The results presented in this chapter show the fast scanning capabilities of the new STM, as well as the applicability of the finite element method as a deterministic 'tool' for the design of scanning probe microscopes.

3.1   Introduction

As discussed in Section 2.2, for a fast scanning probe microscope (SPM) it is beneficial to aim for high resonance frequencies of the components in the mechanical loop (see Figure 2.1). The reason for this is that during the high-frequency actuation of the piezoelectric scanner, through the excitation of resonances in the microscope, the motion of the sample can be so large that it causes image distortions. Not only the resonance frequency, but also the nature of the resonance is of significance in this respect. It is important to determine what part of the microscope moves by what amount when the piezoelectric scanner is excited and what the effect of this is on the imaging. Preferably, one would like to answer these questions for a particular design of an SPM, without actually constructing and testing it. By using finite element analysis (FEA), a technique suited to evaluate the mechanical properties of complex structures, during the design of a microscope, insight can be gained in its expected performance. In addition, FEA calculations can be used to identify the weak points in the structure, after which the design, and consequently the performance of the microscope, can be improved.

The final design of the STM scanner body, see Section 2.3, is the result of an optimization of its mechanical rigidity, within the geometrical constraints set by the application of the STM to *live* observations of deposition and erosion. The optimization was an iterative process that included FEA calculations of the structural mechanics of the scanner body to identify those parts that would compromise the rigidity, and subsequent improvements to the design. It would be beyond the scope of this thesis to report on the complete optimization process; instead we give a detailed account of the FEA of the final version of the STM scanner body[*]. This gives insight into the nature of imaging artefacts and it allows us to pinpoint the residual points of improvement for the next-generation scanners. In addition, the FEA calculations of the final version of the design could be used to assess the quality of our modelling by a comparison with the experimental characterization of the constructed STM.

Up to now FEA calculations have been performed to evaluate the structural mechanics of parts of the mechanical loop of SPMs, see e.g. Refs. 29, 68 and 69, but reports on a modelling of the complete mechanical loop are limited [70]. A FEA calculation, in three dimensions, with only minor simplification of the actual structure, has to our knowledge not been performed before. We have used detailed, 3D computer-aided design (CAD) drawings to not only calculate the resonance frequencies of the scanner body and sample-holder assembly, but also the response of the structure to the force exerted by the motion of the piezoelectric scanner. After the construction of the STM, these results could be

---

[*]Small differences do exist between the model presented here and the STM that was actually constructed. These resulted from minor changes to the design after the modelling that were necessary for the integration of the scanner body into the complete setup.

compared directly with the experimental determination of the amplitudes of the vibrations of the sample-holder, while driving the piezoelectric scanner, simulating the scanning motion during STM experiments.

3.2 Structural mechanics with FEA

A FEA calculation is used to numerically solve differential or integral equations on a domain, which is subdivided into a large number of small elements. The original area of application of FEA is the evaluation of the mechanical properties of complex structures [71–73], which is precisely the task we have had at hand. In a FEA calculation, the structure under investigation is divided into a *mesh* of elements. The main objective is to obtain $\mathbf{u}$, the set of displacements of all nodes in the mesh, when a force is applied to the object; $\mathbf{u}$ is an $(N \times D)$ vector, in which N is the number of nodes and D is number of degrees of freedom; $D = 3$ in our case.

In a *modal* analysis, the eigenfrequencies (resonance frequencies) of an object, and the corresponding eigenmodes are found by solving

$$\mathbf{M}\ddot{\mathbf{u}}(t) + \mathbf{K}\mathbf{u}(t) = \mathbf{0}, \tag{3.1}$$

in which $\mathbf{M}$ and $\mathbf{K}$ are the $3N \times 3N$ mass and stiffness matrices. Note that in the frequency domain this reduces to

$$(-\omega^2\mathbf{M} + \mathbf{K})\tilde{\mathbf{u}}(\omega) = \mathbf{0}. \tag{3.2}$$

Diagonalising $-\omega^2\mathbf{M} + \mathbf{K}$ yields the eigenfrequencies ω_n of the object, and subsequently the eigenmodes $\tilde{\mathbf{u}}(\omega_n)$ can be calculated.

The eigenmodes, or mode shapes, give the ratio between the displacements of the nodes in the mesh when the mode is excited, i.e. an eigenmode can only be used to study the shape of the mode. To calculate the actual displacement of a certain node in the mesh when an external force is exerted, damping must be incorporated in the analysis and the following equation is to be solved:

$$\mathbf{M}\ddot{\mathbf{u}}(t) + \mathbf{C}\dot{\mathbf{u}}(t) + \mathbf{K}\mathbf{u}(t) = \mathbf{f}_{ext}(t), \tag{3.3}$$

or

$$(-\omega^2\mathbf{M} + i\omega\mathbf{C} + \mathbf{K})\tilde{\mathbf{u}}(\omega) = \tilde{\mathbf{f}}_{ext}(\omega), \tag{3.4}$$

where $\mathbf{C}$ is the $3N \times 3N$ damping matrix.

The mass and stiffness matrices can be derived directly from the tabulated material properties, i.e. from the density and Young's modulus of the material of the individual elements, but for $\mathbf{C}$ for many materials no reliable numbers are available. This is partly due to the fact that the same material can have a different degree of damping, depending on the microstructure of the material. The

microstructure depends on the production process of the raw material and on the history of further processing, e.g. on the type of machining and whether or not the material has been annealed. To model the damping in an efficient way in a FEA calculation, often the so-called *Rayleigh damping* is used [74], in which the damping matrix is given by:

$$\mathbf{C} = c_1 \mathbf{M} + c_2 \mathbf{K}, \tag{3.5}$$

where the coefficients c_1 and c_2, which may depend on ω, are to be determined to correctly capture the, often frequency dependent, damping*. The damping of mode n can be described by the modal quality factor Q_n, given through:

$$\frac{1}{Q_n} = \frac{c_1}{\omega_n} + c_2 \omega_n. \tag{3.6}$$

In our analysis we have used the simplest form of damping, which ascribes equal damping to all modes. This *loss factor* damping is obtained by setting $c_1 = 0$ and $c_2 = (Q\omega)^{-1}$. We have assumed a quality factor of 10^5 for all metal parts and $Q = 10^7$ for the ceramic components, which is the best educated guess on the basis of available literature, see e.g. Refs. 75 and 76. The quality factor of the piezoelectric scanner was set to 100 [49]. For most materials used in the construction of the STM, the damping is not known. As the approach motors were expected to critically influence the properties of the mechanical loop, we determined some of their important mechanical properties prior to the modelling. This is discussed in Section 3.3.1.

3.3   Results and discussion

We used a commercial FEA software package to calculate the mechanical properties of our microscope [77]. After importing the 3D-drawings into the program [78], a mesh was generated. For complex structures the choice of a proper mesh is critical: it must be fine enough to capture the details of the object, but the number of elements must be kept within bounds to limit the computation time. Figure 3.1 shows the mesh that was chosen for the analysis of the STM body. Some elements needed to be simplified prior to the modelling to be able to generate a suitable mesh: the prime example for this is the complex internal structure of the coarse approach motors.

3.3.1   Modelling the approach motors

The model version of a single coarse approach motor consists of an alumina bar and four piezoelectric elements, as in Figure 3.2. We have simplified the

---

*Note that in the case of frequency dependent damping, the term $\mathbf{C}\dot{\mathbf{u}}(t)$ in Equation 3.3 becomes a convolution in the time-domain.
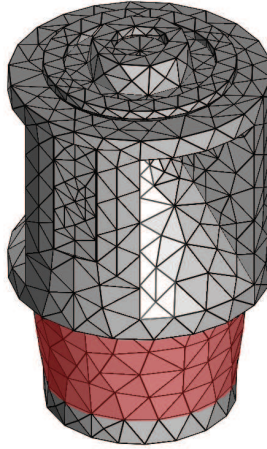
Figure 3.1: The mesh of the STM body and sample-holder assembly consists of 20617 elements. As a boundary condition for the calculations the surface of the tapered part of the scanner body, indicated in red, was fixed.

motors for this analysis by leaving out the housing, the rolling bearings, and the spring; cf. Figures 2.4 and 3.2. In general, when operating the motors, two piezoelectric elements are holding the bar at any time. Figure 3.2 shows the first eigenmode of the simplified version of the motor, in which we have assumed a fixed contact between the bar and each of the two elements. We adjusted the material parameters of the piezoelectric elements such that the eigenfrequency f_1 and the quality factor Q of this mode correspond to experimentally determined values, which were obtained by an electro-mechanical measurement. In this way, we obtained the most simple model of the motors describing the correct behaviour up to the first resonance.

Figure 3.3 shows the electrical scheme that was used to determine f_1 and quality factor Q of the first eigenmode. In the analysis an electronic equivalent of a piezoelectric vibrator, the Butterworth-Van Dyke circuit, is used [79]. The admittance $Y(\omega)$ of the motor is given by:

$$Y(\omega) = i\omega\, C_0 + \frac{i\omega\, C}{1 - (\omega/\omega_1)^2 + (i\omega)/(Q\omega_1)}, \tag{3.7}$$

in which $\omega_1 = 1/\sqrt{LC}$ and $Q = \sqrt{L/C}/R$. By measuring $Y(\omega)$, a value of $f_1 = \omega_1/2\pi = 3.5$ kHz and $Q = 150$ were extracted and used in the further modelling.
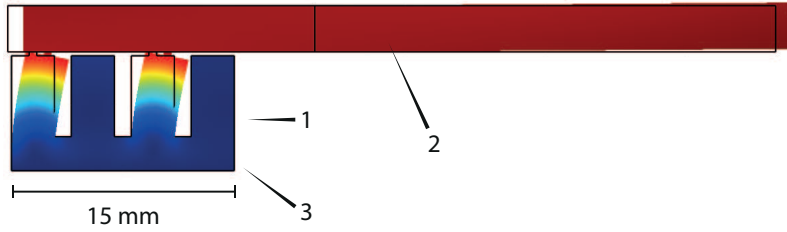
Figure 3.2: The first eigenmode of the simplified model of the approach motor, calculated using FEA. The (exaggerated) deformed shape and the colours, from blue (no displacement) to red (largest displacement), show the relative amplitudes of displacement in the mode. The components of the motor are: (1) 4 piezoelectric elements, (2) alumina bar, and (3) motor base. During STM operation, two piezoelectric elements hold the bar. Note that in the further FEA calculations, as well as in the constructed microscope, the alumina bar is shorter. The analysis of the mechanical properties of the motors was carried out with the bar at the original length, before it was shortened to improve the properties of the mechanical loop. The part of the bar left of the vertical line was used in the further modelling.
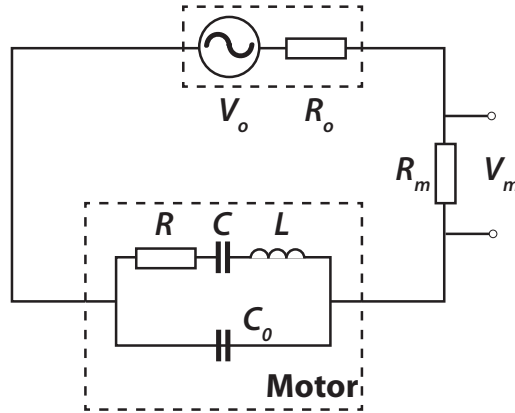
Figure 3.3: Measurement scheme that was used to analyse the first mechanical resonance of the approach motor. The electrical behaviour of the motor, around the mechanical resonance frequency, is modelled by the *LCR*-branch. Similar branches can be added in parallel to incorporate higher order modes. The capacitor C_0 is the capacitance of the piezoelectric elements of the motor. The admittance of the motor can be determined via: $Y(\omega) = (R_m \frac{V_o}{V_m}(\omega) - (R_o + R_m))^{-1}$ by measuring the voltage V_m over R_m as a function of the oscillator output $V_o(\omega)$. R_0 is the output resistance of the oscillator.

3.3.2 Resonance frequencies and mode shapes

Using the simplified model of the approach motors, the first 20 eigenmodes of the scanner body including the sample-holder were calculated. The results are given in Table 3.1, and the mode shapes of selected eigenmodes are depicted in Figure 3.4.

f_n [Hz]	Fig. 3.4(..)	Description	f_n [Hz]	Fig. 3.4(..)	Description
1635	a	z-mode sample-holder	7113	d	bending bars
1822	b	tilt sample-holder	7231		bending bars
1827		tilt sample-holder	8515	e	rotation body
2031		tilt sample-holder	9377	f	bending body
2062		tilt sample-holder	9383		bending body
2279	c	rotation sample-holder	11453	g	bending scanner
6650	d	bending bars	11454		bending scanner
6739		bending bars	15523	h	oval mode body
6813		bending bars	15532		oval mode body
6845		bending bars	19642	i	z-mode body

Table 3.1: The first 20 resonance frequencies of the scanner body including the sample-holder. Eigenmodes that have a similar mode shape, have been grouped (a-i). From each group one example is depicted in Figure 3.4.

The modes with the six lowest eigenfrequencies, (a), (b) and (c), originate from the bending of the piezoelectric elements in the approach motors. The first resonance at 1.6 kHz (a) causes the sample-holder to oscillate in the z-direction, i.e. perpendicular to the scanning plane. This mode corresponds to the in-phase oscillation of the three motors, each vibrating at their first eigenmode (Figure 3.2). The resonance frequency is now lower, because each motor carries the additional mass of $1/3$ of the mass of the sample-holder. The out-of-phase oscillation of the motors results in the tilting of the sample-holder (b). The in-phase sideways deformation of the piezoelectric elements in the motors leads to the rotation of the sample-holder about the axis through the tip (c). Modes (d), between 6.7 kHz and 7.2 kHz, involve the bending of the free ends of the bars of the approach motors. The flexibility of the Mo body causes the modes depicted in Figures 3.4(e), (f), (h) and (i). Although it is not apparent from Figure 3.4, theses modes, except for (e), also involve the displacement of the base of the piezoelectric scanner. Finally, the two eigenmodes at 11.5 kHz (g), are two degenerate bending modes of the piezoelectric scanner; the degeneracy implies that the coupling of these modes to the rest of the, three-fold symmetric structure, is modest.

a

1635 Hz

b

[1822..2062] Hz

c

2279 Hz

d

[6650..7231] Hz

e

8515 Hz

f

9377, 9383 Hz

g

11453, 11454 Hz

h

15523, 15532 Hz

i

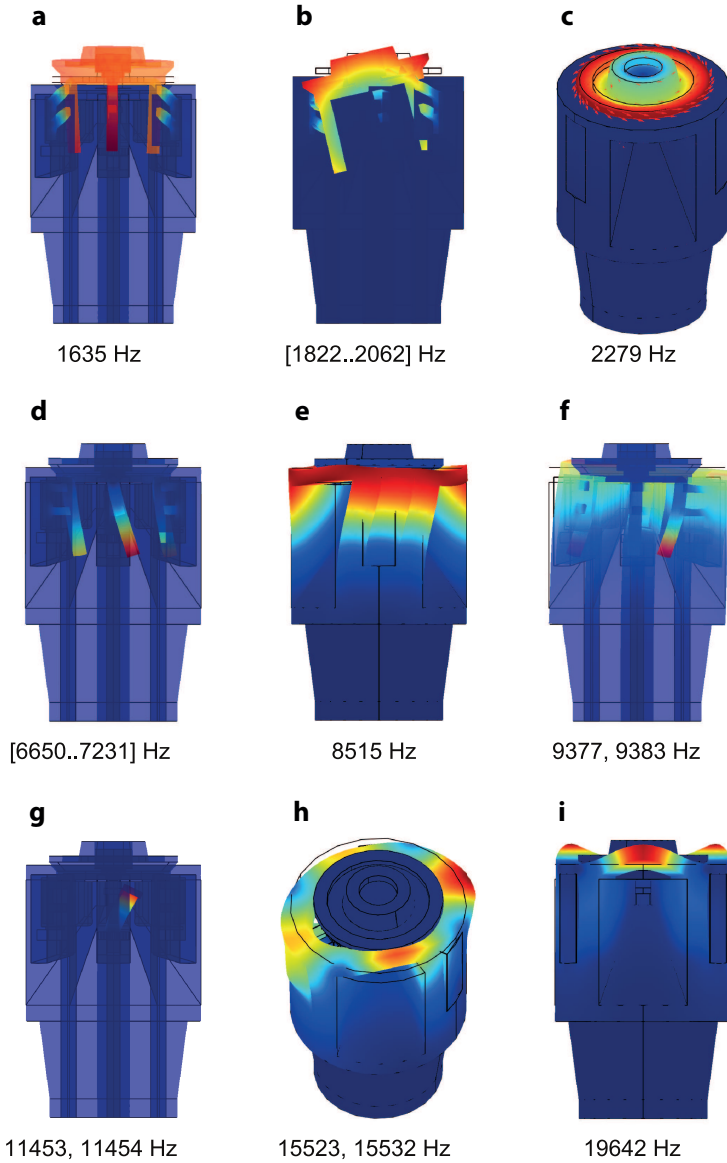19642 Hz

Figure 3.4: Mode shapes of the resonances of the scanner body including the sample-holder up to 20 kHz. The (exaggerated) deformed shape and the colours, from blue (no displacement) to red (largest displacement), show the relative amplitudes of displacement in the mode. Eigenmodes that have a similar mode shape, have been grouped, see Table 3.1; per group only one example is depicted.

3.3.3 Vibration spectra

Although the eigenmode analysis is instructive to identify the weak points in the structure, it is *a priori* not clear to what extent these modes will be excited noticeably by the motion of the piezoelectric scanner. For example, as the eigenmodes depicted in Figure 3.4(c) and (e) are of a rotational nature, we do not expect that these modes are strongly excited during scanning. In addition, whether or not a certain resonance leads to image distortion during STM operation, depends strongly on the modal damping. In the case of considerable damping, i.e. a low Q_n, the resulting amplitude of vibration may be low enough to not have an effect on the imaging. Therefore, from an STM designer's perspective it is thus favourable to have a considerable amount of modal damping. On the other hand, if the damping of a mode cannot be increased sufficiently a certain mode can cause the deterioration of the image quality, not only precisely *at* the resonance frequency, but within the typical frequency band $\Delta f = f_n/Q_n$. In this case, it might be better not to aim for additional damping of the mode.

To investigate to what extent the eigenmodes of the system would result in a displacement of the sample during scanning, we calculated the vibration spectra between 1 kHz and 20 kHz. The motion of the piezoelectric scanner was simulated by applying a bipolar voltage with an amplitude of 20 V to firstly the x-electrodes and secondly the y-electrodes[*]. Taking into consideration the added length of the tip-holder and tip of $\sim$8 mm, this corresponds to a scan amplitude of 150 nm, or a 300×300 nm^2 scan[†]. To the z-electrode a bipolar voltage with an amplitude of 1 V was applied that results in an oscillation amplitude of 2.5 nm, which corresponds to the imaging of a rough surface. Figures 3.5, 3.6 and 3.7 show the response of the sample in the x-, y-, and z-directions to a excitation of the scanner in respectively x, y and z.

In the figures we have also indicated the maximum amplitudes of vibration for stable imaging, if one wants to follow the evolving surface morphology during deposition or erosion experiments with atomic step resolution and a lateral resolution that just exceeds the true atomic resolution in the crystal terraces. If the amplitude in z is smaller than 30 pm, atomic step resolution can be easily obtained. The maximum tolerable in-plane vibration amplitude was set to 0.3 nm, which approximately equals the atomic separation distance of most materials in the terraces and is just below the size of a single pixel[‡]. For true atomic resolution, the tolerable amplitudes are a factor 10 lower: laterally 30 pm and in the z-direction 3 pm[§]. Note that images showing full atomic resolution are often much smaller than 300×300 nm^2, more commonly of the order of 30×30 nm^2. As we have used a linear model for the FEA calculations the following holds:

---

[*]On opposite electrodes a voltage of equal absolute value and reverse polarity was applied.
[†]The x-axis and y-axis are defined as in Figure 2.3(b).
[‡]This holds if the pixel resolution is 512×512 pixels^2, which is a common choice for the imaging of a 300×300 nm^2 area.
[§]Obviously the precise values depend strongly on the choice of the substrate.

Figure 3.5:   Amplitude of vibration of the sample, in the *x*-, *y*- and *z*-directions, when the piezoelectric scanner is excited harmonically in the *x*-direction at a varying excitation frequency. The amplitude of oscillation at the end of the tip is 150 nm. The eigenfrequencies (a-i), as well as the tolerable amplitudes (see text) in *x* and *y* (dashed line) and in *z* (solid line) are indicated.
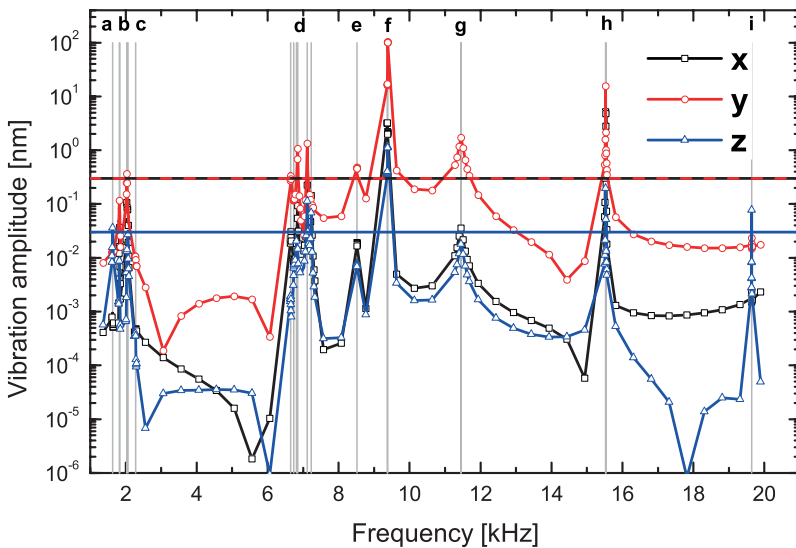
Figure 3.6:   Amplitude of vibration of the sample, in the *x*-, *y*- and *z*-directions, when the piezoelectric scanner is excited harmonically in the *y*-direction at a varying excitation frequency. The amplitude of oscillation at the end of the tip is 150 nm. The eigenfrequencies (a-i), as well as the tolerable amplitudes (see text) in *x* and *y* (dashed line) and in *z* (solid line) are indicated.
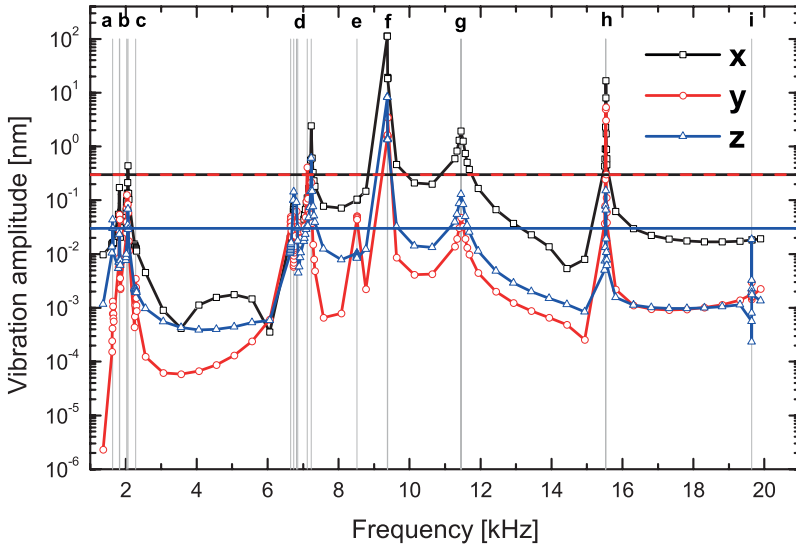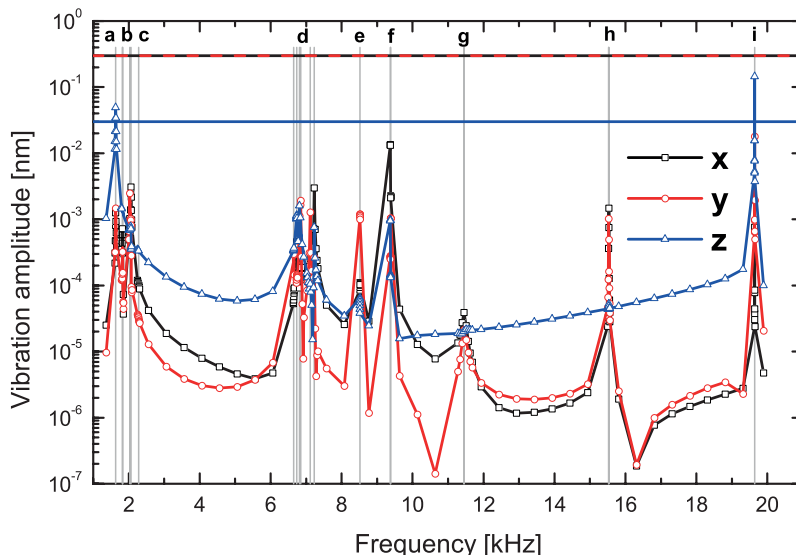
Figure 3.7: Amplitude of vibration of the sample, in the x-, y- and z-directions, when the piezoelectric scanner is excited harmonically in the z-direction at a varying excitation frequency. The amplitude of oscillation of the tip is 2.5 nm. The eigenfrequencies (a-i), as well as the tolerable amplitudes (see text) in x and y (dashed line) and in z (solid line) are indicated.

if the excitation amplitude is a factor 10 smaller, so is the vibration amplitude of the sample. When the scale on the vertical axes in Figures 3.5 and 3.6 is multiplied by 0.1, the graphs can thus also be used to evaluate the fast scanning capabilities of the STM when performing a truly atomically resolved 30×30 nm^2 scan.

On a flat terrace, the required excitation amplitude in the z-direction for atomic resolution is much smaller than 2.5 nm. It is of the order of the amplitude of the atomic corrugation: $\sim$10 pm for metal substrates and $\sim$50 pm for Si(111)-7$\times$7. On a typical metal surface, the frequency of the z-excitation to track the atomic corrugation is $\sim$100 times higher than the line frequency for a 30×30 nm^2 scan. For that scan size, on a Si(111)-7$\times$7 substrate, when only the adatoms and the corner holes of the surface reconstruction [80] are imaged, the excitation frequency in z is $\sim$30 times higher than the line frequency. Similarly to the lateral scanning, also the response of the structure to varying excitations in the z-direction, can be scaled, using Figure 3.7.

The vibration spectra show that at and around many eigenfrequencies the vibration amplitude of the sample is considerable. Naturally, the excitation of a certain mode depends on the coupling to the piezoelectric scanner. Modes (a) and (i), which are pure z-modes, are excited relatively more strongly by the excitation in

z, than by x, y excitations. Similarly, the modes depicted in Figures 3.4 (b), (f), (g), and (h) are excited very effectively by the x, y oscillations of the scanner. As expected, we find that the rotational modes, (c) and (e), are only modestly excited by the motion of the scanner (in any direction). The breaking of the x, y-symmetry by the three-fold symmetric structure is reflected by the difference in response to the excitation in x and y, as well as by the x, y response to the z excitation.

From the width of the peaks we can obtain Q_n. The modal quality factors of (a) and (g), of respectively 1.6×10^2 and 1.0×10^2, are close to the quality factor of the components with the highest deformation in that mode, the piezoelectric elements of the motor and the scanner respectively. Q_n of (h) is 4000, which is a factor 25 lower than the quality factor assigned to the molybdenum body. This indicates that the damping of this mode does not only occur in the body, but probably also in the scanner and parts of the approach motors.

On the basis of these analyses we must conclude that the vibration amplitude exceeds the tolerable amplitudes for a number of eigenmodes. Especially the response to the lateral scanning at certain frequencies should be expected to lead to imaging problems. We must also bear in mind that, commonly, the scanning is not done with a sinusoidal excitation, but rather with a triangular scan signal. Hence, also the excitation of resonances through harmonics of the principal scanning frequency f_s must be considered[*]. The severity of this issue can be reduced by using a *rounded triangle* scan excitation, in which only the contributions at f_s and $3f_s$ appear in the spectrum [29]. Rounding leads to a distortion at the edges of the image, but not in the center of the image. An imaging rate of 1 frame per second (fps) should be possible with a pixel resolution of 512×512 pixels^2, as $3f_s = 1536 < 1635$ Hz. Between 2.1 kHz and 6.7 kHz the vibration amplitude is far below the tolerable limit, and so it should be possible to scan at a line frequency just above 2.1 kHz, which keeps $3f_s$ just below 6.7 kHz. Likewise, aiming for the 'lulls' around 8 kHz and 10.5 kHz, stable imaging should be possible with $f_s = 2.7$ kHz and $f_s = 3.5$ kHz. The latter scan frequency corresponds to an imaging rate of 27 fps, with 128 lines per frame. In principle it should be possible to increase f_s to 10.5 kHz (82 fps with 128 lines per frame), which is just below the bending resonance frequency of the tube scanner. Whether this is possible with a rounded triangle scan excitation depends on the response around 31.5 kHz[†]. Otherwise a pure sine could be used. Whether the imaging rates discussed here are at all possible, depends strongly on the required motion in the z-direction, which depends on the surface roughness and tilt of the sample to be investigated. Furthermore, we are not sure about the accuracy of our FEA calculations, as the modelling included the simplification of the approach motors and the incorporation of unknown damping

---

[*]For a triangular scan signal the amplitudes of the Fourier components decrease as $1/f^2$.

[†]The resonance behaviour of the same type of piezoelectric scanner has been measured up to 100 kHz [46]. No eigenmode was found around 31.5 kHz. However, also the resonances in other parts of the microscope need to be considered.

parameters. In addition, the model is completely linear, but in reality we can expect non-linear coupling of modes, for example as a result of the non-linear behaviour of piezoelectric material [46]. To assess the quality of our modelling, we have performed optical measurements on the built-up microscope to measure the response of the sample to the excitations of the piezoelectric scanner.

3.3.4 Model versus experiment

After the STM had been constructed, we measured the vibration amplitude of the sample when excited by the motion of the piezoelectric scanner, by using a *laser Doppler vibrometer* (LDV) [81]. With an LDV, the velocity of an object, or part of it, can be determined by measuring the Doppler shift of a laser beam reflected off the moving surface. Integration of the data yields the displacement; a resolution of 10 pm can be achieved.

While the scanner was excited harmonically in either the x- or z-direction, the x and z vibration amplitudes of the sample-holder were measured with the LDV. Between 1 kHz and 10 kHz the scanner was driven with an amplitude of 30 V on the electrodes[*]. In order not to damage the piezoelectric scanner, between 10 kHz and 20 kHz the excitation amplitude was reduced by a factor 6 to 5 V[†]; this is especially important around the bending resonance of the piezoelectric scanner[‡]. The measured spectra, including a measurement of the background noise level, are shown in Figure 3.8.

The measurements of the background noise level show two peaks, at 1.3 kHz and 2.3 kHz. The first peak is present in all other spectra, at comparable amplitudes, and so we attribute this excitation to the structure of the LDV setup, rather than to the STM. The height of the 2.3 kHz peak, however, increases significantly if excited, especially in the [x to z] and [z to z] spectra. If we compare this with the FEA results, this mode is very likely to be the mode depicted in Figure 3.4(a). At 1.9 kHz there is a peak in the [x to x] and [x to z] spectra, which is absent in the [z to x] and [z to z] spectra, so we speculate that this is one of the (b) modes. The measured amplitudes for the first two modes, (b) and (a), are very close to the calculated values[§]. The reason for this is the experimental determination of the quality factor of the approach motors.

We do not find any modes in the FEA calculations corresponding to the peaks measured between 3.4 kHz and 5.1 kHz. Some of these modes may very well result from the approach motors, which were simplified in the modelling. The

---

[*]This amplitude is 1.5 times larger than the x, y excitation amplitude in the FEA calculations and 30 times larger than excitation in the z-direction, and was chosen to have a better signal-to-noise ratio. For the comparison, the FEA results can be scaled to these amplitudes.

[†]This is a factor 4 smaller than in the FEA calculations for x; a factor 5 larger for z.

[‡]The amplitude at resonance is Q times higher than the drive amplitude.

[§]Note that the factor 1.5 difference in the excitation amplitude of the LDV with respect to the FEA calculations is to be taken into account.
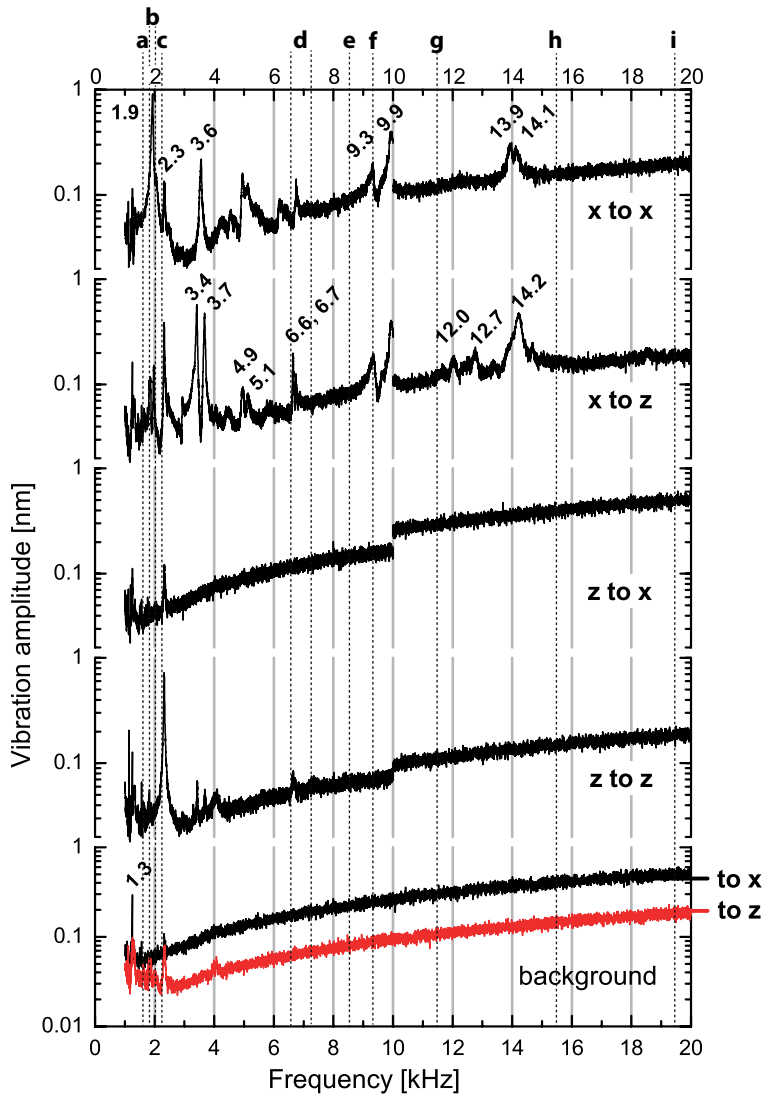
Figure 3.8: Amplitudes of the vibrations of the sample-holder obtained with LDV. The bottom graph shows the background noise level when measuring in the *x*- and *z*-directions without any excitation. The other graphs, the [*i* to *j*] spectra, show the response in *j* to an excitation in *i*. Between 1 kHz and 10 kHz the amplitude of the drive signal is 30 V for both the *x*- and *z*-direction; between 10 kHz and 20 kHz the amplitude was lowered to 5 V to not damage the scanner. The peaks are labelled with their frequency in kHz; the peaks are labelled only once. Note that the background noise level was not constant throughout the measurements. At the top of the figure the calculated eigenfrequencies are indicated.

6.6 kHz and 6.7 kHz peaks fall in the band of the (d) modes. These excitations could indeed involve the bars of the approach motors, since the peaks are rather narrow and the quality factor of the ceramic bars is expected to be large. At 9.3 kHz and 9.9 kHz we find peaks in the [x to x] and [x to z] spectra that are likely to be the (f) modes, which are separated further in reality due to a stronger symmetry breaking.

Between 12.0 kHz and 12.7 kHz we find, just above the noise level in the [x to z] spectrum, some vibrations that we can trace back to the bending modes of the piezoelectric scanner, depicted in Figure 3.4(g). We have also measured the bending modes directly on the scanner in the z-direction and found 12.4 kHz for the bending-mode in the x-direction and 12.6 kHz in the y-direction, see Figure 3.9. The difference in frequency of both bending modes can be the result of imperfections in the piezoelectric material, slight variations in the wall-thickness of the tube, and the effect of symmetry breaking due to other parts of the microscope. For example, the resonance frequency in the y-direction can be slightly higher due to the added stiffness of the coaxial cable to the tip-holder, which is aligned to this direction. The fact that the spectrum measured on the sample-holder appears to be somewhat different than the spectrum measured directly on the piezoelectric scanner shows the influence of the transfer-function of the scanner body and sample-holder assembly on the measurement. Curiously, the coupling of the bending resonances to the sample-holder is not visible in the [x to x] spectrum; we did expect a stronger coupling in this spectrum than in the [x to z] spectrum on the basis of the FEA calculations. It may be that the mechanical filtering of the approach motor and sample-holder assembly is stronger in the lateral directions than anticipated, or that the transfer-function is reduced by losses in contact points, for example between the bars of the approach motors and the sample-holder. In any case, we hardly see the bending resonances of the scanner reflected in the motion of the sample-holder, even though at resonance the amplitude of vibration of the scanner is amplified by a factor Q. This points towards a minor coupling of the motion of the scanner to the rest of the structure, which was precisely the goal to be realized in the design.

The large peaks around 14 kHz in the [x to x] and [x to z] spectra are likely to be the (h) modes, which show also a considerable amplitude in the calculated spectra. It should be noted that the level of the background noise prevents us from identifying any resonances in the [z to x] and [z to z] spectra above ∼7 kHz.

The measured amplitudes of some of the modes, e.g. (d) and (f), are much larger in the calculated spectra. Clearly, the amount of damping has been un-derestimated, which implies that the STM performs better than what could be anticipated on the basis of the FEA results. Additional damping can be due to losses in joints or from viscous damping in the air. Just as the FEA calculations, also the LDV experiments show that the response of the sample-holder to the
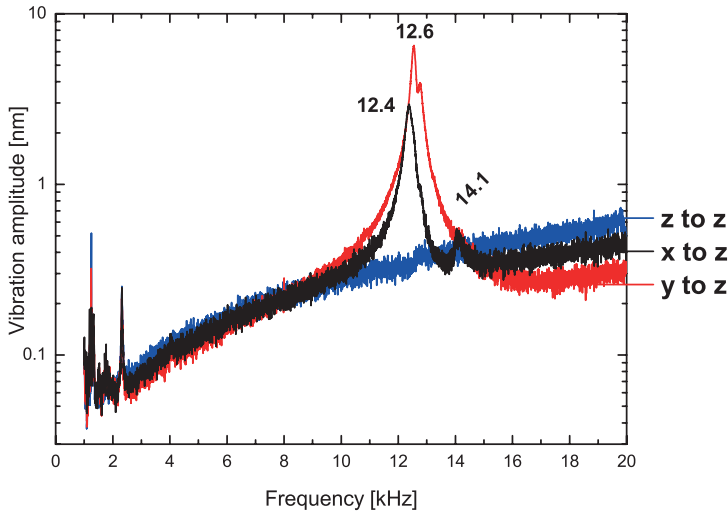
Figure 3.9:   The vibration amplitude of the piezoelectric scanner, measured in the *z*-direction, as a function of excitation frequency. The excitation was done in all three directions with an amplitude of 0.1 V. The quality factor of the bending resonance modes is ∼70.

motion of the piezoelectric scanner exceeds the tolerable amplitudes for atomic resolution for a number of eigenmodes.

The lowest eigenfrequency of the system is 1.9 kHz and is somewhat larger than calculated, which is beneficial for fast imaging. On the basis of Figure 3.8, we conclude that it should be possible to scan with any harmonic excitation up to 1.6 kHz, which corresponds to a maximum line frequency of 0.53 kHz, when a rounded triangular scan signal is used. The STM image depicted in Figure 2.10(b), which was recorded with precisely this line frequency, shows the feasibility of this type of operation. Like the FEA calculations, the measured spectra show the possibility of scanning 'between' resonances, with a sinusoidal, but also with a (rounded) triangular excitation, as shown in Figure 3.10.

3.4   Conclusions

We have demonstrated the applicability of FEA to structural mechanics at the nanometer scale, but we have also revealed shortcomings of the modelling by performing the LDV experiments. In principle, the discrepancies between the FEA calculations and the experiments can be used to improve the modelling, which should include a better model for complex parts, such as the approach motors. Additionally, damping should be incorporated in a more sophisticated manner, for example, by measuring the frequency dependency of the damping
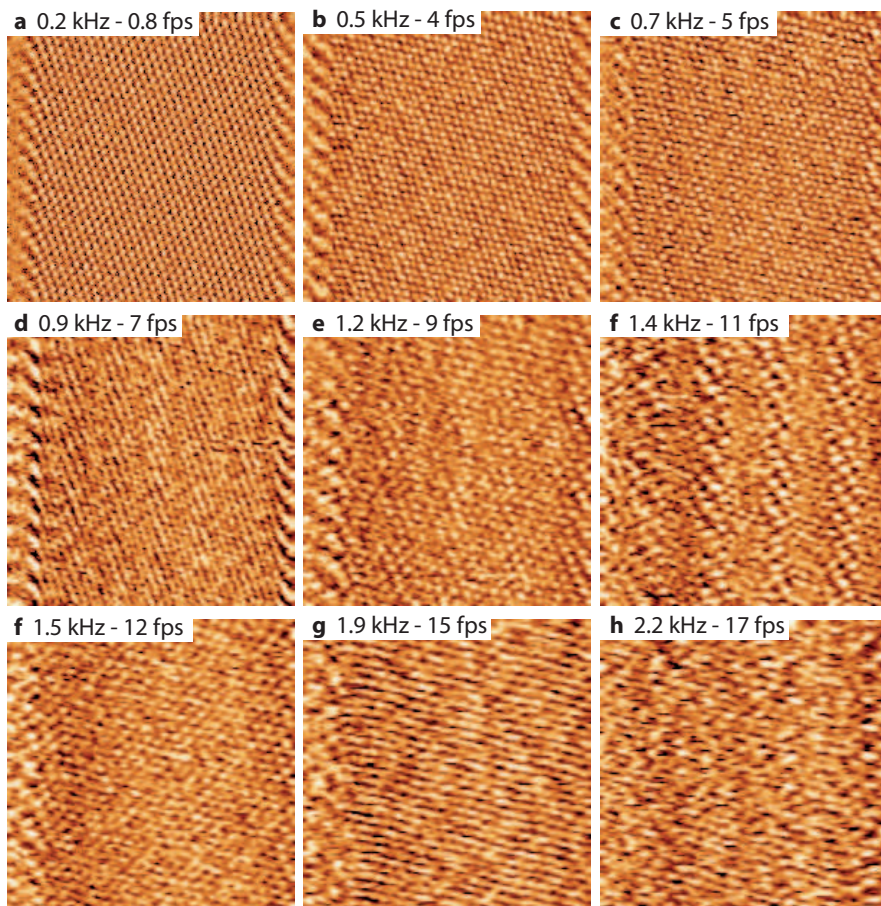
Figure 3.10:   STM images (10×10 nm^2; (a) 256×256 pixels^2 and (b-h) 128×128 pixels^2) of HOPG obtained in the hybrid mode (Section 1.3). The line frequencies and frame rates are indicated. The distortion at the edges is due to the use of a rounded triangle scan signal [29] and hysteresis in the piezoelectric material. The images all show atomic details, but with a different degree of distortion. In hybrid mode, the first minor distortion is visible as vertical bands in the image at a line frequency of 0.7 kHz. At 0.9 kHz, 1.4 kHz, and 1.9 kHz (the lowest resonance frequency) the distortion is considerable, but in between, at 1.2 kHz and at 1.5 kHz, the distortion is much less. Above the first resonance, at 2.2 kHz, the distortion is smaller than at resonance. Note that with increasing line frequency, in addition to the distortions of mechanical nature, the imaging becomes less clear because of the limited bandwidth of 50 kHz of the *IV*-converter used for these measurements.

of a sample of the material to be used. The ideal FEA modelling, which can be obtained by successfully optimizing the modelling as described above, would yield the perfect 'tool' for the design of SPMs.

The lowest eigenfrequency of the microscope is 1.9 kHz* and is, as was to be expected, related to the coarse approach mechanism. Due to the specific design of the microscope, we have been able to limit the transfer of the motion of the scanner to other parts of the microscope. This fact is most evidently recognized from the measurement of the minute displacements of the sample-holder, while the scanner was excited at one of its resonance frequencies. It has been proven to be possible to image with the new STM using a frame-rate in excess of 10 fps.

Video-rate STM, commonly defined as imaging with a frame-rate of 25 fps, and a resolution of at least 256×256 pixels^2 [82], requires a line frequency of 6.4 kHz. With our STM it should be possible to cross all approach motor related resonances, and scan just above 6.7 kHz, which is below the first bending resonance of the scanner at $\sim$12.5 kHz. When using a rounded triangle scan signal, also excitations around 20 kHz are to be considered, which is not expected to be problematic, see Ref. 46. A point of concern is the excitation frequency in the *z*-direction required for video-rate imaging in constant-current mode, which for a typical substrate recorded at 10×10 nm^2 is $\sim$250 kHz. This frequency is far above the *z*-resonance frequency of the tube scanner ($\sim$50 kHz [46]), and also above that of a conical scanner, which is $\sim$70 kHz [41]. A promising candidate for the *z*-scanning is the recently developed MEMS† *z*-stage, which has its first resonance frequency at 189 kHz [83]; these devices can have a fundamental frequency in excess of 1 MHz. The design of our STM allows the incorporation of a MEMS *z*-stage, or other types of high-frequency actuators.

It should be possible to lower the amplitudes of the vibrations of the sample-holder for the lowest eigenmodes by adding damping elements to the approach motors. However, if one aims to scan with a frequency between peaks, it is actually better to maximize the modal quality factor, as the frequency band for which the resonance constitutes a problem decreases with an increasing Q. As it is now, due to the width of the first resonance peak, around 1.9 kHz, this resonance already forms a problem above 1.6 kHz. Additional damping could lower that latter frequency.

Finally we note, that to decrease the effect of the transfer of the motion of the piezoelectric scanner, one could install a piezoelectric element identical to the scanner, 'upside-down', at the bottom of the base on which the scanner is mounted. This second scanner can counterbalance the forces exerted by the

---

*Note that presently a somewhat heavier sample-holder is installed. Hence a lower resonance frequency for the modes that are related to the piezoelectric elements in the approach motor, (a) and (b), is to be expected.

†Microelectromechanical systems.

motion of the primary piezoelectric scanner [84]*. Our STM has been designed such, that a counterbalancing scanner can be added. Care must be taken that the primary and secondary scanner have precisely the same mass and stiffness to ensure that no additional resonances are introduced[†].

---

*Note that when a second piezoelectric scanner is used to counterbalance the forces generated by the lateral scanning motion, the full compensation of the forces perpendicular to the base leads to the doubling of the forces parallel to the base, and *vice versa.*

[†]The mechanical properties of piezoelectric material change over time; this *ageing* can be slightly different for either piezoelectric scanner.

CHAPTER 4

Mo-silicide formation on Si(111)-7×7

Mo deposition by e-beam evaporation onto Si(111)-7×7 was studied with STM during the deposition process. Fast STM imaging, at an average frame rate of 0.5 frames per second, enabled us to follow the complex reactive nucleation, in which Mo-silicide is formed, with great detail. We find that initially the energy released in the clustering of at least two Mo atoms is required to overcome the energy barrier for silicide formation. The Mo-silicide nuclei that are formed comprise a considerable fraction of Si. The amount of Si is probably even as large as in $MoSi_2$, which implies an efficient transport of Si atoms during Mo deposition.

4.1   Introduction

As discussed in Section 1.2 the reflectivity of a Mo-Si multilayer mirror is lower than the theoretical maximum value of an ideal multilayer system, which is in part due to the existence of Mo-silicide (Mo_xSi_y) interlayers. There is an asymmetry in the thickness of the boundary layers: the silicide layer that forms when Mo is deposited onto Si, is thicker than the interlayer formed during deposition of Si onto Mo, as was found by many groups using both sputter deposition and e-beam evaporation to fabricate the multilayers [85–90]. The reported values for the thickness of the silicide interlayers range between 1.1 nm and 2.3 nm for the Mo-on-Si case and between 0.5 nm and 1.1 nm for the Si-on-Mo case. As the thickness of the Mo layer in a Mo-Si multilayer mirror for 13.5 nm radiation is ∼3 nm, the silicide fraction is appreciable. An important gain in reflectivity of Mo-Si multilayer systems can thus be achieved by a reduction of the thickness of the interlayer that forms when Mo is deposited onto Si. For this reason, the system has been widely studied, but an understanding of the atomic processes that govern the formation of Mo-silicide during Mo deposition is lacking.

From a fundamental surface science point of view, the Mo-Si combination is also interesting, as it provides the possibility to study growth processes in a complex, reactive system. The situation is deemed to be much more involved than growth on an inert substrate. This standard type of growth can be understood by conventional nucleation and growth models [91, 92]. These models describe the initial stages of epitaxial growth in terms of the deposition rate and the diffusivity of the deposited atoms under the assumption of a certain stable cluster size and have been shown to be particularly successful to describe growth on low-index metal substrates at not too high temperatures [93]. In non-reactive nucleation, the substrate merely forms the periodically corrugated energy landscape, on which deposited atoms diffuse and cluster. At most, the substrate atoms relax due to the bonding with the deposited atoms. A completely different situation has to be expected for reactive nucleation and growth.

In this chapter we present an investigation of Mo deposition onto Si and silicide formation using real-time STM. We show that we can extract important details of the process by imaging during deposition, especially as we employ the fast-scanning capabilities of our STM. Before presenting the experimental results, the concept of silicide formation during metal deposition is introduced in the next section.

4.2   Silicide formation

Over the past decades metal deposition onto Si has been widely studied. The use of the material combination in integrated circuits and Schottky diodes has stimulated both applied and fundamental research. Many metal-silicon combina-

tions have been probed with a multitude of techniques; a vast body of literature reports on the subject is available. Most metals deposited on Si engage in a chemical reaction with the substrate, even when no bulk silicides exist of the particular metal [94]. The silicide thus formed is not always considered a nuisance, as it finds its application as a metal-like conductor, which is stable at high temperatures and in oxidizing environments [95].

In what is known as a *contact* or *solid phase epitaxial* reaction, during deposition of the metal onto a Si substrate, a thin silicide film is formed, even when the temperature is as low as 300 K. The thickness of the silicide film is limited by the interdiffusion of the species*. Eventually, further deposition results in the overgrowth of a strictly metallic layer, as the silicide layer is forming a diffusion barrier for the Si atoms, thereby preventing further silicide formation. The silicide formation reaction naturally involves bond breaking and it is striking that already at temperatures as low as 300 K the strong covalent Si-Si bond ($\sim$2 eV) is broken by the presence of the deposited metal atoms [96]. Van Loenen *et al.* suggested that for Ni deposition onto Si, the energy release of the clustering of Ni is large enough to overcome the barrier of the silicide formation reaction [97]. In turn, this exothermic reaction fuels the Si surface diffusion required for the reaction. The reaction stops, as soon as the silicide film closes, and the Si supply to newly deposited Ni is blocked.

It was found for various transition metals, including Co and Fe, that the very first deposited atoms diffuse to a subsurface region in the initial stages of deposition onto a Si(111)-7$\times$7 substrate [98, 99]. Only if the concentration of interstitial metal atoms is high enough, the silicide formation reaction starts. This mechanism was proposed by Tu already in 1975 for Ni, Pt and Pd [100]. Bedrossian suggested a similar process for Mo atoms deposited onto Si(001)-2$\times$1 at 680 K [101].

Three stable bulk Mo-silicides exist: $MoSi_2$, Mo_5Si_3 and Mo_3Si. The formation reaction of all compounds is exothermic. $MoSi_2$ is the most stable form: the bulk free energy is lowest. See Ref. 102 for a binary alloy phase diagram and free energy values. To identify the stoichiometry of the compound formed during e-beam deposition of Mo onto Si(111)-7$\times$7 and Si(001)-2$\times$1 in the temperature range $\sim$300-500 K, Slaughter *et al.* used electron diffraction techniques, X-ray photoelectron spectroscopy (XPS) and Auger-electron spectroscopy (AES) [103]. It was found that the first deposited Mo was fully converted to a 0.4 nm thick amorphous $MoSi_2$ layer and that further deposition led to compounds with increasingly more Mo. After the deposition of $\sim$1 nm a polycrystalline structure was identified; upon further deposition the film showed traces of Si up to the maximum thickness of $\sim$2.5 nm. From the binary alloy phase diagram, for a Si fraction above 2/3, $MoSi_2$+Si is expected and in that sense the silicide that is richest in Si, is most likely to be formed in the initial stages of the deposition.

---

*The film thickness can be increased by enhancing the diffusivity by increasing the substrate temperature during deposition or by annealing of the sample afterwards.

On the other hand, it is not evident that at low substrate temperatures there is enough mobility to accommodate the reaction. The fact that $MoSi_2$ *is* formed, suggests that the energy release during the reaction locally heats the substrate enough so that diffusion is activated and every deposited Mo atom is converted into $MoSi_2$. Only after the deposition of a significant amount of Mo, the inter-diffusion of Mo and Si becomes the rate limiting step in the formation of $MoSi_2$. This can be due to the fact that the required diffusion length to accommodate the reaction increases, as, e.g., the transport is locally inhibited by the closure of the film. Consequently, other compounds that contain a larger fraction of Mo, are formed. This view is supported by the fact that for lower temperatures the Si fraction in the growing film decreases faster during deposition. Mo deposition onto Si substrates at higher temperatures results in the formation of crystalline silicide [104].

Here we present a study of Mo deposition onto Si(111)-7×7 at room temperature, which is the common substrate temperature in the production process of Mo-Si multilayer optics. Although in the case of actual multilayers the Si is in an amorphous state, we have chosen a single-crystalline substrate, as that allowed us to start from a well-defined, clean and flat surface, which enabled a rigorous, quantitative analysis of the experimental data.

4.3   Experiment

4.3.1   Details

A Si(111) sample was cleaned by degassing in UHV, followed by flash annealing to 1450 K; the usual 7×7 reconstruction was observed with STM [80, 105–109]. Mo was deposited by means of e-beam evaporation (see Chapter 2 for specifications of the e-beam evaporator) from a rod containing 99.95% Mo. The angle of incidence of the Mo beam was 75° from the surface normal. The deposition flux $d\Theta/dt$ was $8 \pm 2 \times 10^{-3}$ atoms nm^{-2} s^{-1}, which was calculated from data measured *in situ* prior to the experiment using a quartz-crystal microbalance (QCM). The angle of incidence onto the QCM was 15°. The sample was not intentionally heated, but due to the thermal radiation from the evaporation source the sample temperature during the experiment rose from 293 K to 310 K. The base pressure of the UHV-chamber was below 5×10^{-11} mbar. During deposition the pressure increased to 3×10^{-10} mbar. Constant-current STM images were recorded during the deposition at a sample voltage of +2 V and a tunneling current of 200 pA.

4.3.2   Results and discussion

To investigate the initial stages of the deposition with maximum temporal resolution, we utilized the fast scanning capabilities of our STM. During the deposition of Mo, up to a coverage $\Theta = 1.8$ atoms nm^{-2}, images were taken at a frame rate of 0.6 frames s^{-1} (fps). After that, as the roughness had increased and the imaging had to be slowed down slightly to track the surface, up to $\Theta = 7.7$ atoms nm^{-2}, the imaging rate was 0.4 fps. The resulting STM movies are available as supplementary material [110, 111]; Figures 4.1 and 4.2 show frames from both movies.

The STM images show that during the deposition of Mo the surface structure changes by the formation of clusters on top of the initial Si surface. In addition, in the close vicinity of these clusters, most commonly within one 7×7 unit cell, material appears to be removed from the top Si surface layer. From this 'active' participation of the substrate material we infer that the nucleation of the clusters is reactive and that the nuclei are most likely Mo_xSi_y. The precise stoichiometry of the compound clusters is difficult to obtain from the STM images, as we will explain by the following effort, in which we estimate the composition.

With respect to the initial Si surface, the measured height of the clusters is ∼0.1 nm. From the STM images, we cannot assess how thick the silicide nuclei are: we do not know how far the clusters extend below the initial Si surface, but we assume that in the initial stages the clusters are of monolayer thickness. The thickness of a Mo_xSi_y monolayer depends on the arrangement of the Mo and Si atoms, which we do not know and is most likely not precisely the same for all nuclei. To be able to proceed, we coarsely estimate the nuclei to extend as far below as above the initial Si surface and so we assume a thickness of 0.2 nm[*]. The expected number of Si atoms per unit area in a silicide nucleus of that thickness is 10 nm^{-2} for $MoSi_2$, 5.3 nm^{-2} for Mo_5Si_3, and 3.4 nm^{-2} for Mo_3Si. If we assume that the deposited Mo atoms can react with the Si surface atoms, these numbers must be compared to the density of Si surface atoms in Si(111)-7×7. Per unit cell, the 7×7 reconstructed Si(111) surface has 54 surface atoms, of which the outermost 12 are the adatoms [80, 105]: the density of Si surface atoms is 8.7 nm^{-2}.

Of the three silicides, only the formation of $MoSi_2$ requires more Si atoms per unit area than are available in the Si surface, and hence for the formation of this particular silicide more Si atoms must be be transported to the silicide nucleus. The scenario we can imagine to occur, is that in addition to the reaction of the Mo atoms with the Si surface atoms at the location of a nucleus, from the vicinity the weakly bound Si adatoms diffuse to the clusters. The removal of these adatoms from their original positions is what we observe as the formation of shallow holes in the Si surface, with an average depth smaller than 0.1 nm. From the STM

---

[*]This value should be close to the thickness of a Mo_xSi_y monolayer, but for the following argumentation, the precise thickness is not of critical influence.

Figure 4.1: STM images ($28.5 \times 28.5 \times 0.25$ nm^3) taken during the deposition of Mo onto Si(111)-7×7. Images (a-f) show the surface after a Mo coverage of respectively 0, 0.3, 0.6, 0.9, 1.2 and 1.5 atoms nm^{-2}. Besides the formation of clusters on the surface, holes in the substrate are visible. The holes indicate that Si has actively participated in the nucleation, i.e. that a chemical reaction has taken place and that the clusters are Mo$_x$Si$_y$. The images were taken from an STM movie [110] and show approximately the same surface area. In (a) three 7×7 unit cells are indicated.
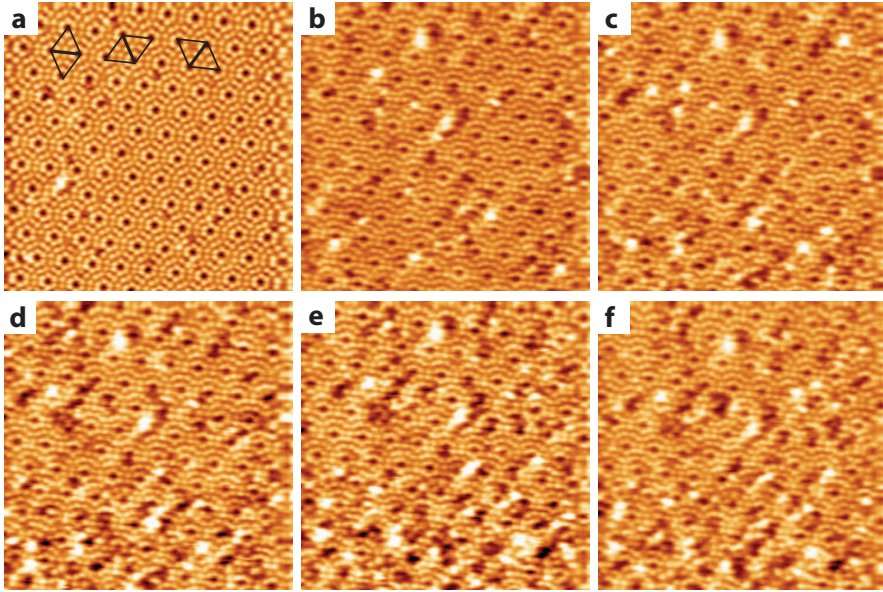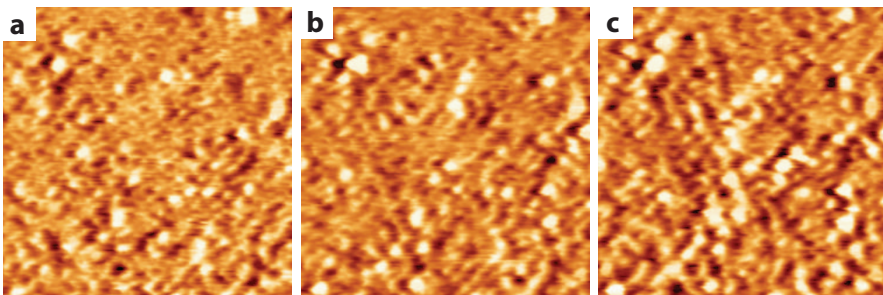

Figure 4.2: STM images ($25 \times 25 \times 0.25$ nm^3) taken during the deposition of Mo onto Si(111)-7×7. Images (a-c) show the surface after a Mo coverage of respectively 2.0, 3.6 and 5.2 atoms nm^{-2}. The images were taken from an STM movie [111] and show the same surface area.

images we can extract the areal density of the clusters ϕ_c and of the holes ϕ_h. On average, during the nucleation process we find $\phi_h/\phi_c = 0.7 \pm 0.1^*$. As the Si adatom density is 1.9 nm^{-2}, on average 1.3 adatoms diffuse to a silicide nucleus of 1 nm^2. The total number of Si atoms (8.7 nm^{-2}+1.3 nm^{-2}) matches the required amount of Si atoms in a MoSi$_2$ nucleus. As the deposition continues and the amount of '7×7-adatoms' decreases, we expect that other atoms, which have become weakly bound in the nucleation process, can diffuse to a Mo-silicide cluster.

We cannot be absolutely certain that MoSi$_2$ is formed according to this scenario, but on the basis of earlier research, e.g. as described in Refs. 90 and 103, the formation of MoSi$_2$ is to be expected in the initial stages of the deposition. In any case, on the basis of our observations, we are confident that a silicide that comprises a significant amount of Si, is formed and that the surface diffusion of Si atoms accompanies this formation. The formation of a silicide containing a relatively large amount of Mo, should have a less 'destructive' influence on the Si surface structure. For example, the formation of a 0.2 nm thick Mo$_3$Si cluster requires initially little more than the binding of the Mo atoms to the 'reactive' adatoms and *rest atoms* of the Si(111)-7×7 surface. The adatoms and rest atoms are reactive in the sense that these atoms have one atomic bond unsatisfied. The *dangling bond* density on a Si(111)-7×7 surface is 2.9 nm^{-2} and is just below the required 3.4 Si atoms nm^{-2} for a 0.2 nm thick Mo$_3$Si cluster. If during the initial stages of the deposition silicides that contain a relatively large amount of Mo, would be formed, we should not expect to observe the formation of a significant amount of depressions in the Si surface.

In Figure 4.3 the number of clusters per unit area is plotted versus Θ. During deposition the cluster density increases to a maximum, the nucleation density, at a coverage of 7.7 atoms nm^{-2}. Further deposition leads to a decrease of the density of clusters, as clusters merge. The evolution of the surface morphology after the nucleation stage is the subject of Chapter 5. Even in the earliest stages of the experiment, the number of clusters is lower than the number of deposited atoms. This implies that single Mo atoms do not react with the substrate to form a silicide and that the energy that is released in the clustering of two or more Mo atoms is required to overcome the energy barrier for the silicide formation reaction. This energy, which is a fraction of the bulk value of the cohesive energy of Mo†, 6.2 eV/atom [112], may be sufficiently high to overcome the activation energy barrier for the silicide formation reaction. The energy barrier for the reaction should be close to the Si-Si bond strength and is 2.4 eV for bulk

---

*This analysis was carried out using images that showed a reasonable amount of the initial surface, which was used as a reference plane. Due to tip convolution ϕ_c is overestimated, whereas ϕ_h is underestimated. Thus the retrieved value for ϕ_h/ϕ_c represents an lower limit. Furthermore, as the tip is not infinitely sharp, the depth of the holes may not be correctly measured, i.e. in reality be deeper than measured.

†As Mo is a bcc crystal the dimer bond energy should be of the order of 1/4 of the Mo cohesive energy per atom.

Mo-silicide [113]*.

Figure 4.4 shows the state of the surface at $\Theta = 7.7$ atoms nm^{-2}. From the autocorrelation function $C_A(\mathbf{r}, t)$[†] of the STM image (inset) we find that the $Mo_x Si_y$ nuclei are dispersed according to the 7×7 Si(111) superstructure; on average each Si(111)-7×7 unit cell contains one nucleus. How does the 7×7 superstructure act as a template during the nucleation process?

On the atomic level the Si(111)-7×7 surface is rougher than most substrates, which is due to the surface reconstruction. The deep corner hole and the 'trench' between the faulted and unfaulted halves of the unit cell contribute to this roughness. As a consequence, the energy barriers for diffusion, especially beyond one half unit cell, are high. At a sufficiently low substrate temperature, deposited atoms will be confined to the half unit cell onto which they were deposited. Figures 4.1(b-f) show clusters, which were formed on the boundary of two half unit cells, as well as clusters that are confined to one half of the unit cell. The mechanism we propose is that two, or more, Mo atoms need to be present in the same half unit cell, or in adjacent half unit cells (one full unit cell), to cluster. Clusters grow by the deposition of Mo atoms onto 'their' unit cell. To test this hypothesis, we calculated the cluster density as a function of the number of deposited Mo atoms using a simple model: nucleation occurs when the required number of Mo atoms i has arrived in one unit cell. In Figure 4.3 the calculated evolution of the cluster density is plotted for $i = 2$, 3 and 4. For completeness also the case $i = 1$ is considered.

A comparison between the modelling and the experimental data shows that the model is too simple to explain all the details of the nucleation process. In reality the cluster density is not monotonically increasing, as we observe that on some occasions a small cluster breaks up. Furthermore, the surface is changed by the consumption of Si in the silicide formation reaction. This effect is not incorporated in the modelling, but should be of least influence in the very beginning of deposition, on the basis of which we may speculate that i is 2 or 3. We refrain from any further attempts to precisely construct the complex nucleation process, as this would overstretch the boundaries of validity of our modelling, but it seems safe to assume that at least two Mo atoms must meet in order to form a Mo-silicide nucleus. A similar result was obtained for Ti deposition onto Si(001) and the formation of $TiSi_2$, where i was found to be larger than 1 and estimated to be in the range of 2-5 [114].

---

*We expect that the energy barriers for the diffusion of Si on Si and of Si on the silicide are lower than the barrier for the breaking of Si-Si bonds and that therefore the latter dominates the process in the early stages. Later, as the growth of the silicide film requires the diffusion of Si over a larger distance, the diffusion becomes the rate limiting step to form $MoSi_2$, and other compounds with a larger fraction of Mo are formed.

[†]The 2D-autocorrelation function $C_A(\mathbf{r}, t)$ is defined as $C_A(\mathbf{r}, t) = \langle (h(\mathbf{x}, t) - \bar{h}(t))(h(\mathbf{x} + \mathbf{r}, t) - \bar{h}(t)) \rangle$ in which $h(\mathbf{x}, t)$ is the height of the surface at position $\mathbf{x}$ and at time t, $\bar{h}(t)$ is the mean surface height at time t, and the angle brackets indicate spatial averaging at time t. The properties of $C_A(\mathbf{r}, t)$ are further explored in Section 5.3.
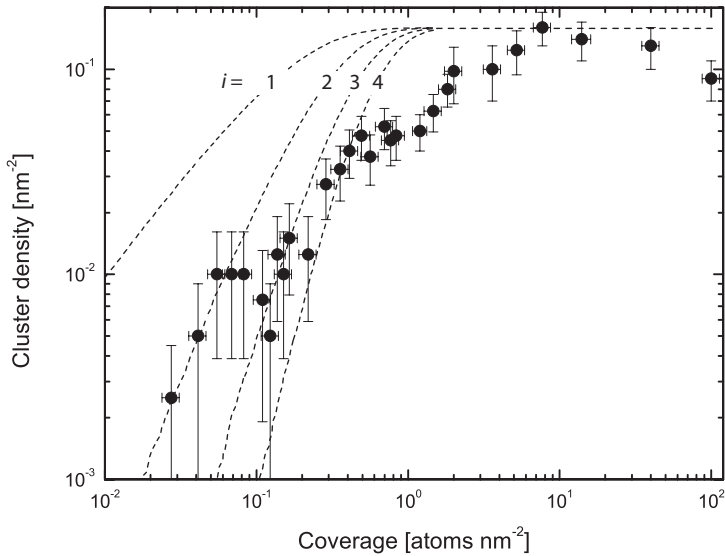
Figure 4.3: The data points show the cluster density plotted versus the Mo coverage. The vertical error bars reflect the error that can be expected from the fact that the number of nuclei was assessed on a small area, which we estimate to be the square-root of the number of counted clusters divided by the sampling area. The lines are calculated cluster densities, on the basis that $i = 1$, 2, 3 or 4 Mo atoms must be present in a Si(111)-7 $\times$ 7 unit cell to form a silicide nucleus.
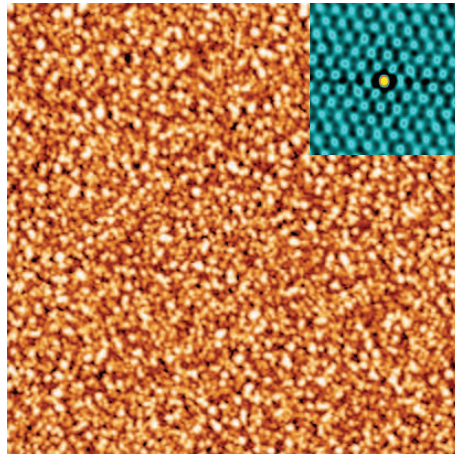
Figure 4.4: STM image ($75 \times 75 \times 0.36$ nm^3) of Mo deposited onto Si(111)-7$\times$7 at a coverage of 7.7 atoms nm^{-2}. The inset shows the autocorrelation function $C_A(\mathbf{r}, t)$ of the image (window size is 25×25 nm^2; $\mathbf{r} = 0$ is at the center of the image). From this we derive that on average each Si(111)-7$\times$7 unit cell contains one Mo$_x$Si$_y$ nucleus.

Finally, we address the question about the whereabouts of the non-reacted Mo atoms. It appears that these atoms are 'missing', as we do not observe them in the STM images. It may be that single Mo atoms diffuse to a subsurface region, as has been suggested for other transition metals [94]. This would, however, not explain why there is approximately one silicide nucleus per 7×7 unit cell, because if Mo atoms indeed diffuse subsurface, there is no obvious reason that they are bound to a half unit cell: the binding energy should be approximately equal everywhere, and the diffusion consequently homogeneous. Therefore, it is likely that single Mo atoms diffuse on the half unit cell too fast for the STM to capture their movement, or are located in the trenches and corner holes, where they remain 'invisible' for the STM until they form a small cluster and react with the Si.

4.4   Conclusions and further remarks

By combining fast scanning and 'imaging during deposition' we were able to follow the initial stages of Mo deposition onto Si(111)-7×7 in detail [110, 111]. The growth is reactive as could be directly inferred from the participation of the substrate in the formation of the nuclei. From a measurement of the number of clusters as a function of the number of deposited atoms, we found that at least two Mo atoms must cluster to start the silicide formation reaction. Apparently, the energy released in the clustering of Mo atoms is required to start the silicide formation reaction.

Although the 7×7 superstructure plays a significant role in the nucleation density of the silicide nuclei, the mechanism through which the silicide forms on amorphous Si substrates, should be very similar, as it is dominated by the chemistry of the interaction of Mo and Si. Also in the case of an amorphous Si substrate will there be dangling bonds, which helps in the silicide formation, as well as covalent Si-Si bonds that need to be broken in order to form the silicide. It is important to realize that an experiment, similar to the one presented in this chapter, on an amorphous Si substrate could not have yielded such detailed information as the present study. It would have been difficult to observe ∼0.1 nm deep holes and similar sized protrusions on a substrate that would show such height variations intrinsically, i.e. prior to deposition.

A coarse estimate of the Mo-Si ratio of the formed clusters points towards a compound that is rich in Si content. The fact that the clusters comprise a significant amount of Si, probably as much as in $MoSi_2$, implies that the supply of Si is not limited in the initial stages of deposition. In view of the negative effect of the silicide formation on the performance of multilayer optics this is bad news. If the supply of Si could be inhibited somehow, the silicide interlayer would be thinner. One expects that an increase of the Mo deposition rate could make the diffusion of Si the rate-limiting step in the formation of Mo_xSi_y. However, an

increase by a factor of $\sim 10^3$ is not enough, because even then MoSi$_2$ is formed, as was investigated with XPS [115].

Another technique, besides e-beam evaporation and sputter deposition, that has been used to fabricate Mo-Si multilayers, is pulsed laser deposition [116, 117]. The advantage of PLD is the high supersaturation following the pulse that can lead to a large nucleation density, and therefore to a fast closure of the film. Consequently the thickness of the silicide can be minimized. A disadvantage of PLD, with respect to the silicide formation, results from the energy transfer to the surface when using PLD, which is much larger than when using e-beam evaporation. Not only the energy of the deposited atoms, which is significantly greater in the case of PLD, also the energy released in the condensation of large quantities of Mo may heat the surface significantly resulting in an increased diffusion and silicide formation. High-resolution transmission electron microscopy (HRTEM) images of Mo-Si multilayers fabricated using PLD do show interlayers with a significant thickness between Mo-on-Si [117]. Interestingly, the authors of Ref. 117 find no significant interlayer between Si-on-Mo. This observation indicates that for Mo-Si multilayers produced by PLD the formation mechanism for the silicide layer differs for the Mo-on-Si and the Si-on-Mo cases, as was also found for other deposition techniques [90].

As the interdiffusion of Mo and Si is a thermally activated process, it seems sensible that Mo-Si multilayers deposited onto cooled substrates, should suffer less from interlayer formation. In fact, recent results of multilayers deposited by e-beam evaporation onto a substrate cooled with liquid N$_2$, show that the interlayer thickness could be decreased significantly, compared to multilayers produced at room temperature [118]. The authors of Ref. 118 find a reduction of the interlayer thickness of ~ 0.9 nm per period, i.e. this reduction of $\sim 60\%$ is the sum of the decrease in thickness of the Mo-on-Si and of the Si-on-Mo interlayer. The fact that even at liquid N$_2$ temperatures a silicide is formed is interesting in itself, if the following is considered. The silicide formation reaction is a complex chain of thermally activated events, on which the total reaction rate and the interlayer thickness depend. The rate ν at which a single event, that requires an activation energy E_b, occurs is given by:

$$\nu = \nu_0 \exp\left(-\frac{E_b}{k_b T}\right), \qquad (4.1)$$

in which T is temperature, k_b is Boltzmann's constant and ν_0 is the attempt frequency, which can be as high as 10^{13} Hz for the diffusion of a single atom. In a chain of thermally activated events, the effective value of ν_0 may be much lower, as it incorporates the influence of the required combination of subsequent processes. The energy barrier for surface diffusion of Si on the growing Mo-silicide surface was estimated to be 0.2 eV [88]. Even for this relatively low energy barrier, the ratio $\nu(293\,\text{K})/\nu(77\,\text{K})$ is extremely large: $> 10^9$. So, the fact that the reported difference in interlayer thickness is quite small, is an indirect proof of the fact that not only the substrate temperature, but also the energy released in

the adsorption and the binding of the Mo atoms, as well as the exothermic energy of the silicide formation reaction determine the interlayer thickness, which is in line with our conclusions. It would be very interesting to infer how the reduction of thickness is distributed between the Mo-on-Si and the Si-on-Mo interlayers. The mechanism of formation of either interlayer is expected to be different, and so one also expects that their temperature dependences differ.

For both the Mo-on-Si, as well as for the Si-on-Mo interlayer, the predominately diffusing species during the silicide formation is expected to be Si [90]. When Mo is deposited onto Si, Mo_xSi_y is formed, which requires the surface diffusion of Si from those parts of the substrates that are uncovered. The diffusion is thermally activated and the local temperature depends on the global substrate temperature and the heat released in the processes that lead to silicide formation. When the Mo-silicide film closes, the transport of Si has to occur through bulk diffusion over a significant distance, which we expect to be very slow at room temperature. When Si is deposited onto a Mo surface, the silicide formation requires that Si atoms diffuse into the Mo layer, which should be easiest at the location of the Mo grain boundaries. After a thin Mo-silicide layer has formed, deposited Si atoms must diffuse through this layer. The energy barriers for bulk diffusion and for diffusion through grain boundaries are generally larger than the barrier for surface diffusion, which may explain the difference in thickness of the Mo-on-Si and the Si-on-Mo interlayers. In addition, regarding the temperature dependence discussed in the previous paragraph, it might not come as a surprise if at sufficiently low substrate temperatures the Si-on-Mo interlayer is completely absent, as the Si bulk (or grain boundary) diffusion is almost completely inhibited. However, even at low substrate temperatures, the Mo-on-Si interlayer may still be of a considerable thickness, as the Si surface diffusion is still fuelled by the heat release of the silicide formation process.

The difference in thickness of both types of silicide interlayers can also be understood by considering the free energy of the various interfaces during the deposition. The balance between the surface free energy of the deposited material γ_d, of the substrate γ_s, and the free energy of the interface between the deposit and the substrate γ_{sd} determines the *wettability* of the substrate for the particular deposit. Perfect wetting corresponds to the spread of the deposited material on the substrate and occurs when $\gamma_d < \gamma_s - \gamma_{sd}$. If on the other hand $\gamma_s < \gamma_{sd} - \gamma_d$, the substrate is said to be totally non-wetting for the deposited material and 'balling-up' of clusters of the deposit on the substrate is observed. In between these two extremes, the contact angle θ_c of a cluster of deposited material with the substrate can be evaluated using Young's equation [119]:

$$\cos\theta_c = \frac{\gamma_s - \gamma_{sd}}{\gamma_d}. \tag{4.2}$$

In the case of perfect wetting $\theta_c = 0°$. The surface free energy of Mo γ_{Mo} is considerably larger (factor ∼2) than the surface free energy of Si γ_{Si} [120–122]. For the sake of the argument, we neglect for a moment that the deposition of Mo

and Si onto respectively Si and Mo substrates is accompanied by the formation of Mo-silicide. By using Equation 4.2, we find that in the case of the deposition of Mo onto Si, θ_c is considerably larger than for the reverse case[*]. The driving force of the Mo-silicide formation when Mo is deposited onto Si is the lowering of the surface free energy as $\gamma_{Mo_xSi_y} < \gamma_{Mo}$ [123]. Because $\gamma_{Mo_xSi_y} > \gamma_{Si}$, also Mo-silicide clusters are expected to have a large θ_c with the Si substrate[†]. The non-wetting of Mo and of Mo-silicide on Si causes that during the deposition of Mo onto Si the film closes only slowly and that consequently the thickness of the interlayer that forms, is considerable. For the growth of Si, or Mo-silicide, on a Mo substrate the situation is different. In this case the deposit wets the substrate and the film is expected to close quickly and the interlayer thickness is modest. In order to increase the wettability of the Si surface for Mo and consequently decrease the interlayer thickness, one might alter the surface free energy of the substrate prior to or during deposition, by using a surfactant. This could be achieved by the exposure of the system to a particular gas, or by the deposition of a solid state surfactant, e.g. a small amount of some metal or a carbon-compound, before depositing Mo.

Another option to prevent intermixing during fabrication and application of Mo-Si multilayer optics is the compromise of depositing thin diffusion barriers of yet another material, such as B_4C, between the layers [124, 125]. Although also these interlayers diminish the performance of the optics for the same reasons a silicide interlayer does, the effect is less as the layers can be kept extremely thin, while still acting as a barrier. To optimize their performance, recent research has focused on the microstructure of the barrier layers, which is different when deposited onto Mo than onto Si [126]. We suggest that a real-time STM investigation, similar to what has been reported on in this chapter, could yield key details of the formation of the barrier layers. It may also be that B_4C acts as surfactant, rather than as a barrier for diffusion.

The final steps towards the ultimate performance of a Mo-Si multilayer are difficult to take and a combination of the approaches discussed here may be required. Perhaps it turns out that the deposition of the Mo layer should be preceded by the deposition of a diffusion barrier or a surfactant, whereas cooling of the substrate might be sufficient to inhibit the formation of the Si-on-Mo interlayer[‡]. Even if the problem of intermixing were to be totally annihilated, the reflectivity of a Mo-Si multilayer mirror is still below the theoretical maximum, because of interface roughness. To understand the origin of the roughness of the Mo layer, the deposition of a complete layer has been studied. The results are presented in the next chapter.

---

[*]We can even expect full wetting of Si on Mo, depending on γ_{sd}.

[†]The precise value of θ_c depends on the free energy of the Mo_xSi_y-Si interface.

[‡]Deposition at cryogenic substrate temperatures may cause additional stress in the multi-layer system at room temperature, which results from the difference in the expansion coefficients of Mo and Si.

Polycrystalline Mo thin film growth

The growth of a polycrystalline Mo film was imaged using STM during its deposition onto Si(111)-7×7. During deposition the interface width $w(t)$ and the lateral correlation length $\xi(t)$ evolve with time t as $w(t) \propto t^\beta$ and $\xi(t) \propto t^{1/z}$, with $\beta = 0.49 \pm 0.02$ and $1/z = 0.34 \pm 0.02$. The Hurst exponent H was determined to be 0.79 ± 0.04, and so $H \neq \beta z$. This implies that the growth cannot be described by self-affine scaling. As the height variations grow faster than the in-plane feature size, $\beta z > 1$, the growth mode exhibits *super-roughening*. We suggest that the origin of this type of growth is an impassable grain boundary crossing barrier: in the presence of a high-energy grain boundary, deposited atoms are bound to the grain onto which they were deposited and smoothing by diffusion is thus limited. The super-roughening growth of Mo on Si seems to be unrelated to the choice of the specific Si substrate, as the same growth mode is found on a Si substrate of which the crystalline order of the surface was destroyed by ion erosion. In view of the application of Mo thin films on Si in Mo-Si multilayer optics, the super-roughness is unwanted: interface roughness reduces the reflectivity. If the diffusion across grain boundaries were to be enabled during deposition, this would lead to a significantly smoother film: there is room for improvement of the reflectivity of Mo-Si multilayer optics.

5.1 Introduction

In the previous chapter we presented an investigation of the initial stages of Mo deposition onto Si and the formation mechanism of Mo-silicide. For Mo-Si multilayers the formation of silicide interlayers during fabrication diminishes the reflectivity of the finished mirror. A similar degradation of performance, as was discussed in Section 1.2, is caused by the fact that the Mo and Si layers do not grow perfectly flat [127, 128]. In contrast to the Mo layer, the roughness of the Si layer can be effectively decreased by ion sputtering of the deposited film [129]. A further gain in reflectivity of Mo-Si multilayer systems can thus be achieved by using a deposition procedure or post-deposition treatment that would result in a reduction of the roughness of the (polycrystalline) Mo layer. In order to understand the origin of the roughness that evolves when Mo grows on Si, Mo films were deposited by e-beam evaporation to a thickness that is relevant for EUV optics, see Section 1.2. With real-time STM, the film growth of the same surface area was completely captured. The experiments presented in this chapter do not only add to the 'knowledge base' of how Mo grows on Si, they are of general importance, as there are but very few experiments where the growth of a film of a significant thickness is captured with STM *during* deposition[*].

Before presenting the experimental results in Section 5.5 and discussing the relevance of out results for industrially produced Mo-Si multilayer optics in Section 5.6, in Sections 5.3 and 5.4 a mathematical description of growing interfaces is introduced, which is required for a quantitative analysis of the evolution of the morphology of thin films. In the next section we briefly discuss what is known about the structure of the Mo layer.

5.2 Mo thin films

The interest in Mo thin films has been mainly deriving from their importance in Mo-Si multilayer structures. Mo films and layers in multilayer structures have been studied using a variety of techniques. Probably best known are the cross-sectional transmission electron microscopy (TEM) images of thinly sliced Mo-Si multilayer structures, of which examples are ubiquitous in the literature, see e.g. Ref. 130. From these TEM measurements it is concluded that the Si layer is amorphous, whereas the Mo layer is polycrystalline and highly (110)-textured [85].

In addition to TEM, X-ray techniques are used to characterize the Mo and the Si layers. Grazing incidence X-ray reflection (GIXR) can be used to determine the thickness of the layers, and wide-angle X-ray diffraction (WAXRD) allows the study of the crystallographic structure. Using WAXRD, Bajt *et al.* inferred

---

[*]For an example we refer to Ref. 40.

from the absence of the (110)-peak that the Mo layers are amorphous below a critical thickness [131]. They used sputter deposition to fabricate the multilayers and reported on an amorphous-to-crystalline transition of the Mo layer around a layer thickness of 2 nm. In the mechanism for the transition that is given in Ref. 131, a certain critical thickness of the Mo layer that depends on the amount of embedded Si in the growing film, is required to trigger the crystallization of the Mo layer. The transition was found to be accompanied by a maximum in the roughness of the surface of the Mo layers: both thicker and thinner Mo layers were less rough. The roughness was measured on the surface of multilayer stacks of 40 bilayers, for different values of the thickness of all Mo layers. The transition is local, as it only starts at some parts in the film where, due to the roughness of the amorphous layer, the critical thickness is reached. At the transition, as some parts are crystalline and others amorphous, the surface roughness is considerably larger than that of a completely amorphous or completely polycrystalline film. An amorphous-to-crystalline transition was also identified by Fillon *et al.* by measuring the evolution of the stress in the film during sputter deposition [132]. After the deposition of 2.2 nm Mo, following a sudden and transient stress change, an increase of the tensile stress was observed. Interestingly, Van de Kruijs *et al.* produced Mo-Si multilayers by e-beam evaporation and found no amorphous-to-crystalline transition for the Mo layer [130]. Rather, they inferred that the crystallization sets in directly from the Mo-Si interface, initially by the formation of a polycrystalline Mo-silicide.

5.3 Description of thin film surface morphology

5.3.1 Film thickness and roughness

The surface morphology of a film can be described by the local height $h(\mathbf{x}, t)$, which is the distance between the surface and a reference plane at an in-plane location $\mathbf{x}$ and at time t^*. The reference plane is usually the substrate onto which the film is deposited. The mean surface height $\bar{h}(t)$ is given by

$$\bar{h}(t) = \langle h(\mathbf{x}, t) \rangle, \tag{5.1}$$

where the angle brackets are used to indicate spatial averaging. Planar microscopy techniques are not suited to directly measure $\bar{h}(t)$ if the film is closed, i.e. if the substrate is fully covered[†]. In principle, with a real-time STM approach, in which the same surface area is continuously probed during deposition, one can

---

[*]The function $h(\mathbf{x}, t)$ is single-valued, and hence cannot be used to describe a surface with 'overhangs'.

[†]With an STM, or another scanning probe microscope, one can try to locally remove the deposit by 'scraping' it away with the tip to measure the thickness of the film directly [133]. The success of this approach depends on the hardness of the deposit with respect to that of the tip material.

obtain $\bar{h}(t)$ directly. As the film grows, the average tip height directly yields the film thickness. In practice, however, the retraction of the tip, due to the growth of the film, can be overshadowed by thermal drift, the motion of the tip relative to the sample that arises when not all parts within the tip-sample loop have reached thermal equilibrium, and are slowly expanding or contracting. This effect is enhanced by the heating of the STM by radiation from the hot deposition source. The relative tip-sample velocity due to thermal drift can easily be a few orders of magnitude larger than the growth rate and is largest directly after the first exposure of the STM to the deposition source. The average film thickness is often indirectly available from the combination of the deposition time and a proper calibration of the deposition flux, using a quartz-crystal microbalance prior to or after an experiment. In fact, the quantity thus obtained is the nominal thickness $\tau(t)$, which is the mean film thickness assuming the film to have the bulk density; the actual density of the thin film can be different. As $\tau(t)$ is proportional to the amount of material deposited, at a constant deposition rate, $\tau(t) \propto t$ and $\bar{h}(t) \propto t$ if the density is constant throughout the film. For most applications of thin films the thickness is an important parameter, which can be controlled with great precision, with e.g. a quartz-crystal microbalance or by *in situ*-reflectometry [134]. In that sense it is more interesting to study deviations from the mean height $h(\mathbf{x}, t) - \bar{h}(t)$, which may influence the film properties. For simplicity, but without loss of generality, henceforth a moving reference frame, in which $\bar{h}(t) = 0$, is used.

No perfectly flat films exist; all surfaces are rough on the microscopic scale. Even the smoothest substrates, such as single-crystalline surfaces, exhibit atomic-scale roughness. The most common measure of roughness is the root-mean-square (RMS) roughness or interface width $w(t)$:

$$w(t) = \sqrt{\langle h(\mathbf{x}, t)^2 \rangle}. \tag{5.2}$$

As the thickness of a film increases during deposition, commonly also $w(t)$ increases; this effect is known as *kinetic roughening* and often the following relation is found:

$$w(t) \propto t^{\beta}. \tag{5.3}$$

5.3.2   Lateral correlation

The determination of the interface width does not complete the description of the surface morphology, as it does not provide information on the in-plane length scale, on which the surface is rough. The autocorrelation function $C_A(\mathbf{r}, t)$ can be used to extract this information from $h(\mathbf{x}, t)$. It is given by

$$C_A(\mathbf{r}, t) = \langle h(\mathbf{x}, t) h(\mathbf{x} + \mathbf{r}, t) \rangle, \tag{5.4}$$

from which it is clear that $C_A(\mathbf{0}, t) = w^2(t)$. The typical in-plane distance on which the surface is rough is the lateral correlation length ξ, which is defined

as the value of $r = |\mathbf{r}|$ above which surface heights are not correlated. So for $r \gg \xi$, $C_A(r, t) = 0$, as $\langle h(\mathbf{x}, t)h(\mathbf{x} + \mathbf{r}, t)\rangle = \langle h(\mathbf{x}, t)\rangle\langle h(\mathbf{x} + \mathbf{r}, t)\rangle = \bar{h}(t)^2 = 0$.

Closely related to the autocorrelation function, and in fact equivalent, is the height-difference correlation function $C_H(\mathbf{r}, t)$:

$$
\begin{aligned}
C_H(\mathbf{r}, t) &= \langle (h(\mathbf{x}, t) - h(\mathbf{x} + \mathbf{r}, t))^2 \rangle \\
&= \langle (h(\mathbf{x}, t))^2 \rangle + \langle (h(\mathbf{x} + \mathbf{r}, t))^2 \rangle - 2\langle h(\mathbf{x}, t)h(\mathbf{x} + \mathbf{r}, t)\rangle \qquad (5.5) \\
&= 2(w^2(t) - C_A(\mathbf{r}, t)).
\end{aligned}
$$

It is useful to calculate the height-difference correlation function, as an important morphological parameter can be extracted directly from the behaviour of $C_H(\mathbf{r}, t)$ for small r, where the function often is found to have a power law dependency [135]. For $r \gg \xi$ the value of $C_H(\mathbf{r}, t)$ follows directly from $C_A(\mathbf{r}, t)$. Thus[*],

$$
\begin{aligned}
C_H(r, t) &\propto r^{2H} \quad \text{for } r \ll \xi \\
C_H(r, t) &= 2w^2(t) \quad \text{for } r \gg \xi.
\end{aligned} \qquad (5.6)
$$

The parameter H with $0 < H \leq 1$ is known as the Hurst exponent or local roughness exponent.

There does not exist a unique definition of ξ [135–139]; it can be defined through $C_A(\xi, t) = w^2(t)/\mathrm{e}$ or $C_A(\xi, t) = 0$[†]. Another definition uses $C_H(r, t)$ to define the lateral correlation length; on a log-log plot of $C_H(r, t)$ versus r, the crossover between the two regimes in Equation (5.6) is found at the crossing of the horizontal line $C_H(r, t) = 2w^2$ and the power law fit for $r \ll \xi$. In this thesis the definition $C_A(\xi, t) = w^2(t)/\mathrm{e}$, which implies $C_H(\xi, t) = 2w^2(t)(1 - \mathrm{e}^{-1})$, is used. It is not uncommon that $\xi(t)$ increases during film growth. This *coarsening* often follows a power law[‡]:

$$
\xi(t) \propto t^{1/z}, \qquad (5.7)
$$

where z is referred to as the dynamical exponent.

5.4 Evolution of surface morphology

5.4.1 Scaling and self-affine growth

In principle, the evolution of the surface morphology during growth is fully captured by $h(\mathbf{x}, t)$, but the description can be simplified and generalized by using

---

[*]Note that in the literature also another definition of the height-difference correlation is used: $\sqrt{\langle (h(\mathbf{x}, t) - h(\mathbf{x} + \mathbf{r}, t))^2 \rangle}$, in which case also the dependency on r is different.

[†]For self-affine surfaces this definition may be useless as $C_A(\xi, t)$ is often found to asymptotically approach 0.

[‡]Naturally, the value of $\xi(t)$ depends on the definition one uses, but this should have no influence on power law dependency of $\xi(t)$ on t.

a scaling theory based on the fractal nature of thin films: many surfaces are identical viewed at different levels of magnification [135, 140]. The power law dependency of Equation (5.6) implies a statistical scaling invariance for an average height profile $h(x, t)$ for $x \ll \xi$ and $\epsilon x \ll \xi$:

$$h(\epsilon x, t) = \epsilon^H h(x, t). \tag{5.8}$$

The scaling is said to be self-similar for $H = 1$ and self-affine for $H \neq 1$. If during film growth the roughening and coarsening both exhibit power law behaviour (Equations (5.3) and (5.7)), the global roughness exponent α is defined as:

$$\alpha = \beta z. \tag{5.9}$$

Dynamical scaling, or self-affine film growth, is observed if the local and global roughness exponents are equal, $H = \alpha$. The nature of self-affine growth is a competition between random deposition leading to roughness and various smoothing mechanisms, which would lead to a perfectly flat surface in the absence of deposition noise. A continuum approach is used to capture the evolution of the local height using Langevin equations of the general form:

$$\frac{\partial h(\mathbf{x}, t)}{\partial t} = \Sigma(\mathbf{x}, t) + \eta(\mathbf{x}, t), \tag{5.10}$$

in which the randomness of the deposition enters through $\eta(\mathbf{x}, t)$, a Gaussian noise term. The smoothing term $\Sigma(\mathbf{x}, t)$ depends on the nature of the smoothing. For example, if surface diffusion is the dominant smoothing agent $\Sigma(\mathbf{x}, t) = -K\nabla^4 h(\mathbf{x}, t)$ [141, 142], and $H = 1$, $\beta = 1/4$, and $z = 4$ describe the evolution of the film: this continuum model is known as the *Mullins model* [135]. The continuum equation that has proven to be most successful in describing non-conserved*, self-affine growth is the *KPZ*-equation, after Kardar, Parisi and Zhang [143], in which

$$\Sigma(\mathbf{x}, t) = \nu\nabla^2 h(\mathbf{x}, t) + \lambda/2(\nabla h(\mathbf{x}, t))^2. \tag{5.11}$$

The first term models relaxation by a surface tension and the second term dictates growth along the local surface normal, i.e. conformal growth†. The exponents are analytically not accessible and were approximated numerically to be $H \approx 0.38$, $\beta \approx 0.24$, and $z \approx 1.58$ [140]. A description of other continuum models that describe self-affine growth, can be found in Refs. 135 and 140.

5.4.2   Mound formation

Although in many cases film growth can be described by self-affine scaling, there are also many cases in which it cannot [139]. A type of evolution that is dis-

---

*In the case of non-conserved film growth, the growth volume is not equal to the deposited volume. This type of self-affine growth can be expected at high temperatures when a significant fraction of the film evaporates during its deposition, or at very low temperatures when the absence of mobility leads to the inclusion of vacancies in the film [139].

†For the interpretation of ν and λ see Ref. 143.

tinctively different, even though it might, at first sight, seem similar, is mound formation, in which mounds (hills) with a typical separation distance $\lambda(t)$ grow on the surface*. It is important to realize that the lateral correlation length $\xi(t)$ for self-affine surfaces is not an intrinsic length scale of the surface; it is the length scale above which surface heights are not correlated. The value of $\xi(t)$ depends on the scale at which the surface is analysed. It is common practice to use the same statistical tools for mound formation as for self-affine scaling to characterize the growth. If the lateral correlation length is obtained from the lateral correlation functions $C_A(r, t)$ or $C_H(r, t)$, for mounded surfaces $\xi(t)$ is some fraction of $\lambda(t)$. From microscopy images that show a sufficiently large number of mounds, $\lambda(t)$ is also directly accessible.

The height-difference correlation function of a mounded surface shows a similar power law dependency on r for $r \ll \xi$ as $C_H(r, t)$ of a self-affine surface. For this reason, mounded surfaces are sometimes falsely interpreted as being self-affine. The distinction between the two is apparent from $C_H(r, t)$ (and $C_A(r, t)$) for $r \gg \xi$; in this domain the correlation functions of a mounded surface show an oscillatory behaviour owing to the existence of $\lambda(t)$. As with self-affine growth, during mound formation coarsening and roughening often follow a power law (Equations (5.3) and (5.7)). In general, for the case of mounding $\alpha \neq H$.

Mound formation can be caused by the presence of an *Ehrlich-Schwoebel (ES) barrier* [144, 145]. On a crystalline surface, an atom deposited on a terrace experiences an additional energy barrier for diffusion to a lower terrace: the ES barrier. As a consequence, the chance that an atom is incorporated in the upper step is larger than the chance of the atom diffusing to the lower terrace, which results in a net uphill diffusion current [146]. The continuum equation describing the evolution of the local height in the presence of a diffusion bias is given by [139]:

$$\frac{\partial h(\mathbf{x}, t)}{\partial t} = -\nabla \cdot \mathbf{j}(\mathbf{m}) - (-1)^n K (\nabla^2)^n h(\mathbf{x}, t) + \eta(\mathbf{x}, t), \qquad (5.12)$$

where $\mathbf{j}(\mathbf{m})$ is the destabilizing diffusion current due to the ES effect, which is a function of the local slope $\mathbf{m} = \nabla h$. For surface relaxation through surface diffusion $n = 2$. Depending on the functional form of $\mathbf{j}(\mathbf{m})$ the growth exponents can vary. Values β between $1/6$ and $1/2$ and $1/z$ between 0 and $1/3$ have been reported in the literature [139, 147–150].

Although an effective ES barrier always leads to mound formation, it is not the exclusive origin of this phenomenon. *Any* effect that leads to a net uphill diffusion causes a growth instability that leads to mounding. Even in the absence of an ES barrier, the attraction of an adatom towards an upward step results in a diffusion biased in the uphill direction [151]. The origin of this *step-adatom attraction* is the fact that, on some surfaces, the potential energy of an adatom is lower in

---

*Other growth modes that deviate from self-affine growth are step flow growth and layer-by-layer growth [139].

the vicinity of the step than at another location on the terrace, which increases the *capture radius* of the step. It was calculated by using solid-on-solid (SOS) models[*] that the specific nature of *step-edge diffusion* [154, 155] can lead to mound formation. The fact that an atom that diffuses along a step, experiences an additional energy barrier for diffusion at a kink position [156, 157] leads to an uphill current and consequently to mounding. As the diffusion barrier at kink positions is essentially the 2D analogue of the ES barrier, this particular growth instability is said to originate from the *Kink-Ehrlich-Schwoebel barrier*.

5.5   Mo film growth on Si substrates

5.5.1   Experimental details

Mo was deposited by means of e-beam evaporation (see Chapter 2 for specifications of the e-beam evaporator) from a rod containing 99.95% Mo onto a Si(111) substrate[†]; the angle of incidence of the Mo beam was ∼75° from the surface normal. The nominal growth rate $d\tau/dt$ was $1.3 \pm 0.2 \times 10^{-4}$ nm s^{-1}. This rate was calculated from data measured *in situ* prior to the experiment using a quartz-crystal microbalance (QCM). The angle of incidence onto the QCM was 15°. Due to the thermal radiation from the evaporation source the sample temperature during the experiment increased from 293 K to 310 K. The base pressure of the UHV-chamber was below 5×10^{-11} mbar. After an initial increase to 3×10^{-10} mbar, the pressure restored to 7×10^{-11} mbar during deposition. Constant-current STM images were recorded during the deposition at a sample voltage of $+2$ V and a tunneling current of 200 pA.

5.5.2   Deposition onto Si(111)-7×7

Figure 5.1 shows images from an STM movie that was recorded during the deposition of Mo onto Si(111) to a nominal film thickness τ of 4.0 nm. Note that also Figure 4.4 is part of the movie and shows the state of the surface at $\tau = 0.1$ nm. The complete movie is available as supplementary material [158]. The STM images show 3D cluster growth starting immediately at the nucleation stage. In the previous chapter we discussed the formation of a Mo-silicide layer during the initial stages of Mo deposition onto a Si substrate. The accepted view for many metal-Si systems is that the silicide formation reaction continues until the interdiffusion of the reactants is blocked [94]. At room temperature, in

---

[*]In SOS models, atoms are sequentially positioned at a random lattice position and on the basis of a set of 'rules' they diffuse to a certain position or stay at the initial location. Examples of SOS models are the Wolf-Villain (WV) and the Das Sarma-Tamborenea (DT) models [152, 153].

[†]The experiment was a continuation of the experiment described in Chapter 4.
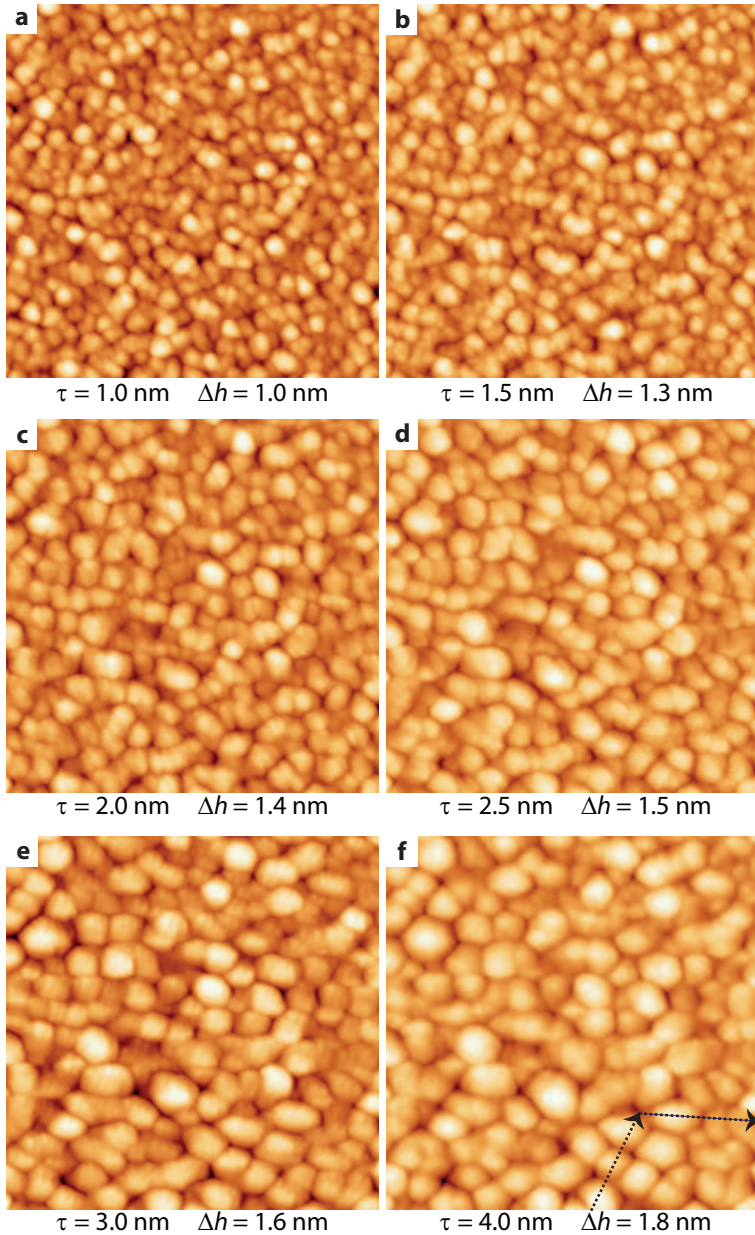
Figure 5.1: STM images ($50 \times 50 \times \Delta h$ nm^3 - Δh is indicated) taken during the deposition of Mo onto Si(111). The nominal thickness τ is indicated. The images were taken from an STM movie [158] and show the same surface area. The arrows in (f) indicate the path of the height profiles of Figure 5.3.
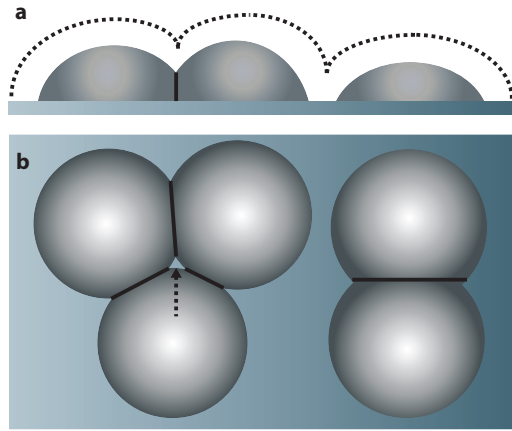
Figure 5.2: (a) Side-view of grains on a substrate. Between the two grains on the left a grain boundary has formed. The path the STM tip takes in constant-current mode is indicated by the dots: from a single STM height-line it is difficult to infer if two grains are touching. (b) From the top-view the local closure of the film can be seen by the formation of (straight) grain boundaries. The film closes latest at the triple-point indicated by the arrow.

the case of Mo-Si, the diffusing species is suggested to be Si [88, 90]. The Si atoms continue to diffuse to form a silicide until the silicide layer is closed. So an important question is: at what thickness is the film closed? From the STM movie the precise moment of closure cannot be determined, as it is impossible to judge with absolute certainty if two nuclei are very close together or are actually touching. The reason for this is that the STM tip is not infinitely sharp, and hence cannot probe the substrate between two grains if they are very close to each other. Figure 5.2(a) serves to illustrate this point. After the closure of the silicide film, further deposition of Mo is expected to result in the growth of a polycrystalline Mo film. At larger thicknesses, for example in Figures 5.1(e) and (f), the polycrystalline nature of the film is apparent from the grain boundaries that have developed; especially those that meet at 120° angles signify the polycrystallinity of the film. The moment of local closure of the film can in principle be determined by the moment a grain boundary is formed, which should be visible as a sudden disappearance of the sharp 'groove' between two grains, as the surface opening angle of a (low-energy) grain boundary is expected to be larger than the angle of the groove. Unfortunately, this identification requires the STM tip to be much sharper than it was during the present experiment. A coarse estimate, on the basis of the formation of straight lines between grains, which are presumably grain boundaries, is that between $\tau = 2$ nm and $\tau = 3$ nm most of the film is closed, although 'deep' *triple-points*, see Figure 5.2(b), are still visible for $\tau = 3$ nm. It is therefore not surprising that silicide interlayers in many Mo-Si multilayer systems have been reported to have a considerable

thickness [90]. Although the full closure of the film is expected to occur between a nominal thickness between 2 nm and 3 nm, the decrease of the number of clusters that is observed already after $\tau \sim 0.1$ nm, which corresponds to the situation in Figure 4.4, indicates that the merging of clusters starts at much lower τ, see Figure 4.3. Our observations of the growth of small clusters and a very slow film closure are consistent with the expected limited wetting of Mo on Si, as discussed in Section 4.4.

The average grain size increases during the experiment. At the relevant thickness for Mo-Si multilayers, $\tau = 3$ nm, the mean grain diameter is 4.5 ± 0.3 nm[*] and the interface width is 0.24 ± 0.02 nm. Figure 5.3 shows the evolution of a characteristic height profile; it shows that the number of polycrystalline grains at $\tau = 4$ nm is smaller than the number of nuclei. During local closure of the film, grain boundaries are formed between grains; some of these grain boundaries seem to disappear during further growth. Two mechanisms can lead to the merging of grains [14], which are both to be expected to occur during the growth of the Mo film. Firstly, the total free energy can be reduced effectively by the elimination of high-energy grain boundaries by their motion through a grain, an effect known as grain boundary migration. Secondly, it may only appear that two grains have merged, whereas in reality a low-energy grain boundary with a shallow surface profile exists between the grains. An additional effect is that the number of grains can be reduced by the overgrowth of a grain by its neighbours. It is difficult to distinguish between these effects, especially as grain boundary migration can occur much faster than the temporal resolution of STM: the activation energy for grain boundary migration, which depends on the specific type of boundary, can be very low: 0.1-0.3 eV [159]. See Figure 5.3 for a further discussion.

To analyse the Mo film morphology and its evolution during deposition systematically, the height-difference correlation function $C_H(r, t)$ was evaluated. The result is plotted in Figure 5.4. From $C_H(r, t)$ the local roughness exponent H, the interface width $w(t)$, and the lateral correlation length $\xi(t)$ were extracted. The evolution of H, $w(t)$, and $\xi(t)$ is plotted in Figure 5.5. During the experiment the local roughness exponent H slowly increases at first, until it becomes almost constant: $H = 0.79 \pm 0.04$, above $\tau = 1$ nm. After the deposition of ~ 0.25 nm Mo, $w(t)$ increases, whereas $\xi(t)$ increases almost directly from the start of the experiment.

We do not observe a clear peak in the evolution of $w(t)$ and so we cannot identify an amorphous-to-crystalline transition from a change of the roughness of the film, as was found for sputter deposited Mo-Si multilayers (see Section 5.2). One might speculate whether the data point at $\tau = 2.1$ nm is above the observed trend. In Ref. 131 a doubling of the roughness was determined around the tran-

---

[*]The mean grain diameter was determined by counting the number grains and determining the average area per grain, from which the average diameter was calculated assuming a simplified circular grain shape. Note, as we will explain in the following, that this is an overestimate of the actual average grain diameter, as two grains when separated by a low-energy barrier, may appear to be one if the shallow barrier is not resolved.
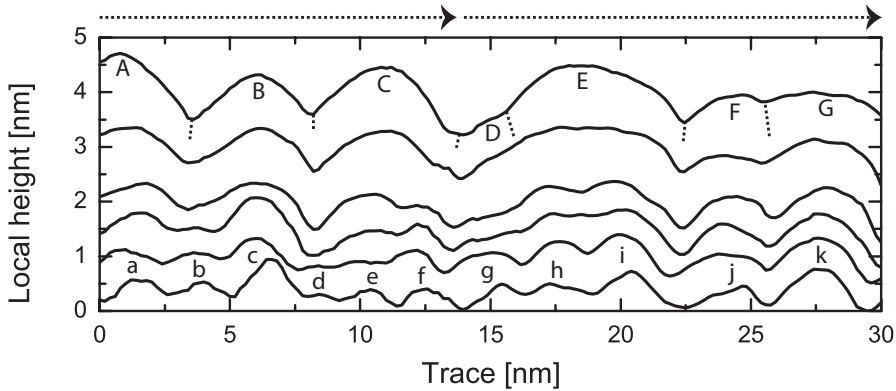
Figure 5.3: Evolution of the height profile indicated by the arrows in Figure 5.1(f). The height profiles are offset by the corresponding nominal thickness τ, which is from bottom to top: 0.5, 1.0, 1.5, 2.0, 3.0 and 4.0 nm. Note that the ratio between the vertical and horizontal scales is 2:1; in reality the profiles are twice as flat. The dashed lines indicate the grain boundaries at τ=4.0 nm. After the deposition of 4.0 nm, there are 7 polycrystalline grains (A-G), which grew out from 11 silicide nuclei (a-k). It is impossible to determine the precise mechanism of the merging of the grains. For example: the merging of (h) and (i) into (E) may have been accompanied by the formation of a shallow, low-energy grain boundary, or by the migration of the boundary through either (h) or (i). To the left of the graph, we cannot determine whether (b) has been overgrown by (a) and (c), and remains buried below (A) and (B), or that the grain boundaries have migrated 'outwards'. Between (F) and (G), it seems that a low-energy grain boundary has formed.

sition, but this was measured on the surface of a multilayer stack of 40 bilayers, and hence the effect should be much stronger than in our case. The change in roughness of a single layer may be too small to signify a transition. However, as we do not, at any point in the experiment, observe a dramatic change in the surface morphology of the growing film, we suggest that no amorphous-to-crystalline transition has occurred in our case. Further research is required to determine the influence of the specific production process on the occurrence or absence, and nature of the transition. A real-space investigation of the morphology of sputter deposited Mo films of varying thickness on Si substrates would yield an interesting comparison to our results.

Both the roughening and coarsening follow a power law with respectively $\beta = 0.49 \pm 0.02$ and $1/z = 0.34 \pm 0.02$ (see Equations (5.3) and (5.7))*. Using Equation (5.9) the global roughness exponent α is calculated to be 1.44 ± 0.10, and so $H \neq \alpha$: the growth of Mo on Si(111) cannot be described by self-affine scaling, which can also be inferred from the oscillatory behaviour of $C_H(r, t)$ for $r > \xi$ (see the inset in Figure 5.4). As $\alpha > 1$, the average height differences

---

*Using other definitions of $\xi(t)$ (Section 5.3), or a direct measure of the typical grain size from the STM images, results in the same value for $1/z$.
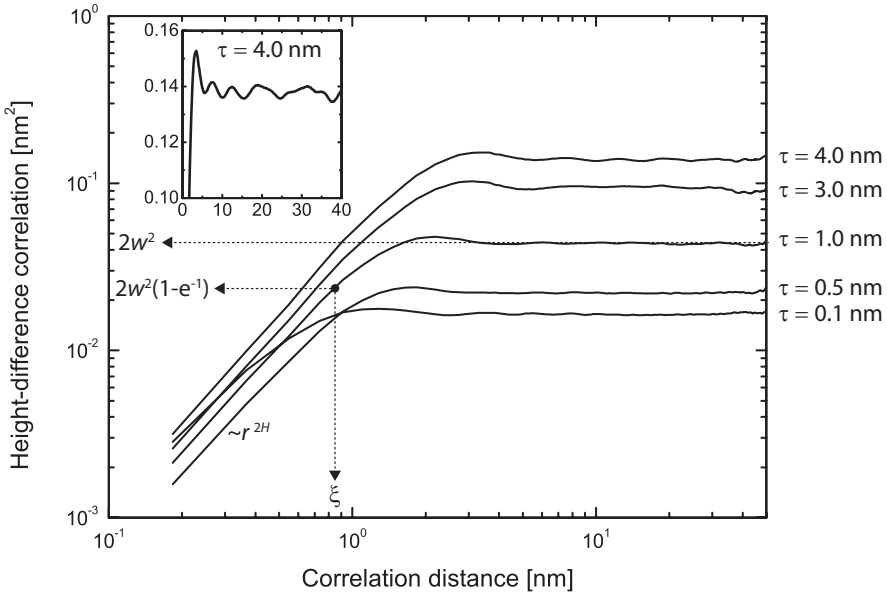
Figure 5.4: The height-difference correlation function $C_H(r, t)$ is plotted for various values of the nominal thickness τ. The inset shows a zoom-in for $\tau = 4.0$ nm. The fact that the surface is not self-affine is reflected in the pseudo-oscillatory behaviour of $C_H(r, t)$ for $r > \xi$.

outgrow the lateral feature size. This effect is known as *super-roughening* [160] and in the following we will discuss its origin.

The ES barrier induced growth instability, which is described by Equation (5.12), can lead to growth exponents $\beta = 1/2$ and $1/z = 1/3$, consistent with our observations, but not simultaneously [139]. The case in which $1/z = 1/3$ is associated with the development of a stable slope during growth, so that $\beta = 1/z = 1/3$. On the other hand, in the absence of slope selection $\beta = 1/2$, independent of z, which depends on the order n of the smoothing term in Equation (5.12) [149]. For surface diffusion related smoothing $z = 2n = 4$. In any case $z \geq 4$ and even, so $z = 3$ is not to be expected. Besides 'hunting' for the right exponents to understand the nature of the observed evolution of the surface morphology, it is worthwhile to question if an ES barrier induced instability is to be expected at all in our case. After the deposition of 3 nm Mo, the average grain radius is 2.3 nm and the height of the 'spherical' cap is $\sim$1 nm. The average terrace of a Mo grain, with $\langle 110 \rangle$ perpendicular to the substrate, is therefore a mere $\sim$2 lattice positions wide. Towards the grain boundary, i.e. towards the steepest part of the grain, atomic-sized 'terraces' must be expected.

It has been found experimentally that on small terraces of Cu(111) and Ag(111), which are less than $\sim$6 atoms wide, the ES barrier does not effectively hamper
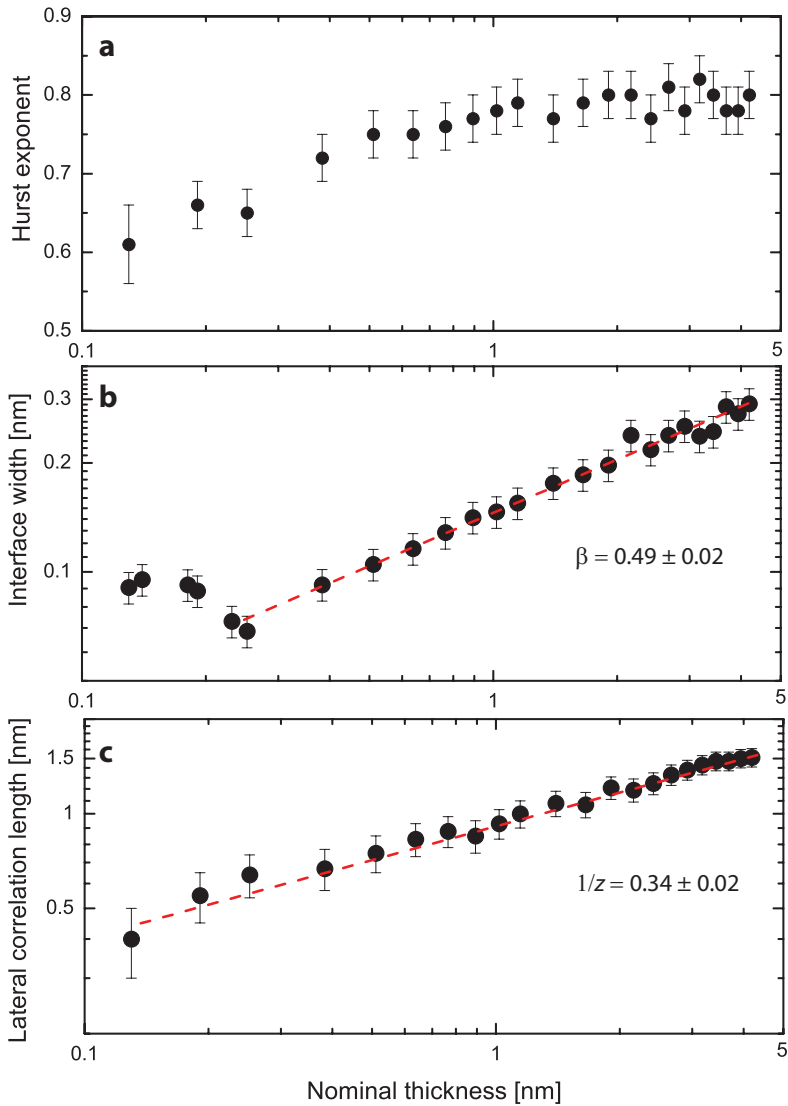
Figure 5.5: (a) During the experiment the Hurst exponent H initially slowly increases, and becomes almost constant above $\tau = 1.0$ nm. (b) The interface width $w(t)$ and (c) the lateral correlation length $\xi(t)$ are plotted versus the nominal thickness τ on a double-log graph. The dashed lines show power law fits to obtain the growth exponents β and $1/z$.

interlayer transport [161–164]. This has been related to the vanishing of the ES barrier for the case of small terraces on Cu(111) [162], which could not explain the results obtained on Ag(111) [163, 164]. There, a low-barrier, concerted diffusion mechanism was suggested to become available upon the contact of steps due to edge fluctuations, leading to very effective interlayer transport. The necessity of such a mechanism to explain the observations has been challenged [165]. At those locations where the width of the terraces vanishes atoms may diffuse on a facet. The nature of the diffusion is related to the crystallographic orientation of the facet. For example, depending on the substrate temperature, atoms deposited on fcc(111) facets during growth on a fcc(001) substrate, may not be stably adsorbed on the threefold hollow sites on the facet and diffuse downhill to a fourfold hollow site on a lower terrace. This concept, introduced by Evans *et al.* [166, 167], is known as *downhill funneling*. A process that is similar to funneling, can occur if an atom is deposited close to the edge of a fcc(111) terrace. Using the energy released in its condensation, the atom is transported, in a 'cascade' of diffusion events, to the terrace below where it is bound to the step [168]. The atomic mechanism of this effect may include that an atom at the edge of a terrace is 'pushed out' of the step onto the lower terrace, while the adatom takes its place [169–171].

The effects described in the previous paragraph, which cause a downhill diffusion current that can be especially very effective in the case of downhill funneling, become increasingly dominant in the evolution of the morphology when the width of the terraces reduces. Therefore, we expect one or more of these effects to play a role in our case. The downhill diffusion currents cancel the effects of an uphill current, if present at all in our case, that would lead to mounding*. Therefore, we do not expect the ES barrier effect to dominate the growth in our case. Also the growth instabilities that are caused by step-adatom attraction and step-edge diffusion (Section 5.4.2), can be active in our experiment. However, also these effects are expected to be of little influence for the case of narrow, and even vanishing, terraces.

Another effect that can be expected to be of influence on the film growth, is caused by the energy barrier that must be overcome if an atom diffuses from one grain to another: the grain boundary crossing (GBC) barrier. The height of the GBC barrier is expected to depend on the relative orientation of the grains [172, 173]. A diffusion barrier can be evaluated using *transition state theory*: during the diffusion from one adsorption site to another, an atom goes through a transition state with a higher potential energy. The height of the barrier is equal to the difference in energy between that of the initial situation and of the transition state. Low-energy grain boundaries, such as those between *twin* crystallites, should have a small GBC barrier, whereas high-energy grain boundaries, resulting from a significant misorientation[†] between the grains are

---

*A net downhill diffusion does not cause a growth instability.

[†]There are a few 'special' grain boundaries that have a low-energy, although the degree of misorientation is large [174, 175].

expected to have a large GBC barrier.

Based on the WV and DT SOS models (Section 5.4), Albano *et al.* considered a model, with which the effect of both an ES barrier and a GBC barrier on polycrystalline film growth was studied [176]. The explicit inclusion of the effect of grain boundaries on thin film growth in this model justifies that we shall refer to it as the polycrystalline solid-on-solid (PSOS) model. In the PSOS model both the ES and GBC barriers were included by introducing a probability of the crossing of either barrier. From the simulated films, the growth exponents β and $1/z$ were extracted in a similar way as was done in our analysis. The case where an ES barrier is absent, and full interlayer transport is possible, but mass transport from one grain to another is forbidden due to an impassable GBC barrier was found to result in $\beta = 0.52 \pm 0.07$ and $1/z = 0.33 \pm 0.03$, which nicely matches our results. Also in our case the absence of an effective ES barrier is to be expected, but for the GBC barrier the situation is more complicated as we expect low *and* high barrier heights, depending on the specific type of boundary. Here we must consider that low-energy grain boundaries, which are expected to have a low GBC barrier, have a minor effect on the roughness and the lateral correlation length: two grains that are separated by a low-energy boundary, might seem to be a single grain. On the other hand, the high-energy grain boundaries that dominate the surface morphology, and its characterization using lateral correlation functions, *are* expected to have a large GBC barrier. Due to this large barrier, smoothing by diffusion is limited and because of the deposition noise, height differences between grains add to the roughness. The analogy between the PSOS model and our results can be extended somewhat further, as we will see in the following.

Although a self-affine scaling theory cannot be used to characterize the evolution of the film morphology for Mo deposition onto Si(111), the fact that both $w(t)$ and $\xi(t)$ do scale independently with τ enables the characterization through an anomalous scaling theory [160, 177–179]. For self-affine growth, $C_H(r,t)$ is constant in time for $r \ll \xi$, whereas in the case of anomalous scaling $C_H(r,t)$ for $r \ll \xi$ increases as $C_H(r,t) \propto t^{\beta_L}$, in which the exponent is given by [179]:

$$\beta_L = \frac{\alpha - H}{z}, \qquad (5.13)$$

from which we expect β_L to be ~0.22 in our case. From a direct determination of the evolution $C_H(r,t)$ for $r \ll \xi$ we find that $\beta_L = 0.18 \pm 0.04$. Albano *et al.* found a value of 0.17 ± 0.05 for the local roughening exponent β_L from their PSOS simulations [176], which is again in agreement with our results.

There is an important point to be made regarding the comparison between the PSOS model and our experiment. Naturally, the effect of a GBC barrier on the morphology can only be active if grain boundaries are actually present. In our case one does not expect grain boundaries to be present at all the circumferences of the grains at thicknesses below ~2.5 nm, which represents the thickness at which the film closes. In the beginning of the growth, most of the nuclei are separated and no grain boundaries are formed. Nevertheless, we find that the

growth exponents correctly describe the development after already $\tau = 0.25$ nm. In part, this can be understood from the fact that already after $\tau = 0.1$ nm we observe the merging of grains, which must be accompanied by the formation of grain boundaries. However, in analogy to the GBC barrier, it is not clear that the transport of material between still separated nuclei is accompanied by a large energy barrier for diffusion, although we may expect that the diffusion of Mo atoms is limited at room temperature. Even if the transport between nuclei is very limited, it not clear if that would lead to the same growth exponents before and after the closure of the film. The fact though, that we do not observe a change of the growth exponents for the whole thickness range is indicative of the fact that globally the growth must be very similar before and after closure.

Even though the PSOS model aids in the understanding of the observed growth, a direct understanding of the origin of the growth exponents is still lacking. The fact that both β and $1/z$ are close to simple rational numbers may prove to be indicative of their fundamental origin. Coarsening, or grain growth, has been found to occur during deposition or annealing of thin films [14, 180]. The driving force generally considered, is a reduction of the free energy by a decrease of the total grain boundary energy, i.e. by a reduction of the number of grains. This mechanism should lead to a coarsening exponent $1/z = 1/2$, in the case of spherical grains [181], although it has since long been recognized that experimentally determined values of $1/z$ range between $1/4$ and $1/2$ [182, 183]. A theoretical model of the type of growth we observed in our experiment should include an atomistic description of the interface curvature driven grain growth [183], including the effect of GBC barriers, but also the following must be considered to have an influence on the growth. Surface diffusion depends on the specific crystallographic orientation of a grain, and so it may be that at a certain grain boundary atoms are incorporated at a higher rate from one side than from the other, which can lead to the overgrowth of one of the grains. Another effect that can occur during polycrystalline film growth is the following. Although having an effective high GBC barrier, a particular grain boundary may have locally a low GBC barrier where atoms can cross the grain boundary, but stay in the close vicinity. An effective high GBC barrier is realized if the atoms are more strongly bound at a location close to the grain boundary as compared to a location further from the boundary, like on the terraces of the grains. The case of an asymmetric local GBC barrier can lead to the preferential growth of some grains and the overgrowth of others.

5.5.3 Deposition onto ion eroded Si(111)

In the fabrication of Mo-Si multilayer optics the Mo layers are not deposited onto single-crystalline Si wafers, but onto deposited Si, which is in an amorphous state. In Chapter 4 we found a rather dominant effect of the Si(111) 7×7 superstructure on the nucleation density, as was derived from the anisotropy

of the autocorrelation function $C_A(\mathbf{r}, t)$ in Figure 4.4. In later stages during deposition $C_A(\mathbf{r}, t)$ becomes isotropic and the effect of preferential nucleation is overgrown. Nevertheless, to infer if the obtained growth exponents β and $1/z$ are universal for growth of a Mo film on Si, an additional experiment was performed using a Si substrate, of which the surface was amorphized using ion erosion. After flash annealing of a Si(111) sample it was bombarded with 800 eV Ar$^+$ ions with a total dose of 5 ions nm^{-2} to remove the 7×7 periodicity*. The deposition conditions and substrate temperature were chosen to be the same as during the experiment on Si(111)-7×7; also this experiment was obtained in a real-time fashion.

Figure 5.6 shows STM images taken during deposition of Mo onto this sample. The roughening and coarsening behaviour were obtained from $C_H(r, t)$; the Hurst exponent H above $\tau = 1.0$ nm was found to be 0.75 ± 0.04. The evolution of $w(t)$ and $\xi(t)$ is plotted in Figure 5.7. In Table 5.1 the parameters that characterize the evolution of the surface morphology of both deposition experiments are summarized.

Substrate	Si(111)-7×7	Ion eroded Si(111)
β	0.49 ± 0.02	0.47 ± 0.04
$1/z$	0.34 ± 0.02	0.31 ± 0.04
α	1.44 ± 0.10	1.52 ± 0.23
$H(\tau > 1.0$ nm$)$	0.79 ± 0.04	0.75 ± 0.04
$w(\tau = 3.0$ nm$)$	0.24 ± 0.02 nm	0.25 ± 0.02 nm
$\xi(\tau = 3.0$ nm$)$	1.4 ± 0.1 nm	2.0 ± 0.1 nm

Table 5.1: Summary of the morphological parameters that characterize the growth of Mo on Si(111)-7×7 and on ion eroded Si(111).

For the growth of the Mo film on the partially amorphized Si substrate we find the same power law behaviour, for both the roughening and the coarsening, as on the Si(111)-7×7 substrate, and so we can expect that similar processes govern the evolution of the surface morphology on either substrate. We speculate that also on truly amorphous Si substrates, such as those in Mo-Si multilayer systems, the growth mode of the Mo layers, if deposited by e-beam evaporation, is very similar.

The main difference between the two experiments is found in the initial stages of deposition. The lateral length scale in the case of the eroded sample is dominated by the damage introduced by the ion erosion. After the closure of the film, around $\tau = 3.0$ nm, ξ is significantly larger, which implies a larger typical grain size. This indicates a difference in nucleation density between both experiments; the lower density corresponding to the eroded Si sample. Unfortunately, the absence of atomic-scale resolution on the eroded Si substrate, as well as its intrinsic

---

*The dose was kept low to maintain a reasonably flat surface.

$\tau = 0$ nm $\Delta h = 0.5$ nm $\tau = 0.6$ nm $\Delta h = 0.5$ nm $\tau = 3.0$ nm $\Delta h = 1.4$ nm
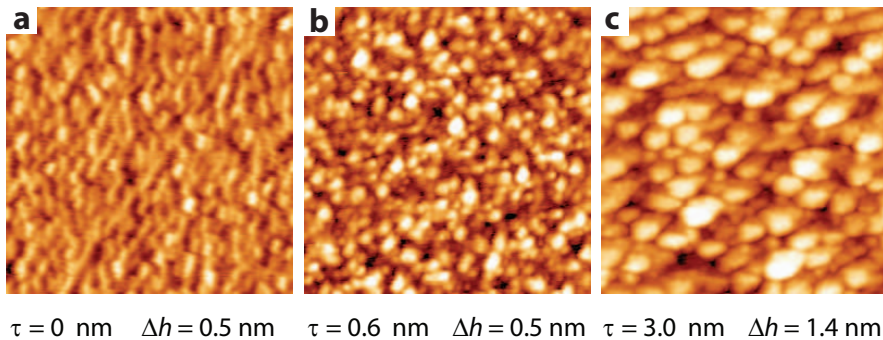
Figure 5.6: (a-c) STM images ($50 \times 50 \times \Delta h$ nm^3) of Mo deposited onto a Si substrate that partially amorphized by bombarding it with Ar$^+$ ions. The nominal thickness τ is indicated. Note that Δh is different for (c).
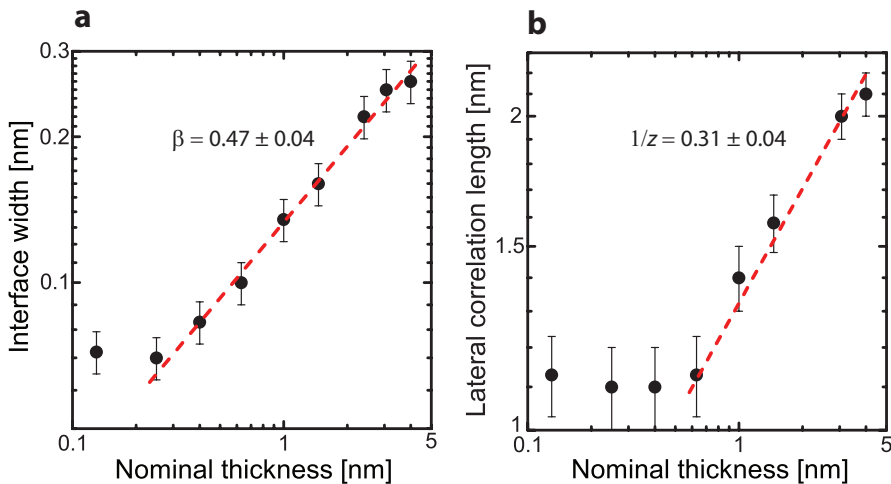
Figure 5.7: Graphs showing the roughening and coarsening of a Mo film during its deposition onto the ion eroded Si substrate. (a) The interface width $w(t)$ and (b) the lateral correlation length $\xi(t)$ are plotted versus the nominal thickness τ on a double-log scale. The dashed lines show power law fits to obtain the growth exponents β and $1/z$.

roughness and coarseness, make it impossible to analyse the initial stages of the Mo deposition onto this substrate in the same detail as was done for the crystalline Si substrate in Chapter 4. A difference in nucleation density should not only have an effect on the size of the crystallites of the full Mo layer, and therefore on the roughness [14][*], it should also play an important role in the closure of the film and hence in the thickness of the Mo-silicide interlayer.

5.6   From fundamental research to application

Not only the type of substrate, but also the deposition rate, which is significantly higher in the production process of Mo-Si multilayer optics as compared to our experiment, is expected to be of influence in the nucleation stage and the further growth. On defect-free, single-crystalline surfaces the nucleation density N should scale according to [139]:

$$N \propto (F/D)^{\chi}, \tag{5.14}$$

in which F is the deposition rate and D is the surface diffusion coefficient, which is proportional to ν in Equation (4.1): D increases with increasing substrate temperature. The exponent χ depends on the size of the smallest stable cluster. An increase in nucleation density can thus be achieved by increasing the deposition rate, by decreasing the substrate temperature, or both. We do not expect this model to describe the nucleation stage of Mo growth on Si, for two reasons. Firstly, the surfaces are not free from defects: the 7×7 superstructure on the Si(111) was found to dominate the nucleation density and in the case of the eroded Si the in-plane length scale introduced by the ion erosion seemed to be of influence on the nucleation density. On an amorphous Si substrate the density and nature of defects should be of influence on the nucleation density. Secondly, we have seen in the previous chapter that the substrate atoms participate in the nucleation of silicide clusters, a process which itself introduces defects. Nevertheless, it may be expected that the nucleation density depends on the deposition flux and the substrate temperature.

Mo-Si multilayer optics are most commonly produced at room temperature, similar to our case, but the difference in growth rate of up to three orders of magnitude can be expected to result in a large difference between the Mo layers in industrially applied Mo-Si multilayer systems and the Mo films we have studied. To further bridge the gap between the growth of Mo under model and industrial conditions, a comparison has been made between our results and recent STM measurements of Mo films deposited in a professional coating facility for the fabrication of multilayer optics [184]. Mo films produced there are deposited on amorphous Si layers at a growth rate of ~ 0.1 nm s^{-1} (compare with our growth

---

[*]In our case we do not find any effect on the evolution of the roughness, which is almost identical for both experiments; cf. β and $w(\tau = 3.0$ nm$)$ for either experiment, see Table 5.1.

rate of 1.3×10^{-4} nm s^{-1}). Preliminary results point towards the growth of Mo crystallites with sizes comparable to those in our model experiments. In the case of the deposition under industrial conditions, the Mo grains are ∼4 nm in diameter at $\tau = 3$ nm. At that film thickness, the film deposited in the professional coating setup exhibits an interface width of 0.22 nm, which is equal, within the error margins, to $w(\tau = 3$ nm$)= 0.24$ nm obtained in our experiments. The fact that the growth is similar, signifies the dominance of the chemical interaction of Mo and Si on the growth. We expect that the influence of the substrate temperature on the process is much larger than that of the deposition rate, as it not only alters the nucleation density directly, but also has an effect on the silicide formation.

5.7 Conclusions and outlook

Mo deposition onto Si(111)-7×7 by e-beam evaporation leads to the development of a polycrystalline film, which is observed to be more or less completely closed after the deposition of 2.5 ± 0.5 nm Mo. At the relevant thickness for Mo-Si multilayer optics of 3 nm, the grains have an average diameter of 4.5 nm[*] and the interface width is 0.24 nm. During the deposition of the Mo film, the height-variations grow faster than the in-plane grain size: the film develops a super-rough morphology. The origin of this super-roughness is very likely an impassable grain boundary crossing barrier: atoms cannot diffuse to an adjacent grain if a high-energy grain boundary needs to be crossed. Diffusion is allowed to increase the coordination number of a deposited atom and to lower the free energy. The diffusion is not hampered by an Ehrlich-Schwoebel barrier, as effects that lead to downhill diffusion are expected to be active. To explore the relevance of our findings for Mo-Si multilayer optics, we have also investigated the growth on a Si substrate that was altered by ion bombardment prior to deposition to destroy the surface crystallinity, as in the case of the industrial process Mo is deposited onto amorphous Si. A very similar type of growth was found, but the nucleation stage was different for the ion eroded substrate, which had a modest effect on the morphology of the closed film.

Evidently, the super-rough growth of Mo on Si is not favourable for Mo-Si multilayers, in which the performance relies on the smoothness of the interfaces. Having related this super-roughening to a large grain boundary crossing barrier, impassable at room temperature, the relevant question is whether the situation can be improved. Is a smoother morphology of the Mo layer possible? Again, we refer to Ref. 176, in which also simulations of polycrystalline film growth are reported that do include a finite probability that an atom diffuses to a neighbouring grain. If the chance that an atom attempting to cross-over to an adjacent grain

---

[*]Note that if two grains are separated by a low-energy grain boundary, they can be falsely interpreted as being a single grain. This has an influence on the determination of the average grain size.

succeeds, is only 0.1, the roughening exponent β is already reduced by 30%. In the limit of a vanishing GBC barrier, smoothing can occur by unbounded transport between grains, and $\beta \approx 0.25$ [176]. If this situation could be realized in our case, the film roughness at a thickness of 3 nm would be significantly reduced. If $w(t)$ would evolve as $t^{0.25}$, instead of as $t^{0.5}$ after $\tau = 0.25$ nm, the interface width at $\tau = 3$ nm would decrease from 0.24 nm to 0.14 nm.

The obvious way to increase the probability for diffusion across grain boundaries is to increase the substrate temperature during deposition. The major drawback of this approach is that it would lead to additional intermixing of the Mo and Si layers leading to an increase of the thickness of the silicide layers [185]. It would be better to heat only the growth front during deposition. A technique that naturally exhibits this feature is sputter deposition, in which the deposit arrives in the form of energetic ions and neutrals. Interestingly, already in the 1980s it was suspected that the multilayers produced by sputter deposition had probably smoother interfaces than those produced by e-beam evaporation [186]. The downside of sputter deposition is that it can lead to an increased intermixing due to the impact of highly-energetic particles on the substrate. Ion beam assisted deposition (IBAD), which is the simultaneous ion bombardment of a growing film during deposition, is a way to introduce additional energy in the top surface layers during deposition by evaporation. Mo-Si multilayer optics have been produced by IBAD, see e.g. Ref. 187, in which the reflectance of the optics was reported to be 65%. Here we stress that when using IBAD to produce Mo-Si multilayers, the ion beam should be turned on only after the deposition of a significant amount of Mo to avoid additional intermixing*. This *modus operandi* should give an advantage over sputter deposition, in which it is not possible to turn on and off the energy addition at will. Yet another approach is to alter the morphology of the Mo film *after* its production. In Chapter 7 we investigate the possibility of post-deposition smoothing of Mo thin films by means of ion bombardment.

Finally, an important point must be made regarding cross-sectional TEM images of multilayer structures. The morphology of the Mo film in Figure 5.1 should be kept in mind when (re)viewing these TEM images. A sample prepared for TEM has a typical thickness between 10 nm and 200 nm [188]. TEM images are thus the result of an averaging over possibly many Mo crystallites. Consequently, the roughness observed in these TEM images is an underestimate of the actual roughness. In addition, due to the averaging, interface roughness may be falsely interpreted as interlayer formation, and the thickness of the interlayer can be overestimated. Hence, the thinnest samples should yield the most accurate picture, but these samples are altered the most, in a relative sense, by the sample preparation process. Although cross-sectional TEM images are useful to inspect multilayer structures, care must be taken in their interpretation.

---

*The moment the ion beam should be turned on depends on the penetration depth of the ions, hence on the ion energy, the type of ions, and the angle of incidence of the ion beam.

Ion erosion of Si(111)-7×7

The eroding effect of low-energy ion bombardment was investigated on a single-ion-impact level, with atomic-scale resolution. A Si(111)-7×7 substrate subjected to a flux of Ar^+ ions, was imaged with STM during the ion sputtering process. The resulting movie allows us to perform a detailed analysis of the efficiency and spatial correlations of the local sputtering. The evolution of the spatial damage distribution indicates preferential sputtering of damaged regions and reflection of ions on the undamaged Si. An additional effect on the surface structure is the ion induced creation of Si adatoms, which subsequently diffuse and cluster on the substrate. The combined effect of the sputtering process is the development of nanometer-sized grooves and ridges, which are oriented parallel to the projected ion beam direction.

6.1   Introduction

In surface science and technology sputtering, the removal of atoms and molecules from a substrate by bombarding it with energetic ions, is an important means of surface modification. It is employed e.g., as a sample preparation step for single-crystal model experiments, in ion beam assisted deposition (IBAD) of thin films, and for smoothing of surfaces [189]. The latter application is important for the optimization of the reflectivity of multilayer mirrors and for thin film engineering in general. A study of the effects of ion bombardment on the morphology of thin Mo films is the subject of Chapter 7 of this thesis.

The central question addressed in the numerous experiments on ion bombardment concerns the sputtering yield, i.e. the amount of material removed relative to the ion dose. These investigations range from simply determining the decrease in mass of a sputtered sample with a quartz crystal balance [190], to more detailed studies probing the evolution of the surface morphology with, e.g., X-ray scattering, thermal He scattering and Raman spectroscopy [191–193].

The introduction of the STM enabled the study of the sputtering process on the atomic scale and the possibility of observing local effects. One of the difficulties in applying STM, a technique that displays its full power on atomically flat surfaces, lies in the fact that ion erosion is often accompanied with surface roughening. The combination of sputtering and thermal annealing - to retain a suitable sample for STM - can yield detailed, yet indirect information on the sputtering process, provided that the annealing process is sufficiently well understood. This approach proved to be very effective in investigating ion erosion of Pt(111) [194]. As with deposition experiments, STM has mainly been employed to probe the surface morphology *after* bombardment. With our new STM it is possible to investigate the details of sputtering on the atomic scale, in a real-time fashion.

Of special interest are ion induced patterns, such as ripples and dots [195, 196]. This *nanostructuring* of surfaces is understood to be the consequence of a balance between non-uniform sputtering and diffusion [197, 198]. In fact, the ion eroded surface presented in Section 5.5.3 had an anisotropic morphology, as can be seen in Figure 6.1, which shows the same surface as in Figure 5.6(a), on a somewhat larger scale. The colour scale has been adjusted to clearly display the pattern. From the autocorrelation function we find an average wavelength of the pattern of 4.2 nm. To investigate the origin of this pattern and to study the interaction between the ions and the substrate on the atomic level, we bombarded a Si(111)-7×7 surface with a relatively low Ar^+ flux to record single impact damage, while the surface remains flat enough for STM imaging with atomic resolution. The experiment offers a unique perspective on ion erosion, with direct observations of the local sputtering yield and its dependence on the surface morphology. In addition, we observe surface diffusion and clustering of material that is displaced by the impact but not removed from the surface.
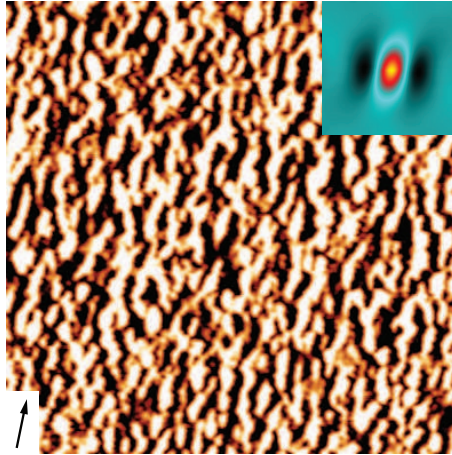
Figure 6.1: STM image ($70 \times 70 \times 0.15$ nm^3) of Si(111) eroded by grazing incidence ion bombardment (dose: 5 ions nm^{-2}). The inset shows the autocorrelation function of the image (window size is 10×10 nm^2). The arrow indicates the azimuthal direction of the ion beam. The grooves and ridges are oriented parallel to this direction.

6.2 Experiment

6.2.1 Details

The Si(111) sample was cleaned by flash annealing to 1450 K; the usual 7×7 reconstruction was observed with STM [80, 105–109]. During the experiment the sample was at room temperature. The ion source was used to generate 800 eV Ar$^+$ ions. The polar angle of incidence of the ions was $75°$ from the surface normal. The base pressure of the UHV chamber was below 5×10^{-11} mbar; during the experiment the pressure in the UHV chamber rose to 3×10^{-9} mbar. The average ion flux during the experiment* was 3×10^{14} m^{-2} s^{-1}. A 25×25 nm^2 region was imaged with the STM, at a sample voltage of $+2$ V and a tunneling current of 200 pA. The ion current on the tip was much smaller than the noise of the *IV*-converter, and hence was of no influence on the imaging. The recording time was 10.9 s per image, which means that on average 2 ions arrived at the investigated region per frame. A total of 416 images were recorded, which capture the erosion of the surface from an ion dose of 0 to 1.26 nm^{-2}.

---

*The ion flux was estimated from the current density on the sample cup, see Figure 2.3, not taking into account the effect of the generation of secondary electrons on the measured ion current.

6.2.2   Results and discussion

Figure 6.2 shows frames from the resulting STM movie. The complete movie is available as supplementary material [199], also in a '3D', projected version that offers a different perspective; some selected 3D STM images are shown in Figure 6.3. Because of the constant image quality, we were able to subtract from every frame the preceding frame, and from these *difference images* we could pinpoint accurately the changes from frame to frame. The STM recording shows that the structure of the substrate is modified in several ways, predominantly by the removal of material: the formation of holes. The lateral size of these holes ranges from that of a single vacancy to the equivalent of half the 7×7 unit cell. In general these larger vacancy islands appear to be deeper, but it is difficult to quantify the depth due to the influence of the tip convolution on the topography. So, to investigate the sputtering efficiency, rather than speculating about the precise amount of material removed, we distilled from the difference images the number of removal events and their coordinates. In this way we obtained the evolution of the spatial damage distribution. Note that the surface already exhibited some defects prior to the bombardment. The number and location of these damage sites were also taken into account in the analysis; see Figure 6.4.

Figure 6.5 shows the cumulative number of removal events plotted against the ion dose. As the surface becomes more damaged, the damage a single ion does, increases. The exponential dependency shows that the instantaneous removal rate scales linearly with the amount of damage done up to that point in the experiment. From this we conclude that the perfect Si(111)-7×7 surface is reflective for 800 eV Ar^+ ions incident at 75° from the surface normal, or equivalently, that the ions reflect off the undamaged regions. From low-energy ion scattering (LEIS) it is understood that the interaction of the ions and the substrate can be viewed as two-body collisions between the ions and the substrate atoms, governed by the Coulomb repulsion between the nuclei and the distance dependent screening of the electrons [200]. An incident ion can be backscattered by a series of these binary collisions, depending on its energy and angle of incidence. We suggest that this is the mechanism through which the ions are reflected on the undamaged Si. The effect of one or multiple missing surface atoms is that on these locations the ions do not interact sufficiently with the substrate to be reflected, which results in an impact in the proximity of the damaged site and subsequent sputtering of material. A similar mechanism was proposed for the preferential sputtering of step edges as observed on Pt(111) [201].

The effect of the condition of the surface on the sputtering efficiency found in our experiment would lead to a non-uniform removal of material. A qualitative inspection of the movie also hints towards a preferential sputtering of damaged areas: while some regions become heavily damaged, on other locations the surface remains undamaged. We assume that the ions arrive at the surface randomly, so that if the state of the surface has no influence on the sputtering efficiency, the
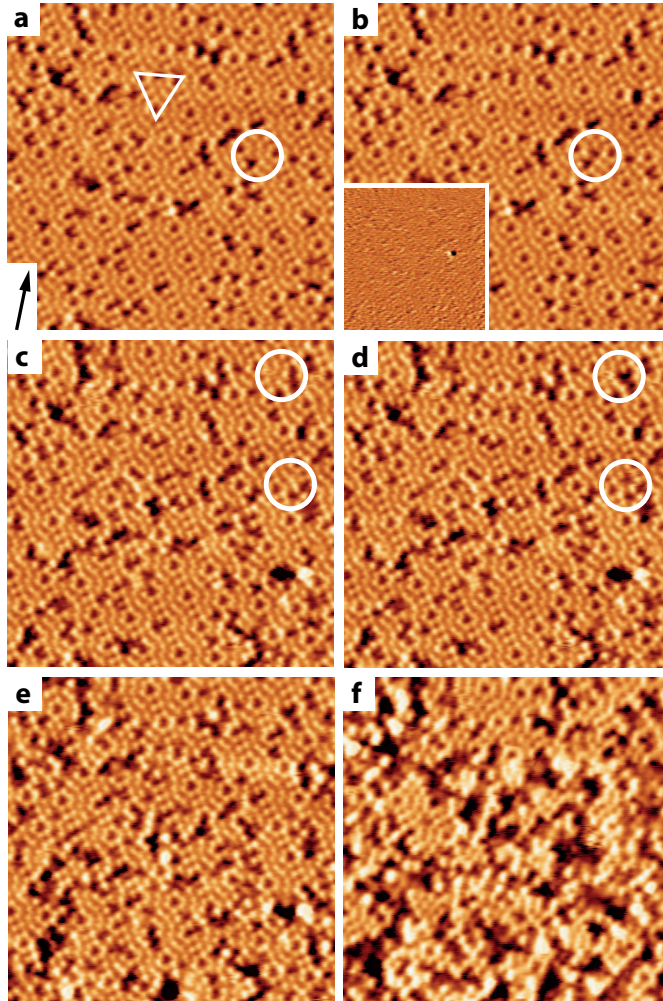
Figure 6.2: Frames ($25\times25\times0.20$ nm^3) from an STM movie recorded during Ar$^+$ ion bombardment of a Si(111)-7$\times$7 surface [199]. Frames (a), (c), (e) and (f) show the erosion of the surface at different ion doses: 0.015, 0.28, 0.69 and 1.2 nm^{-2} respectively. The arrow in (a) indicates the azimuthal direction of the ions; the triangle does not indicate a special location but is used for further reference. To analyse the effect of the ions on the surface morphology on a single-impact level, from every frame the preceding frame was subtracted. Frames (b) and (d) were recorded directly after respectively (a) and (c). The inset in (b) shows an example of a difference image used in the analysis: the result of (b)$-$(a). The circles indicate the positions where the surface changed between the frames.
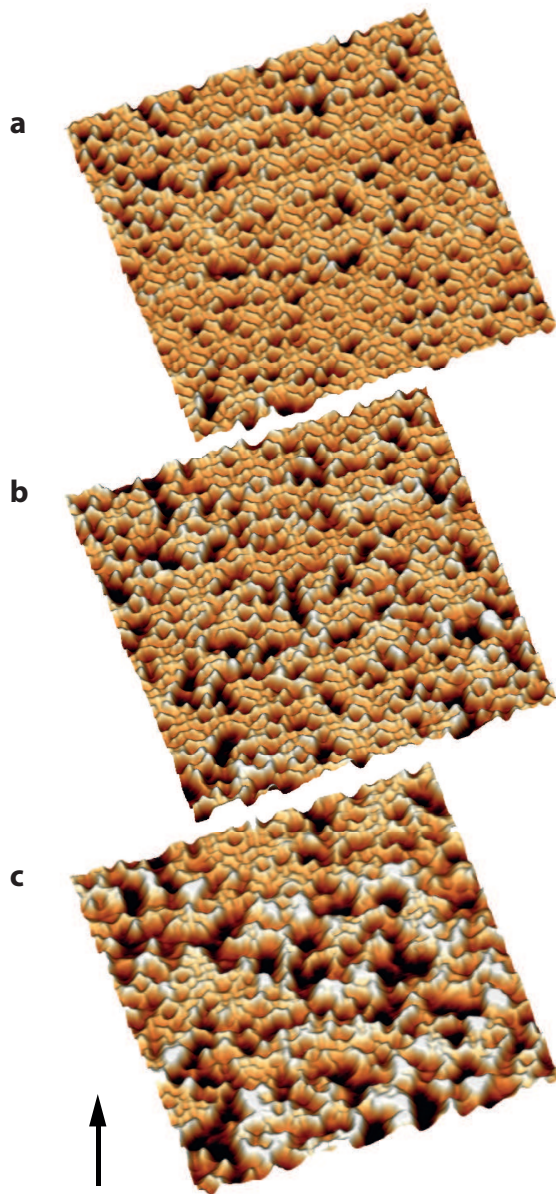
Figure 6.3: STM images (25×25 nm$\times 0.20$ nm^3) recorded during Ar$^+$ ion bombardment of a Si(111)-7×7 surface [199]. Images (a-c) show the state of the surface after an ion dose of respectively 0, 0.55 and 1.1 nm^{-2}. The arrow indicates the azimuthal direction of the ions.
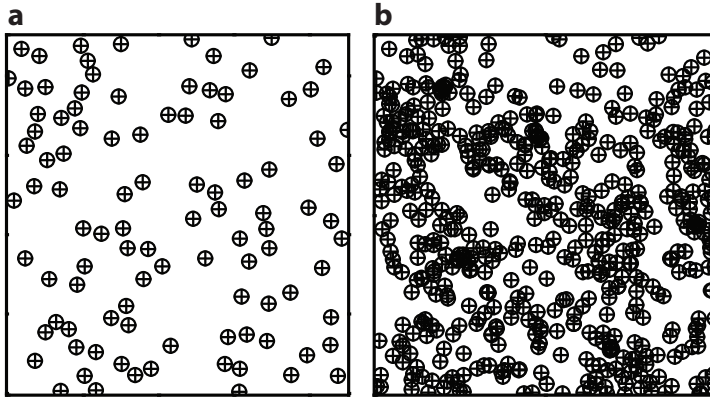
Figure 6.4: Spatial distributions (25×25 nm^2) of (a) the initial and (b) the final distribution of damage sites. The total 416 spatial distributions capture the evolution of the distribution of the damage.
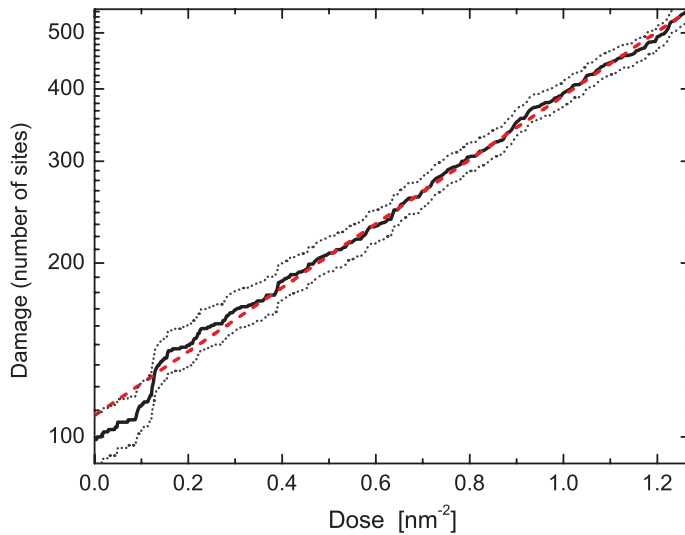
Figure 6.5: The number of removal events is plotted against the ion dose. The vertical axis is logarithmic, hence the dashed line is an exponential function fit of the data. This dependency implies that the Ar$^+$ ions reflect off the undamaged Si. The dotted lines indicate the error margins.

Figure 6.6: The ratio of the variance (σ^2) and the mean (μ) of the distribution of the number of removal events in a certain sample area, determined for various sample sizes, is plotted versus the number of removal events. A random distribution of removal events would lead to $\sigma^2/\mu = 1$. In the case of the present study the ratio evolves to $\sigma^2/\mu > 1$, a clustered type of distribution: it is more likely for a new hole to be created in the proximity of an already damaged site, than at a random location.

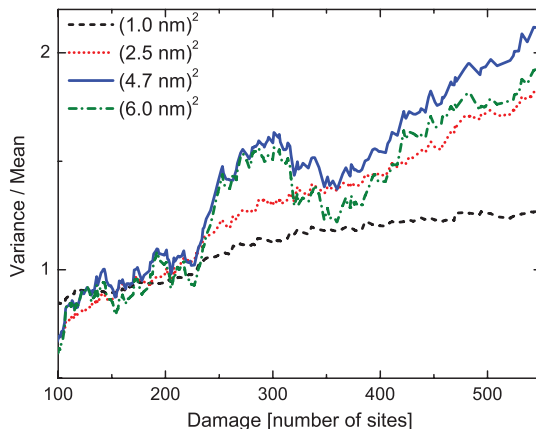removal events would be distributed Poissonian. To analyse this, we evaluated the evolution of the spatial damage distribution in terms of the mean (μ) and the variance (σ^2) of the density of removal events. This analysis was carried out by sampling square sub-regions in the spatial distributions (see Figure 6.4) and counting the number of removal events in each square. For a random distribution the ratio σ^2/μ equals 1. Figure 6.6 shows that the damage distribution evolves to a clustered type with $\sigma^2/\mu > 1$, which proves preferential sputtering of damaged regions. The analysis was performed for different sample sizes. The effect of clustering is largest viewed on a 4.7×4.7 nm^2 scale. As the typical distance of a new hole to the nearest previously damaged site is 0.7 $\pm$ 0.4 nm, the typical size of the aggregation (4.7×4.7 nm^2) is the result of an 'inkblot' type of spread.

During the bombardment the morphology of the surface is also changed by the accumulation of material on the substrate. We attribute this to ion induced displacement and subsequent ejection of atoms onto the surface. A similar effect has been shown on Pt(111) [202]. We stress that it is highly unlikely that the added material is sputtered Si that is redeposited. For this to occur, an ejected atom must collide with part of the substrate, which is improbable on an atomically flat surface. The combination of removal of material and the formation of clusters on the substrate leads to an overall increase of roughness.

A closer investigation of the movie reveals that near a recent impact one can often observe a well-defined region with noisy scan lines. We attribute the origin of this 'glimmering' to atoms diffusing too fast for the STM to fully capture them, see
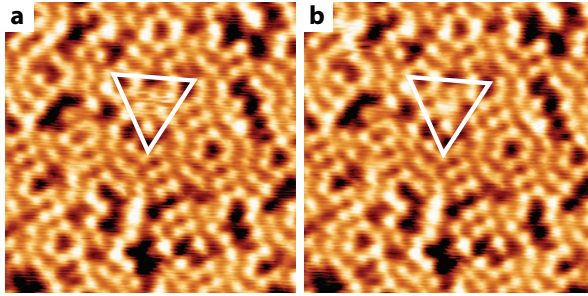
Figure 6.7: STM images (12×12 nm^2 cut outs) taken from the movie [199]; the triangles correspond to the one in Figure 6.2(a). (a) Surface diffusion of an extra-adatom is visible as 'noise' in the STM scan lines: the diffusion is too fast for the STM to fully capture the varying location of the extra-adatom. This atom was ejected onto the surface by an earlier ion impact. The extra-adatom is bound to half of the 7×7 unit cell, indicated by the triangle, as the energy barrier to diffuse to the next half unit cell is too high to overcome at room temperature. (b) The diffusion is terminated by another impact at the right side of the triangle, the ejection of more material and subsequent clustering. This event occurs 20 s after the start of the movie.

Figure 6.7(a) for an example. The diffusing atoms were ejected onto the surface by the impinging ions, but did not form a stable cluster. The fact that the diffusion is localized, implies that these *extra-adatoms*[*] are bound to a certain area. With density functional theory (DFT) calculations and atom-tracking STM the energy barrier for diffusion E_b of an extra-adatom from one half of the 7×7 unit cell to the next was determined to be 1.12-1.14 eV [203, 204]. The rate ν at which that happens can be calculated using Equation (4.1). Thus, at room temperature such an event is extremely rare, occurring once every 4×10^6 s, assuming an attempt frequency for diffusion ν_0 of 10^{13} Hz: the extra-adatom is trapped in the half unit cell. The energy barrier for diffusion within a half unit cell was calculated to be 0.56 eV [203], which means that an extra-adatom is expected to change its position every 0.5 ms. On the same time scale the STM tip traverses the half unit cell each scan line. As the time between the scan lines is 20 ms, the observed noise pattern is precisely what one would expect: within one scan line distinct recordings of the diffusing atoms, but no correlation between the lines[†]. The diffusion of extra-adatoms is terminated locally with either the sputtering of the *active* region as a whole, or the further ejection of atoms as the result of a new impact and the subsequent clustering of added Si, see Figure 6.7(b).

---

[*]It is customary to refer to an added atom on the Si(111)-7×7 as extra-adatom, to avoid confusion with the adatoms that are part of the surface reconstruction.

[†]The temporal resolution of our technique is in between two regimes. If the imaging were faster or the diffusion slower, we would be able to capture the precise position of the atoms. Faster diffusion, or slower imaging would lead to an average contribution to the tunneling current on the entire area, which would then appear to be higher.
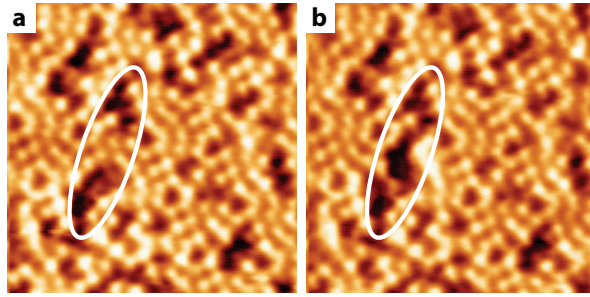
Figure 6.8: STM images (12×12 nm² cut outs, from the lower left part) taken from two consecutive frames at a dose of 0.63 nm⁻². At the indicated position a trench is formed from two smaller ones by the sputtering of the atoms that formed the boundary.

6.3   Pattern formation

At the end of the experiment (Figure 6.2(f)), the surface does not exhibit a clear pattern. Instead, trenches are visible, oriented in the projected direction of the ion beam, are visible. We suggest that these trenches evolve into the grooves that are observed in Figure 6.1 for a dose that is a factor ∼5 higher than that in Figure 6.2(f). The lensing effect of the damaged regions, discussed in the previous section, implies a preferential sputtering of the 'far end' (as viewed from the ion source) of such a region. In the later stages of the movie it can be observed frequently that a crater grows as a result of this effect. As an example Figure 6.8 shows the growth of a trench from two smaller ones. Although the described preferential sputtering can be readily seen to lead to an anisotropic surface morphology, namely grooves, it does not directly dictate a specific wavelength. Before addressing that issue, it is interesting to compare our results with established models on pattern formation.

6.3.1   Comparison to the Bradley-Harper model

The continuum model that forms the basis for the description of ripple formation by ion bombardment is known as the Bradley-Harper (BH) model [205]. References 197 and 198 provide a mathematical description of the theory and an overview of the different sputtering phenomena that have been explained by the BH-model and derivatives thereof. The main features of the model are summarized here. The BH-model is based on Sigmund's theory of sputtering [206, 207]: when an ion strikes a surface, it penetrates the solid and loses its energy by colliding with the target atoms, of which some are sputtered or displaced in the process. The initial kinetic energy of the ion, E_0, is distributed in the near-surface region,

following a Gaussian:

$$E(x, y, z) = \frac{E_0}{(2\pi)^{3/2}\kappa\rho^2} \exp\left(-\left(\frac{(z'-a)^2}{2\kappa^2} + \frac{(x'^2 + y'^2)}{2\rho^2}\right)\right),$$ (6.1)

where a is the average penetration distance and κ and ρ are the longitudinal and lateral spread of the distribution*. Bradley and Harper showed that the local sputter yield, related to the distribution of energy of all incoming ions, depends on the surface curvature: concave regions (valleys) are sputtered faster than convex areas (hills), which causes roughening. In the basic BH-model, surface relaxation enters the model via classical diffusion [141, 142]. The equation that governs the evolution of the local height $h = h(x, y, t)$, in which the x-direction is defined as the in-plane direction of the ion beam, is given by:

$$\frac{\partial h}{\partial t} = -v_0 + \frac{\partial v_0}{\partial \theta}\frac{\partial h}{\partial x} + v_x\frac{\partial^2 h}{\partial x^2} + v_y\frac{\partial^2 h}{\partial y^2} - K\nabla^4 h.$$ (6.2)

The first four terms on the right-hand side describe the ion erosion, where v_0 is the global erosion rate and θ is the global polar angle of incidence. The parameters v_x and v_y link the local sputtering to the local curvature, and depend on the ion beam characteristics, such as energy, species and angle of incidence. More directly these two parameters are functions of a, κ, ρ and θ. The final term in Equation (6.2) accounts for relaxation through surface diffusion, in which the coefficient K depends on the self-diffusivity, the surface energy, the concentration of mobile species and the substrate temperature. The solution of Equation (6.2) is a wavelike morphology, where the wave vector is either parallel or perpendicular to the projected ion beam direction, depending on the polar angle of incidence. For angles smaller than a certain critical angle, ripples are predicted to run perpendicular to the ion beam direction; for larger angles, towards grazing, the ripples are aligned with this direction. In Ref. 198, in Figure 11, calculations of typical $v_x(\theta)$ and $v_y(\theta)$ are given, which show a critical angle $\sim 45°$. Obviously, the precise value of the critical angle depends on the ion beam parameters and the substrate. Figure 6 of Ref. 197 shows a fit, using Equation 6.2, to find $v_x(\theta)$ and $v_y(\theta)$ of Xe^+ ion sputtering of graphite; for this case a critical angle of $64°$ was determined.

The BH-ripple wavelength λ_r is given by:

$$\lambda_r = 2\pi\sqrt{\frac{2K}{v_{max}}},$$ (6.3)

where v_{max} is equal to the maximum of $|v_x|$ and $|v_y|$. At a constant ion flux the amplitude of the ripple pattern A is expected to increase exponentially in time:

$$A \propto \exp\left(\frac{2\pi^2 v_{max}t}{\lambda_r^2}\right),$$ (6.4)

---

*The z'-axis is oriented along the ion beam direction.

from which it is evident that eventually the BH-theory cannot describe the morphology, as the amplitude of the ripple pattern cannot increase indefinitely. For ion induced rippling that follows the BH-model in the initial stages, at high ion dose saturation of the ripple amplitude, or coarsening of the pattern can occur [208, 209].

There are many refinements of the BH-model to explain different patterning phenomena. For instance, for crystalline material the diffusion term $K\nabla^4 h$ is not valid, and may even not be a good approximation. The presence of an Ehrlich-Schwoebel barrier [144, 145] on stepped surfaces, for example, leads to anisotropic diffusion. Still, in derivatives of the BH-model, the basis remains the balance between non-uniform sputtering and surface relaxation.

BH-ripples, parallel and perpendicular, have been observed on Si at elevated temperatures ($T \sim$850-950 K) [195, 209]. In these experiments, the ripples were observed to have a much larger wavelength (100 nm-1 μm) than the typical groove separation distance of 4.2 nm we observe, and they occurred at a much higher ion dose: $\sim$10^5 nm^{-2} versus 5 nm^{-2} in our experiment. Following the BH-model, both of these differences can be qualitatively expected. At higher temperatures, the wavelength is expected to increase, as diffusion leads to surface relaxation on a larger length scale (Equation (6.3)), and a pattern with a larger wavelength develops more slowly (Equation (6.4)). In general, the maximum dose, for which the BH-model can be used to calculate the morphology, decreases with decreasing substrate temperature.

Erlebacher and Aziz studied ion erosion of Si(111) by bombardment with 500 eV Ar$^+$ ions incident at 70° from normal incidence at various substrate temperatures [210]. Ion bombardment at 873 K yielded, after an ion dose of 10^7 nm^{-2}, a parallel ripple pattern, with a wavelength of 580 nm and an amplitude of 20 nm. Sputtering with the same dose at 323 K resulted in a rough, possibly amorphous morphology. Also in this case, the dose used and the wavelength observed were orders of magnitude larger than in our experiment. From later studies [208] it is clear that at such high ion dose the BH-model is no longer valid for the high temperature case, and certainly not for the near room temperature case. In fact, in contrast to metals, sputtering of semiconductors can lead to amorphization at low enough substrate temperatures, see Ref. 211 for an example on Ge(001).

It is tempting to classify the parallel grooves we observed after near grazing incidence sputtering with a low ion dose as ripples, or the onset of ripples, of the BH-type. However, the grooves are the result of a balance between sputtering and reflection of ions, dictated by the state of the surface: on undamaged regions the sputtering yield is zero, because ions are reflected, whereas damaged areas are sputtered significantly. This is a much more pronounced effect than the curvature dependent erosion terms in Equation (6.2). The basic BH-model cannot explain the ion induced morphology we obtained. In fact, the BH-model does not include reflection of ions. In addition, shadowing, the effect that taller surface features block the path of ions to lower regions, is stronger for oblique angles of incidence.

This may lead to the preferential sputtering of mounds with respect to valleys, which is opposite to what is expected from the BH-model.

6.3.2 Atomistic approach

In his review article, when discussing ion erosion of single-crystalline metals, Valbussa [197] discriminates between the *diffusive* and *erosive* sputter regimes. The former is characterized by substrate temperatures that are high enough for diffusion to occur at a rate much faster than the arrival rate of the ions. The predominant effect of the ions is the production of adatoms, clusters, vacancies, and vacancy islands that have more than enough time to find low-energy configurations. Under specific conditions, regarding the ion beam parameters and the substrate temperature, in the diffusive regime, sputtering is equivalent to the deposition of vacancies. Reference 212 offers an example on Ag(001). Even when sputtering is not equivalent to inverse homoepitaxial growth, in the diffusive regime, the crystalline nature of the substrate determines the ion induced morphology, rather than the ion beam parameters.

The erosive sputtering regime for metals requires the absence of large scale diffusion. Hence, the substrate temperatures should be low enough, that the ion induced damaging occurs at a rate much faster than the repair via diffusion. Because of this, thermodynamically unstable structures can be formed. In the erosive regime, sputtering with a large angle of incidence is often found to lead to the creation of surface features, which are elongated along the azimuthal ion beam direction. Grazing incidence ion bombardment of Ag(001) at 180 K shows a parallel ripple pattern already after the sputtering of single monolayers [197].

The transition between the erosive and diffuse regimes depends on the substrate temperature and on the ion beam parameters. Van Dijken *et al.* [213] found that grazing incidence ($\sim 80°$) ion bombardment of Cu(001) with ~ 1 keV Ar^+ leads to nanometer-sized parallel grooves after an ion dose of $\sim 10^2$ nm^{-2} . The wavelength of the pattern was seen to depend on the ion energy for temperatures below 200 K, and above that temperature the determining factor was the substrate temperature. Kim *et al.* [214] showed that on Au(001) the transition between both sputtering regimes could be achieved by varying the ion energy and flux at constant sample temperature. Decreasing both the energy and the flux caused a transition to the diffusive regime: sputtering with a low yield created numerous *add-species* at a sufficiently low rate to allow the formation of equilibrium configurations. Hitherto, classification of sputtering phenomena on the basis of their erosive or diffusive character, was restricted to single-crystalline metals, but can its meaning be extended to semiconductors? Can ion bombardment of Si(111) as presented in this chapter be viewed as either erosive or diffusive?

From the STM movie we have a strong indication of the absence of large scale

diffusion: on the undamaged regions extra-adatoms are bound to half of the unit cell. As the surface becomes damaged, the nature of the diffusion should also change, because the energy barriers depend on the surface structure. There is a large spread in the reported values of the energy barrier for surface mass transport: cf. Refs. 215, 216, and 209, but in general the value is larger than the barrier of extended diffusion on the 7×7 reconstructed surface. Thus, although the diffusion locally occurs at a rate much faster than the arrival rate of the ions, the low-flux, large-angle ion bombardment of Si(111) is best described as erosive: the pattern is dictated by the ion beam direction, and is not an equilibrium structure defined by the crystal.

Similar to our results are those obtained by Hansen *et al.* studying 5 keV Ar$^+$, grazing incidence, ion bombardment of Pt(111) [217]. The authors of Ref. 217 identified an *athermal* regime, between 200 K and 500 K, and a *thermal* regime between 500 K and 700 K, similar in nature to the aforementioned erosive and diffusive regimes, respectively. In the athermal regime, on Pt(111), a pattern parallel to the project ion beam direction develops, which appears to be formed by the coalescence of vacancy grooves, with the same, parallel, orientation. The origin of these grooves is the efficient sputtering of the far end of vacancy islands, whilst the (step edge) diffusion is not effective enough to have an effect on the shape of the grooves. It seems reasonable to expect that also for Si(111) the mobility in the groove is not effective enough at room temperature to influence its shape. On Pt(111), in the thermal regime, full step edge mobility keeps the ion induced vacancy islands close to their equilibrium shape. The fact that the surface morphology develops anisotropy at all, was attributed to *channeling*, in which an ion, incident at a ascending step, travels in between the surface and the first sub-surface layer [218]. Eventually the ion scatters a considerable distance behind the step, causing the emergence of a new vacancy island. Through channeling, vacancy islands are lined up parallel to the ion beam direction.

The origin of parallel grooves on Cu(001), induced by grazing incidence bombardment, was also found to originate from the preferential sputtering of ascending steps [213]; likewise a transition between an erosive and a diffusive regime was reported. Interestingly, on Cu(001) this transition was attributed to the onset of vacancy diffusion, whereas on Pt(111) the efficiency of step edge mobility seems to be the determining factor. Real-time STM would be particularly suited to investigate if this is a generic difference between fcc(001) and fcc(111) metal surfaces; the order of the height of the activation barriers for the different types of diffusion does depend on the crystal symmetry [217].

Finally, we address the origin of the typical lateral separation distance of the grooves of 4.2 nm. While the formation of grooves is of an erosive nature, the limited diffusion seems to be a determining factor in the typical length scales of the pattern. Extra-adatoms that are ejected onto the surface, form clusters of which the size is limited to that of the half unit cell. The typical size of such a cluster is 3.1 nm^2; the typical diameter of a round cluster 2.0 nm, which

is approximately half of the average groove separation distance. In addition to this, the growth of the grooves in the direction of the ion beam is ensured by a modest lateral straggling of the ion trajectories after an impact, the parameter ρ in Equation (6.1). The lateral spread must be smaller than half of the typical separation distance. For 800 eV Ar$^+$ into Si, using SRIM-2008 [219], ρ was calculated to be 1.3 nm. While the trenches grow as a result of the sputtering, material accumulates on either side, and a network of grooves and ridges of a particular size, but without a long range order, develops.

6.4   Summary and conclusions

With the use of real-time STM we have been able to investigate the important erosion and diffusion processes that accompany grazing incidence ion bombardment of Si(111)-7 $\times$ 7. The fact that we continuously imaged the same region of the surface during its erosion enabled us to find the correlation between the local sputtering events and the morphology of the substrate. With a similar, but more 'conventional' STM investigation of sputtering, in which the surface was imaged at various stages of erosion, identifying such a correlation would have been very challenging. The most important reason for this is that it would be very difficult, if not impossible, to image precisely the same sample area before and after the ion bombardment.

The main conclusion to be drawn is that in the initial stages of the bombardment ions are reflected on the undamaged regions and damaged areas are preferentially sputtered. In addition, not all targeted substrate atoms overcome the energy barrier to be sputtered, but some are merely displaced and ejected onto the surface. There, the diffusion of the added atoms is limited to half of the 7 $\times$ 7 unit cell, and clusters of a similar size are formed, analogous to homoepitaxial growth of Si.

The combined effect of erosion and accumulation of material is the formation of grooves and ridges, oriented parallel to the projected ion beam direction. This pattern cannot be described by the Bradley-Harper model of ion induced ripple formation [205], but is similar to those in the erosive, or athermal, sputtering regime, as defined for single-crystalline metals [197].

As a general point, we conclude that the use of real-time STM is an important step towards an atomistic description of ion sputtering in general and pattern formation in particular.

CHAPTER 7

Ion induced smoothing of thin Mo films

An investigation of the effect of low-energy ion bombardment of thin Mo films deposited on Si is presented in this chapter. It is found that the ion erosion can lead to smoothing of the film. A real-time STM study, performed during grazing incidence sputtering (75°), is compared with ion erosion at an angle of incidence of 45°. In the latter case, an initial decrease in roughness is observed, which is quickly followed by an increase when more Mo is removed. The roughening is accompanied by the formation of a ripple pattern, in which the ripples are oriented perpendicular to the azimuthal direction of the ion beam. Sputtering at an angle of incidence of 75° was observed to decrease the roughness of the film continually over the course of the experiment and the removal of a significant amount of Mo. This type of ion erosion is therefore suited as a smoothing treatment of the Mo layers during the production process of Mo-Si multilayer optics, especially as grazing incidence sputtering is not expected to lead to additional intermixing of the deposited layers.

7.1 Introduction

In Chapter 5 the deposition of Mo on Si(111)-7 × 7 and on ion eroded Si(111) was studied. On both substrates the deposited Mo film exhibited a grainy, rough morphology. Recent STM studies of Mo films deposited under industrial conditions, i.e. in a coating facility for multilayer optics, showed a similar morphology [220]. Further comparison between Ref. 220 and the deposition experiments described in this thesis showed that both the difference in deposition flux of two orders of magnitude, as well as the choice of the specific Si substrate have little influence on the film morphology [184]. Besides attempting to control the roughness during growth, or prior to the deposition by altering the substrate, one could try to reduce the roughness of the deposited film. Low-energy ion bombardment proved to be an effective means of thin film smoothing. Ion bombardment is almost always accompanied by sputtering, so if the thickness of the film is a critical parameter, as in multilayer optics, the procedure is as follows. A film, thicker than the required thickness is deposited, followed by the removal of the excess material by ion bombardment. Whether or not the thus obtained layer is smoother than one produced directly at the nominal thickness depends on a number of factors, such as the type of ions, their energy, the angle of incidence, the layer material, the substrate temperature, and the amount of excess material. In addition, sputtering may lead to alterations of the properties of the layer. For example, in multilayer optics, ion induced changes in the density of the material can cause loss of reflectivity, even if the interface roughness is reduced [128].

7.1.1 Ion erosion in the Mo-Si system

For Mo-Si multilayer optics the state of the art is to ion erode every Si layer during production, while the Mo layers are kept as deposited. In any case, it is important that the roughness of the interfaces is reduced at intermediate stages during the production, as the growth is partially conformal [25, 129, 221]. The first attempts to reduce the interface roughness in the Mo-Si system by ion bombardment were actually made on the Mo-on-Si layer [222]. A 10.8 nm Mo layer, deposited on Si, was eroded by Ar^+ ions incident at 45°. A comparison was made between ion energies of 300 eV and 800 eV. It was found that in both cases after an initial decrease in roughness, the roughness increased. For both energies, this transition occurred at the same ion dose, but in the case of the higher energy more material had been removed, approximately 5.6 nm versus 2.8 nm, due to the higher sputtering yield. An explanation for the increase in roughness was found in the ion enhanced crystallization of the Mo layer after a certain ion dose, seemingly unrelated to the ion energy. From this study it was proposed that with ion bombardment at an angle of incidence of 45° the amount of Mo that could be removed with reducing roughness is limited and that it depends on the ion energy. The fact that for the same ion dose for different energies the layer morphology changed in a similar manner indicates that the
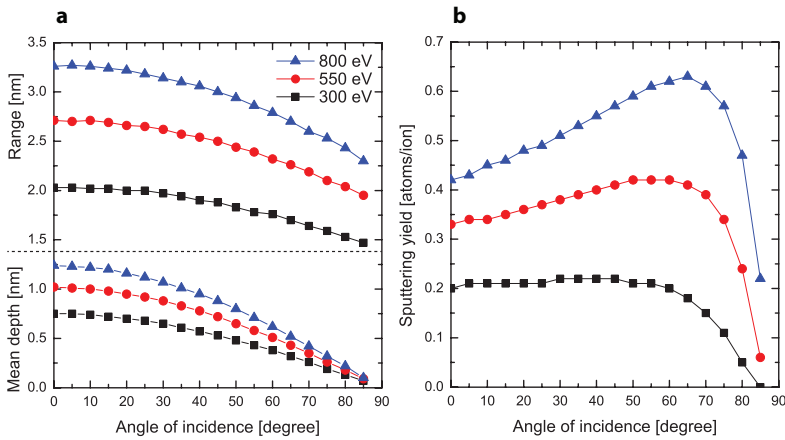
Figure 7.1: Calculated characteristics of Ar^+ ion bombardment of Mo, using SUS-PRE [229]. (a) The mean penetration depth and the range of the ions is plotted versus the polar angle of incidence, for 300 eV, 550 eV and 800 eV ions. The range is defined as the depth above which 95% of the ions are stopped and the residual energy is negligible. (b) The sputtering yield for the different energies is plotted versus the angle of incidence.

morphology is affected by more than the removal of material. For example, the production of adatoms, clusters, vacancies, and vacancy islands, as well as ion induced grain boundary migration can lead to coarsening of the layer through enhanced grain growth, similar to annealing [223–228].

If during the ion erosion of a layer the range of the ions in the target exceeds the layer thickness, additional intermixing of the multilayer species and loss of reflectivity is to be expected [128]. Following Sigmund's theory of sputtering [206, 207] the energy of the ions is distributed in the near-surface region according to a Gaussian, see Equation (6.1). The mean range and straggling of the ions depend on the target and ion species and is a function of the energy and angle of incidence of the ions. In addition to the requirements of the thickness of the excess layer as discussed in the previous paragraph, the risk of additional compound formation limits the choice of ion beam parameters. Figure 7.1 shows the range of Ar^+ ions into Mo, as well as the sputtering yield, for various energies and angles of incidence, calculated using SUSPRE [229]. This computer program can be used to calculate both the ion implantation depth of any type of ion into any type of solid target, as well as the energy dissipation profile in the target. Subsequently, using Sigmund's theory of sputtering [206], the sputtering yield is calculated.

From these calculations it is clear that bombarding a Mo layer with 800 eV Ar^+, while removing material up to the required thickness of $\sim$3 nm, might lead to additional intermixing. This was also found experimentally by Schlatmann *et al.*,

who produced Mo-Si multilayers with a period of 6 nm (approximately 3.5 nm Si and 2.5 nm Mo) [129], and investigated the effect of 45° ion erosion on the reflectivity. To avoid intermixing an ion energy of 300 eV was chosen and Kr^+ ions were used, as these have a smaller penetration depth than Ar^+ ions. Under these conditions the removal of an excess layer of 1.3 nm Mo was found to only modestly reduce the roughness. As a consequence, sputtering of each Mo layer could not prevent the development of conformal roughness during the fabrication of the multilayer structure. Ion erosion of Si, with the same ion beam parameters, had a smoothing effect that was large enough to inhibit the increase of interface roughness during production. Sputtering of all layers did not further improve the reflectivity of the multilayer mirror. For this reason, the production process of modern Mo-Si multilayer optics, of 50 periods and an approximate total thickness of 350 nm, includes an ion erosion step of the Si layers, but not of the Mo layers [230]. Although the periodic ion treatment of the Si layers suffices to maintain a reasonable interface roughness throughout the multilayer, the reflectivity would increase by the reduction of the roughness of the Mo-on-Si layers.

7.1.2   Grazing incidence ion induced smoothing

Hitherto, the optimization of the ion erosion procedure of the Mo layer has been limited to investigating the effects of the ion species, energy and the thickness of the excess layer. Intermixing and an increasing roughness through crystallization proved to be the limiting factors. Both effects might be tackled by changing the angle of incidence of the ions to larger values. From the calculations displayed in Figure 7.1, we find that the penetration depth of the ions is smaller at larger angles, so that a higher ion energy can be chosen without creating additional intermixing during bombardment. Grazing incidence sputtering and a high sputtering yield, which is achieved for angles that are not too large (Figure 7.1(b)), may lead to sputtering in the *erosive* regime, as defined for single-crystalline metals [197] and discussed in Section 6.3.2. Ion erosion in this regime is characterized by a morphology dictated by the ion beam parameters, rather than by surface relaxation. The combined effect of reflection of ions on smooth regions, preferential sputtering of locally rough areas and shadowing can lead to roughness reduction, depending on the initial surface morphology.

There are but few recordings in literature where large-angle sputtering was used to successfully reduce surface roughness. Spiller used grazing incidence ($> 80°$) Ar^+ ion sputtering to reduce the interface roughness of the RhRu-C and the Co-C multilayer systems [186, 231]. Only the C layer was bombarded, as on the metals crystallization was an issue. The experiments were performed at a maximum ion energy of respectively 300 eV and 500 eV. The roughened surface of crystalline GaAs was successfully smoothed by using 1 keV Ar^+ grazing incidence ion bombardment [232]. Grazing incidence sputtering was used to smooth a

single 60 nm thick Ca film and a CaF$_2$ substrate [233, 234] using respectively 3 keV and 4.5 keV Ar$^+$ ions. For the Mo-Si system such high energies cannot be used, as even at extremely grazing angles intermixing is to be expected [219, 229]. Still, for reasons discussed in the previous paragraph a high ion energy is beneficial. In this chapter we present an investigation of the effect of grazing incidence sputtering of a Mo film deposited on Si, using an ion energy that corresponds to a significant sputtering yield, but with which intermixing is not to be expected. The results are compared with bombardment at 45°.

7.2 Experimental details

The Mo films where deposited by e-beam evaporation onto a Si(111) substrate. The deposited amount corresponded to a nominal thickness of 5.5±0.5 nm. The films were bombarded by 800 eV Ar$^+$ ions with an ion flux* was 2×10^{16} m^{-2} s^{-1}. During the bombardment the sample was at room temperature. The base pressure of the UHV chamber was below 5 × 10^{-11} mbar. During the experiment the pressure in the UHV chamber increased to 2×10^{-8} mbar, while the pressure in the ionization stage of the ion source was 1.5×10^{-4} mbar. STM imaging was done at a sample voltage of +2 V and a tunneling current of 200 pA.

The films were bombarded by ions incident at angles of 75° and 45° from normal incidence. At the larger angle, two experiments were conducted: one experiment where the surface was imaged during bombardment and one where the surface was inspected at intermediate stages of the sputtering. The former was performed to investigate the local sputtering effects, the latter to exclude any effects of the presence of the tip on the process. Sputtering at 45° was only studied by interrupting the ion flux and imaging the surface.

In comparison to the experiment reported in Chapter 6, the ion flux is much higher in the present experiment: approximately two orders of magnitude. As a consequence, during a real-time experiment the ion current on the STM-tip I_i becomes much larger than the typical tunneling current I_t. Still, one can perform STM by operating the feedback system at a higher setpoint tunneling current, but this may lead to imaging problems for the following reason. In the STM feedback loop the *IV*-converter converts I_t to a voltage V_t, with $V_t \propto I_t$. Because the tunneling current depends on the tip-sample distance approximately exponentially, V_t is converted to V_f by a logarithmic amplifier according to:

$$V_f = K \log \left(\frac{V_t}{V_{ref}} \right), \tag{7.1}$$

where K is a constant and V_{ref} some reference voltage. V_f is approximately

---

*The ion flux was estimated from the current density on the sample cup, see Figure 2.3, not taking into account the effect of the generation of secondary electrons on the measured ion current.
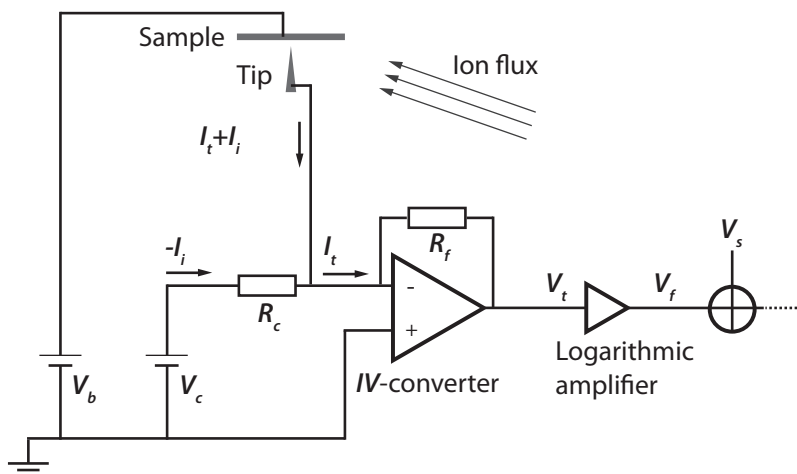
Figure 7.2:   A current source, consisting of a controlled voltage source V_c, and a resistor R_c at the input of the *IV*-converter, compensates the ion current on the tip I_i, so that the *IV*-converter exclusively measures the tunneling current I_t. The other symbols represent the feedback resistor R_f, the tip-sample bias voltage source V_b, the output of the *IV*-converter V_t, the output of the logarithmic amplifier V_f and the setpoint value V_s.

proportional to the tip-sample distance and is compared to the setpoint value V_s. The error signal $V_f - V_s$ is proportional to the error in the tip-sample distance. It is clear that with an ion current on the tip, the total current at the input of the *IV*-converter, $I_t + I_i$, is not exponentially dependent on the tip-sample distance. As the sensitivity of the logarithmic amplifier dV_f/dV_t is proportional to V_t^{-1}, the total gain of the feedback loop, including the gain of the PI-regulator and the response of the piezoelectric scanner, might be too low to track the surface. Furthermore, if $I_t + I_i$ is larger than the limit of the *IV*-converter, which in our case is 10 nA, it is impossible to perform STM in any case.

A simple solution is to compensate I_i by adding another, low-noise current source that supplies $-I_i$ to the tip, as indicated in Figure 7.2. In our case the current source consists of a resistor R_c at the input of the *IV*-converter, shielded by its container and a voltage supply. The thermal noise current of the 10 MΩ resistor into the *IV*-converter is 9 pA at room temperature over the full 50 kHz bandwidth, much less than the intrinsic noise of the *IV*-converter. The voltage source, with a noise level below 0.1 mV, does not contribute significantly to the noise. During the real-time experiments presented in this chapter an offset current of 10.5 nA was used to compensate for the ion current on the tip.

7.3 Results and discussion

7.3.1 Sputtering at 75°

The real-time STM experiment consists of an STM movie of 185 frames of 95×95 nm^2 captured during bombardment with a final dose of 3.5×10^2 nm^{-2}. Figure 7.3 shows selected frames from this movie, which is available as supplementary material [235]. The surface morphology can be characterized by the surface width $w(t)$, the lateral correlation length $\xi(t)$ and the roughness exponent $H(t)$, which can be retrieved from the height-difference correlation function $C_H(r, t)$ or the autocorrelation function $C_A(r, t)$. We use the same conventions as in Chapter 5: ξ is defined through $C_A(\xi, t) = e^{-1} C_A(0, t)$. Figure 7.4 shows how $w(t)$, $\xi(t)$, and $H(t)$ develop during the sputtering.

Over the course of the experiment the roughness decreases from 0.51 ± 0.05 nm to 0.11 ± 0.02 nm. In the initial stages, up to a dose of approximately 1.0×10^2 nm^{-2} the typical lateral scale on which the roughness is observed is constant: the Mo grains reduce in height, but do not change in width, cf. Figures 7.3(a) and (b). An explanation can be found by considering the effect of shadowing: the taller surface features block the path of the ions to the lower regions, leading to a preferential sputtering of the tops of the grains. This leads to a smoothing effect as it evens out the height differences between the grains. The STM movie [235] shows that up to a dose of 20 nm^{-2} this is the predominant smoothing mechanism. Above that ion dose, the morphology develops differently. In addition to smoothing, the network of grains reorganizes. Figure 7.5 serves to illustrate this. It appears if some grains disappear completely between frames, whereas new grains seem to suddenly form. This reorganization is not accompanied by a change of the average grain size*, as has been determined directly from the images and can be also inferred from the lateral correlation length in Figure 7.4(c), which does not significantly change. The reorganization of the grains may be due to the fact that high-energy configurations are formed during the sputtering of the film and that a relaxation takes place, which is accompanied by the migration of grain boundaries. Commonly, grain boundary migration is associated with grain growth, which interestingly seems not to occur initially, i.e. up to a dose of 1.0×10^2 nm^{-2}. It has been found that the energy supplied by ion bombardment can drive grain boundary migration, and grain growth, very effectively [223–228]; the order of magnitude of the used ion energies ranges between 1 keV and several MeV. Ion bombardment during or after deposition can also lead to the growth of grains with a preferential crystallographic orientation, e.g. due to the preferential sputtering of grains with a certain orientation; this effect depends strongly on the angle of incidence of the ions [236–239].

While the smoothing of the film continues and seemingly approaches a constant value, the morphology develops differently yet again in the later stages of the

---

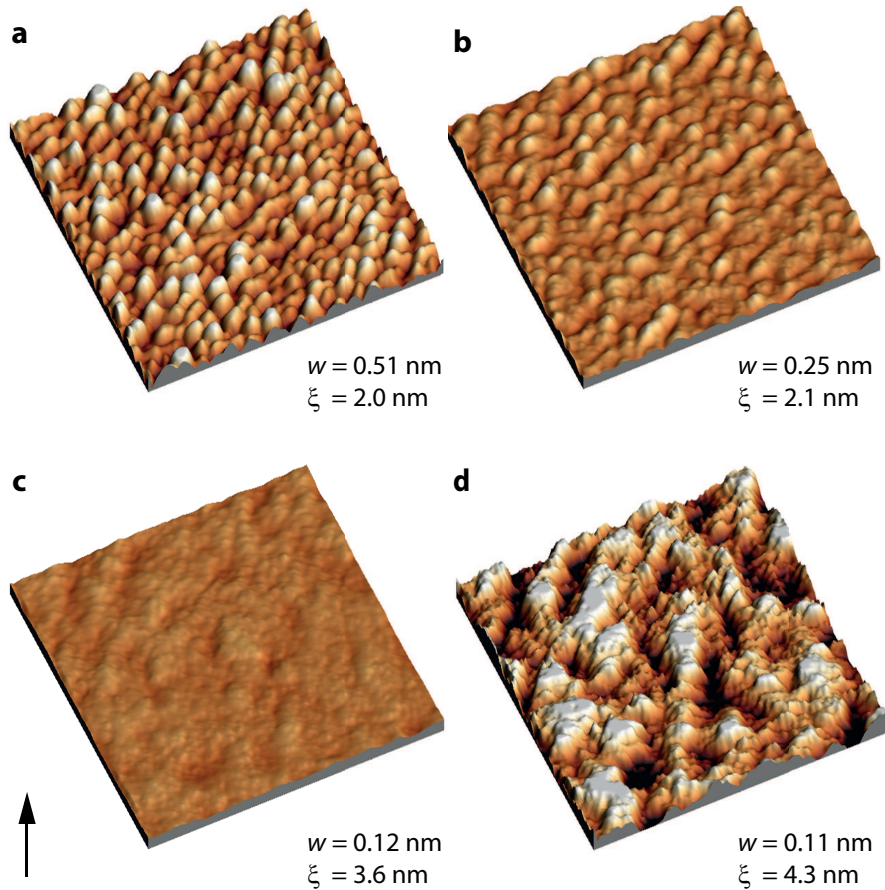*We have determined a marginally small increase in the average grain size.

Figure 7.3: STM images (95×95 nm^2) from a movie [235] captured during the $75°$ ion bombardment of a 5.5 nm thick Mo film on Si(111). The sequence shows (a) the initial surface and in (b-d) the smoothing of the surface after an ion dose of respectively 54, 2.3×10^2 and 3.3×10^2 nm^{-2}, which corresponds to an estimated amount of removed Mo of 0.5, 2.0, and 2.9 nm. The surface width w, the lateral correlation length ξ, and the projected ion beam direction (arrow) are indicated. The height scale, from black to white, for images (a), (b), and (c) is the same (2.3 nm) to illustrate the smoothing effect. The scale for image (d) is different (0.4 nm) to reveal more detail. The grooves and ridges that run parallel to the ion beam show the erosive nature of the sputtering.
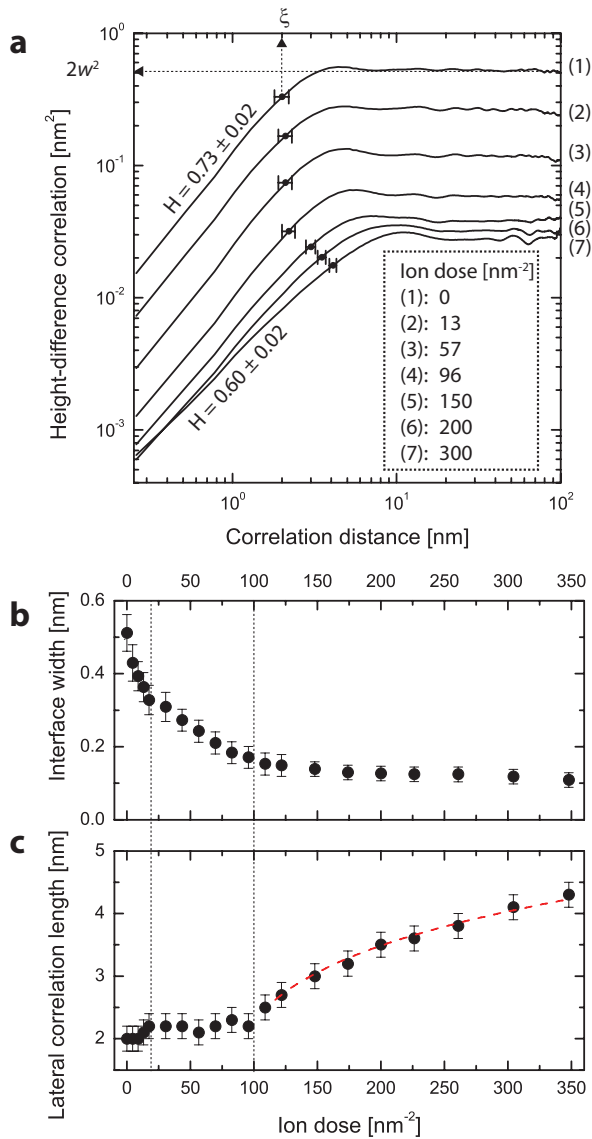
Figure 7.4: (a) Graphs (1-7) show the height-difference correlation function $C_H(r)$ at various stages in the experiment. From $C_H(r)$ the surface width $w(t)$, the lateral correlation length $\xi(t)$ and the roughness exponent $H(t)$ are found. (b) $w(t)$ is plotted versus the ion dose: the sputtering reduces the roughness of the surface. (c) In the initial stages of the experiment $\xi(t)$ is approximately constant. After an ion dose of approximately 1.0×10^2 nm^{-2} $\xi(t)$ increases as $t^{0.24\pm0.04}$; the dashed line shows the fit. The vertical lines in (b) and (c) are the boundaries of the regimes discussed in the text. A dose of 2.8×10^2 nm^{-2} corresponds to an estimated amount of removed material of 2.5 nm.

Figure 7.5: STM images (50×50 nm^2) taken during the sputtering of a Mo film on Si. The full color scale spans (a) 2.7, (b) 2.3 and (c) 2.0 nm. The images sh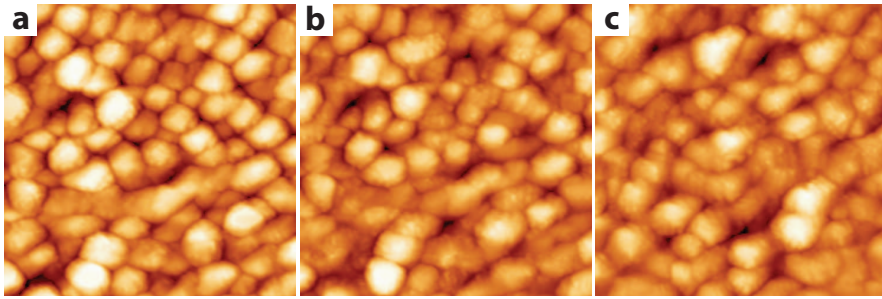ow the same surface area after an ion dose of respectively 0, 13 and 26 nm^{-2}. Below a dose of ~ 20 nm^{-2} the surface is smoothed predominately by the preferential sputtering of taller grains. Between ~ 20 nm^{-2} and 1.0×10^2 nm^{-2} the surface reorganizes: some grains seem to disappear between frames, while new grains seem to form. Interestingly, the average grain size does not increase. This reorganization must be accompanied by grain boundary migration, which is an effect that is known to occur during sputtering.

experiment. Above an ion dose of 1.0×10^2 nm^{-2} there is only a minor reduction of $w(t)$. The residual roughness is dominated by the formation of a disordered network of grooves and ridges, of which most are aligned with the projected ion beam direction (see Figure 7.3(d)). The correlation length increases in time according to a power law: $\xi(t) \propto t^{0.24 \pm 0.04}$, in which $t = 0$ corresponds to an ion dose of 1.0×10^2 nm^{-2}. One expects that the coarsening would be associated by a roughening of the surface. We suggest that the energy deposited by the ion beam in the top layers of the substrate leads to coarsening, which would be accompanied by roughening in the absence of the eroding effect of the sputtering. However, as the sputtering *is* accompanied by erosion, an increase in the roughness is suppressed by the efficient sputtering of emerging features.

We presume that the film would have further coarsened, if we would have continued the sputtering[*]. As the lateral correlation length would have kept increasing, we speculate that eventually also the roughness would have increased. The reason for this is that the ion bombardment can only mitigate height differences up to a certain lateral separation. This typical in-plane length scale should depend critically on the angle of incidence of the ions.

To judge whether or not it would be beneficial to include an ion erosion treatment of the Mo layers in the production process of Mo-Si multilayers, we must compare the results of the present experiment with the roughness after the deposition of the nominal thickness of the Mo layer. In Chapter 5 we found that after the deposition of 3 nm of Mo on Si(111) the interface width was 0.24 nm,

---

[*]Here we neglect the fact that at some point we would have removed all the Mo and would be sputtering the Si; we consider the hypothetical situation of an infinitely thick film.
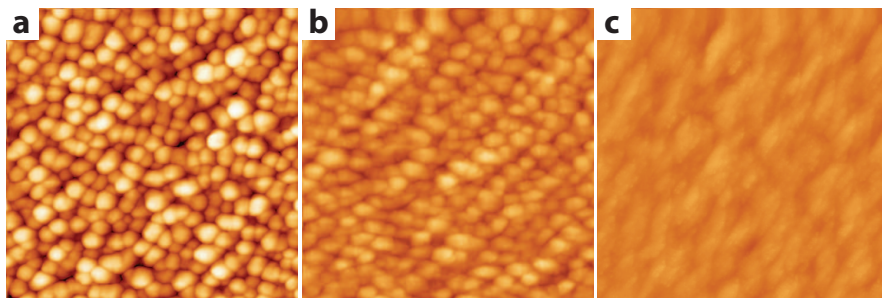
Figure 7.6: STM images (95×95×4.1 nm^2) taken during the sputtering (angle of incidence 75°) of a Mo film of a nominal thickness of 5.5±0.5 nm deposited on Si(111) after an ion dose of respectively 0, 45 and 2.8×10^2 nm^{-2}. The surface width reduces from (a) 0.71, to (b) 0.34, to (c) 0.14 nm. The images do not show the same surface area.

which is also the typical roughness of a 3 nm thick Mo layer in Mo-Si multilayer systems (see Section 5.6). The main downside of our experimental method is that we have no precise measure of the amount of removed material. We can however make an estimate on the basis of the calculated sputtering yield (see Figure 7.1(b)) and the ion dose. With a sputtering yield of 0.57 atoms per ion*, an ion dose of 1.1×10^2 nm^{-2} would be required to remove 1 nm of bulk Mo. After sputtering with an ion dose of 2.8×10^2 nm^{-2}† 2.5 nm would then be removed and the estimated thickness of the Mo layer at that point would be 3 nm, with a roughness of 0.11 nm, which is significantly smoother than the layer obtained after deposition of that amount.

To investigate if the presence of the STM-tip was of influence on the results, we compared the experiment with sputtering without simultaneous STM imaging. Figure 7.6 shows the surface at different stages of erosion. These images back-up the conclusions drawn from the real-time experiment: sputtering with 800 eV Ar$^+$ ions at an angle of incidence of 75° leads to smoothing, even when the film coarsens.

7.3.2 Sputtering at 45°

Although sputtering at an angle of incidence of 45° with 800 eV Ar$^+$ ions is known to lead to intermixing [129], it is interesting to investigate how the morphology of the Mo film develops, if we change the angle of incidence with respect to the previous experiment. At an angle of incidence of 45° the calculated sputtering

---

*If ions are reflected on smooth surface areas, we must expect a decreasing average sputtering yield as the film becomes smoother.

†Note that we continued the sputtering to a final dose of 3.5×10^2 nm^{-2}, which corresponds to the removal of approximately 3 nm.

a

b

c

w = 0.38 nm
ξ = 1.9 nm

w = 0.15 nm
ξ = 1.6 nm

w = 0.23 nm
ξ = 6.0 nm

d

w = 0.33 nm
ξ = 6.4 nm
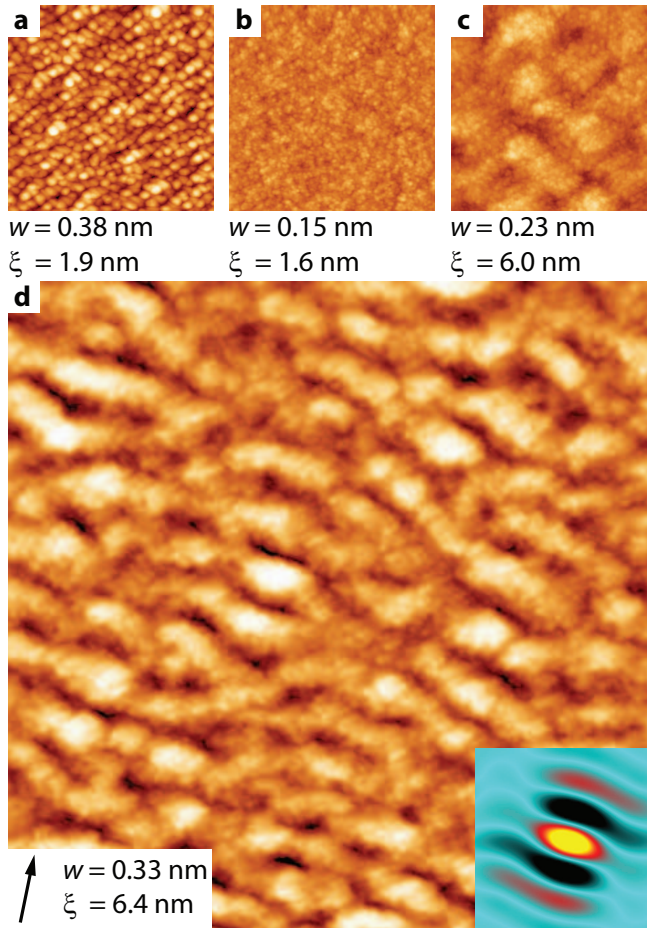
Figure 7.7: STM images ((a-c) $90 \times 90 \times 2.5$ nm^3 and (d) $285 \times 285 \times 2.5$ nm^3; printed to scale) recorded after interrupting the sputtering (angle of incidence $45°$) of a Mo film on Si. The images were taken after an ion dose of respectively 0, 75, 2.3×10^2 and 3.8×10^2 nm^{-2}, which corresponds to estimated amounts of removed Mo of 0, 0.7, 2.1 and 3.5 nm. The surface width *w* and the lateral correlation length ξ are indicated. The arrow in (d) indicates the projected ion beam direction; the inset shows the autocorrelation function of the image (window size is 80×80 nm^2). After an initial decrease of the roughness, a ripple pattern, perpendicular to the ion beam direction develops and the roughness increases. The images do not show the precise same surface area.

yield is 0.57 (see Figure 7.1(b)), which is the same yield as at 75°. As also the ion energy is the same for both experiments, the choice of these two particular angles allows that we can attribute any difference between the two experiments exclusively to the angle of incidence.

Figure 7.7 shows STM images taken at intermediated stages during the process. Initially, up to a dose of 75 nm^{-2}, the surface becomes significantly smoother with a finer structure: $w(t)$ decreases from 0.38 nm to 0.15 nm and ξ decreases from 1.9 nm to 1.6 nm. At that point the estimated amount of removed material is 0.7 nm, and the film is not yet at the required thickness. Further sputtering leads to coarsening and an increased roughness. A similar roughness evolution was found on thicker Mo films, as discussed in Section 7.1.1. In our case, after the removal of 2.5 nm the film is not smoother than the film obtained after deposition of the nominal thickness. Sputtering at 45°, while removing an excess layer of 2.5 nm*, which is required to ion erode a film with a thickness of 5.5 nm to the proper thickness, is not the right approach for smoothing of the Mo layers. The evolution of the roughness suggests that the removal of a thinner excess layer, of ~0.7 nm, would be a suitable approach, although we cannot be certain. The morphology of a Mo film with a thickness of 3.7 nm is different than that of film with a thickness of 5.5 nm. The difference in initial morphology certainly has its influence on the process. Even if the problem of intermixing would not occur for 45° sputtering, grazing incidence sputtering would still be the more flexible approach, as it was found to monotonically decrease the roughness, even when the film coarsened.

7.3.3 Ripple formation

In the final stages of the 45° experiment a ripple pattern perpendicular to the projected ion beam direction is observed. According to the Bradley-Harper (BH) model of ion induced rippling, Equation (6.2), such a pattern is expected to develop for an angle of incidence below the critical value θ_c. Comparing the results with those from the 75° sputtering experiments, more specifically with the morphology of Figure 7.3(d), we conclude that for the system under investigation 45° $< \theta_c <$ 75°. It is however not clear whether the BH model is suited to describe the pattern formation for our particular system, for both angles of incidence.

After an initial transient period, the BH model predicts a pattern with a fixed wavelength and an increasing amplitude upon further sputtering [198]. For the 75° sputtering experiment, we have suggested that the effect of shadowing played an important role in the development of the morphology of the Mo film. In addition, on the basis of our results of Chapter 6, we can expect that on smooth surface areas some of the ions were reflected during the bombardment, although

---

*As with the grazing incidence experiment, at the end of this experiment we removed more than the required 2.5 nm, approximately 3.5 nm.

the substrate is different for the experiments discussed here. Both shadowing and reflection are not incorporated in the BH model and so we cannot expect that the model would fully describe the experimental observations of the 75° experiment. However, in the final stages of the experiment we do observe the development of an anisotropic morphology. Therefore, it may be that if we would have continued the sputtering, we would have found that eventually the evolution of the morphology would have followed the predictions of the BH model. In this scenario, we should expect that the roughness would have started to increase after the correlation length had increased beyond the length scale, on which height differences could be reduced by the ion erosion.

The BH model should be better suited to describe the 45° sputtering experiment than the 75° experiment, as for the smaller angle of incidence the effects of shadowing and ion reflections should be of less influence. After an ion dose of $\sim$200 nm^{-2} (Figure 7.7(c)) a ripple pattern started to become visible, of which the wavelength did not significantly increase upon further sputtering, while the roughness did increase. Both trends are to be expected within the BH model, although the ripple-amplitude should grow exponentially (Equation 6.4), which we did not observe*. This implies that also for the 45° experiment the steady growth of BH ripples had not yet started when the experiment was finished.

7.3.4   Can 75° sputtering smooth any surface?

Finally, we explore the limitations of 800 eV Ar$^+$ sputtering at an angle of incidence of 75° as a smoothing technique. We expect that if the lateral correlation length is too large, the ion erosion does not lead to a reduction of the surface roughness, because of the limited length scale on which the smoothing is active. We put this expectation to the test by applying the 75° sputtering treatment to a Mo film that was first roughened by ion bombardment at an angle of incidence of 45° (Figure 7.7(d)). Based on the estimated amount of Mo removed, 3.5 nm of an initial 5.5 nm, and on the fact that intermixing has to be expected during 45° sputtering, we expect that the resulting starting situation for the grazing incidence sputtering is a Mo$_x$Si$_y$ film. Although the precise nature of the film is unknown, it is still interesting to inspect the effects of grazing incidence sputtering. In a real-time experiment the substrate was bombarded with a final dose of 4.0×10^2 nm^{-2}. The results are depicted in Figure 7.8. The morphology changes by the preferential sputtering of the mounds on the side closest to the ion source and the valleys are elongated in the direction of the ion beam. This is accompanied by an increase of the surface width from $w = 0.33$ nm to $w = 0.39$ nm. The fact that this time we do not find a smoothing effect can be understood from a simple geometric argument. In the present experiment the mound separation is larger than that of the as-deposited Mo film, while the

---

*We have also imaged the surface at stages between the situation depicted in Figures 7.7(c) and (d). The roughness increased, but certainly not exponentially.
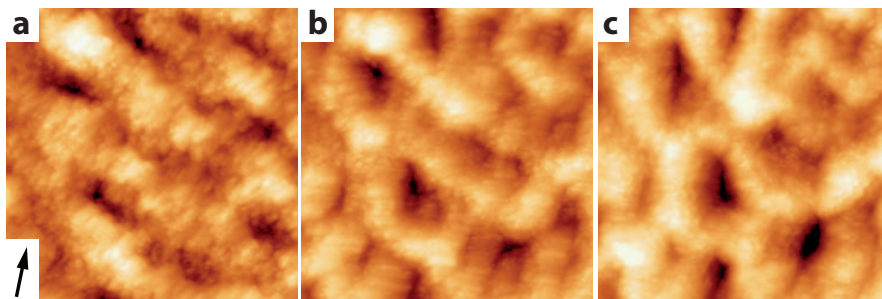
Figure 7.8: STM images ($95 \times 95 \times 2.5$ nm^3) taken during the sputtering, at angle of incidence of 75°, of a Mo film on Si(111) that had been eroded by 45° sputtering prior to the experiment. The images were taken after an ion dose of respectively 0, 2.0×10^2 and 4.0×10^2 nm^{-2} and show the same surface area. The sputtering does not have a smoothing effect: the surface width increased from $w = 0.33$ nm to $w = 0.39$ nm. The morphology changed by the preferential sputtering of the side of the mounds closest to the ion source as can be seen by the elongation of the valleys in the direction of the ion beam, which is indicated by the arrow.

roughness is smaller. The effect is that taller mounds do not cast a shadow on lower regions and the roughness is not reduced. In general, for shadowing to become a smoothing agent, the angle of incidence should be increased as the ratio w/ξ decreases. Because the sputtering yield decreases for angles towards grazing incidence, the ion energy should be increased to ensure sputtering in the erosive regime. For the Mo-Si multilayer system, the choice of the ion energy is limited by the occurrence of intermixing at higher energies.

7.4 Conclusions and outlook

The experiments presented in this chapter provide direct evidence that sputtering at an angle of incidence of 75° with 800 eV Ar$^+$ ions can be used to smooth the Mo layers in Mo-Si multilayer systems. We observed, through real-time STM experiments of grazing incidence sputtering of Mo films on Si(111), how the ion bombardment caused a very efficient reduction of the surface roughness, which even continued while the films coarsened. The smoothing mechanism relies partly on the preferential sputtering of tall surface features, which cast a shadow on lower regions that remain 'out of sight' of the ion beam. Another effect that was found to occur during the ion erosion, is the reorganization of the polycrystalline grain boundary network through grain boundary migration, which initially does not lead to coarsening. Even when the coarsening does set in, the roughness keeps on reducing to finally approach a constant value. We expect that upon further sputtering the roughness would have started to increase, as the smoothing effect of the ion erosion process can only mitigate height differences

up to a certain length scale.

The effect of the angle of incidence of the ions was studied by a comparison between sputtering at 75° and at 45°. For the two situations both the ion energy, as well as the calculated sputtering yield were the same. The ion erosion with the lower angle also led to an initial smoothing, followed by the coarsening and roughening of the film, which was accompanied by the development of a ripple pattern oriented perpendicular to the ion beam. The large differences between the two experiments, which resulted solely from the change of the angle of incidence, show how crucial this parameter is. For the ultimate smoothing recipe, also the ion energy, the ion mass, and the required ion dose to remove the excess layer are of critical importance. For grazing incidence sputtering for example, if the ion energy is chosen to be too low, the effect of the sputtering is that still a significant amount of energy is introduced, which leads to coarsening. However, as the sputtering yield is too modest, the roughening that commonly accompanies the coarsening, cannot be balanced by the limited eroding effect of the ion bombardment.

Regarding Mo-Si multilayer optics, grazing incidence sputtering of the Mo layers has the added value that it is not to be expected to lead to additional intermixing of the deposited layers, as the penetration depth of the ions is very modest, in contrast to sputtering at a smaller angle of incidence. The real test of the applicability of the sputtering procedure would be to produce a multilayer mirror including an ion bombardment treatment of the Mo layers to investigate the effect on the reflectivity. We investigated the main properties of the procedure, but we have not searched for an optimal combination of ion beam parameters: the type of ions, their energy, the flux and the angle of incidence. Also, we have not investigated the role of the thickness of the excess layer. A commercial coating facility would be suited to explore the process further as the accurate layer thickness and the reflectivity of the multilayer can be monitored *in situ* during the deposition and erosion of the layers [128]. We can imagine that the ideal recipe for the smoothing of the Mo layers might be to deposit only a small excess layer, and to use the shadowing effect to very efficiently reduce the roughness. Besides the fact that this would be a relatively fast approach, it would also keep the amount of wasted Mo to a minimum. If the anisotropic morphology that develops during the grazing incidence sputtering procedure is a problem for the performance of the multilayer structures, rotation of the sample or sputtering from several sources at different azimuthal angles of incidence should provide a direct solution.

During the production of the multilayer optics it is common practice to bombard every Si layer with ions from a source mounted at approximately 40° from the surface normal. For the smoothing of Si this proved to be the best choice [240]. Recent research on Si(001) showed that for angles of incidence between ∼35° and ∼60° a sputtered Si sample remains smooth nearly independently of the type of noble gas ions or the ion energy, whereas for larger angles pattern formation was

seen to lead to roughening [241, 242]. Hence, it appears that Mo and Si cannot be smoothed by the same procedure and that the incorporation of a treatment of the Mo layer requires a second source positioned at a different angle with respect to the substrate.

If the coating setup is constructed in such a way that a source at a more grazing angle cannot be mounted, it possible to use only one source for the erosion of both the Si and the Mo layers. If the substrate cannot be tilted, one might deflect the ions to the desired angle of incidence using electrostatic or magnetic optics. This can be done for example by applying an electric field perpendicular to the substrate, to decelerate the ions, thereby changing their angle of incidence to a larger value. Alternatively, a magnetic field could be applied parallel to the surface and perpendicular to the azimuthal direction of the ions to bend the path of the ions to the desired angle of incidence.

Including the ion smoothing of the Mo layers into the production process would increase the reflectivity of the multilayer optics, but it will come at the cost of additional production time. As Si grows conformally on Mo [128], one could consider to ion erode only all Mo layers, as this would increase the reflectivity possibly even more for the following reason. The optical contrast in a multilayer is enhanced by the reduction of the density of the spacer material. Si exhibits after deposition by e-beam evaporation a density of 90% of the bulk value, which can even be decreased by the implantation of H^+ [243]. This advantage is partly lost by the conventional ion erosion treatment for Si [129].

Finally, we speculate that the grazing incidence ion sputtering approach described in this chapter is not limited to thin Mo films. Other (metal) films might equally well be smoothed by a similar treatment, provided that the sputtering is of an erosive nature and depending on the initial morphology of the deposited film.

Summary (for the layman)

In this thesis I present my research on the physics of some key processes in the production of thin films. A thin film is a layer of material, of which the thickness is of the order of nanometers (nm) to micrometers (μm)[*]. In modern society thin film technology plays a significant role, which is reflected in the large variety of applications of thin film systems in daily life. For instance, decorative coatings on jewellery as well as coatings on drill bits to harden the surface are thin films. Other examples include the very thin layers of material in computer chips and optical coatings, such as anti-reflection coatings on photographic lenses and spectacles.

Commonly, a thin film is produced by depositing a material onto a substrate, e.g. by means of thermal deposition. Using this particular method, to start the film growth process, a piece of material, often termed the target, is heated to a temperature around its melting point. From the hot target, which faces the substrate, material is evaporated and single atoms (or small clusters of atoms) of the target material arrive at the substrate. As single, adsorbed atoms often have a significant mobility on a surface at room temperature, they move around on the substrate in the initial stages of the process, until they encounter other deposited atoms. The atoms bond and form small clusters that become immobile as they become larger. As more material is deposited, these clusters grow by direct deposition of atoms onto the clusters as well as by diffusion of deposited atoms towards the clusters. At some point the clusters come into contact with each other and the film closes. By continuing the process after the closure of the film, its thickness can be increased to the required value.

Various parameters of the deposition process, most notably the rate at which

---

[*]A μm equals 0.001 mm; a nm is equal to 0.000001 mm.

the atoms arrive at the substrate, and the temperature of the substrate that influences how mobile the deposited atoms are, determine the morphology of the film, i.e. its shape and texture. The properties of a thin film, e.g. its electrical conductivity, hardness, and optical reflectivity, depend on the morphology*. Thus, by controlling the deposition process, and hence the morphology, one can optimize the film properties.

In addition to tuning the deposition parameters to obtain the desired type of film morphology, one can also alter the structure of the film after its deposition. A very effective way to change the properties of a deposited film, which was also used in some of the experiments described in this thesis, is to bombard the film with charged particles: ions. This ion bombardment results not only in a reshuffling of the deposited atoms, but often also in the removal of atoms from the film, which is called sputtering. Several parameters can be tuned to alter the effect of the ion erosion. These include the mass of the ions, the impact velocity (energy), and the angle at which the ions strike the surface.

In order to produce the desired thin film, both the deposition and post-deposition processes can be optimized by varying the process parameters and successively determining the effect on the film morphology. Such a trial-and-error approach can lead to a suitable production recipe, but there is also another approach. If one would understand the evolution of the morphology of a film during its deposition and during modification by ion bombardment on a fundamental level, one could very effectively tune the fabrication process to optimize the film properties. The motivation for the research described in this thesis is that ultimately, through a profound understanding of the processes that determine the morphology of a thin film, the production can be tuned such that one can make the perfect thin film, for the desired application.

As with all materials, the building blocks of thin films are single atoms or molecules. Therefore, if one seeks a fundamental understanding of thin film production, one needs to study it on the atomic scale. The analytical instrument that I used in the experiments described in this thesis, is a special type of microscope that enables one to visualize material surfaces on the scale of single atoms: the scanning tunneling microscope (STM)[†]. An STM uses a very sharp needle, the tip, to 'feel' the surface profile. The tip is moved, most commonly in a straight line, across the surface under investigation and the height variations that are detected, are recorded. Multiple, closely spaced, parallel scan lines are used to generate an image of the surface.

Scanning tunneling microscopy has often been used to study material deposition and ion erosion, but for this type of research the technique has one major draw-

---

*For instance, a thin film that is used as a mirror, must have a very smooth surface.

[†]With a conventional optical microscope it is not possible to resolve single atoms. Using the best optical microscope, one can distinguish two features when they are typically 200 nm or more apart. The separation of neighbouring atoms in solid state matter is much smaller: typically 0.3 nm.

back. With a regular STM setup it is impossible, or at least very challenging, to deposit material onto a substrate or bombard it with ions, *while* imaging with the STM. Almost all STM investigations of deposition and ion erosion were performed *after* the film had been produced or modified. Although one can gain information on the morphology of the film on the atomic scale, no direct insight is gained in the processes that have led to the specific film morphology. To be able to investigate thin film deposition and ion erosion with atomic-scale resolution *during* the execution of these processes, a part of my PhD-project was to design and to construct a novel, dedicated STM, which would enable this type of research. In Chapter 2 this new instrument is presented.

In contrast to the extreme magnifying power of an STM stands its very low imaging rate: a typical STM image takes several minutes to obtain. This is caused by the fact that the tip has to be scanned, line-by-line, across the surface, which simply costs time. The scanning speed cannot be increased unlimitedly, as this would lead to image distortions due to resonances in the microscope, very much like the strong vibrations of some parts of a car when driven at a certain speed. By designing the structure of the STM to be as rigid as possible, I have been able to minimize the problems of the resonances and to create a fast STM, which is a necessity if one wants to image fast surface processes during deposition or erosion. The calculations required in the design of the fast STM, which allows its user to record several images per second with atomic resolution, are discussed in Chapter 3.

I have used the new STM to perform research on a specific thin film system: molybdenum-silicon[*] multilayer mirrors. These structures consist of alternating Mo and Si layers of a few nm thick and are used as mirrors for extreme ultraviolet (EUV) light[†]. Mo-Si multilayer optics are used in the newest machines that produce computer chips, for which EUV light is used. The multilayer coating is produced by depositing a Si layer, then on top of that a layer of Mo, followed by another Si layer, etcetera, to a total of typically 100 layers. In order to achieve the best possible reflection of a multilayer mirror, the boundaries between the layers must be as sharp and smooth as possible. In practice though, the boundaries are not very sharp, because during deposition an additional layer is formed between the Mo and Si layers, in the form of a Mo-Si alloy. The interfaces between the layers are also not very smooth, because the deposition of each layer leaves a rough surface. The problems of alloying and roughness formation are larger when Mo is deposited onto Si, than in the reverse case. Therefore, to ultimately improve the performance of Mo-Si multilayer optics, I have concentrated on the deposition of Mo onto a Si substrate.

---

[*]Molybdenum (Mo) is a strong metal with a very high melting temperature. It is used for example as one of the elements of high-strength steel. Silicon (Si) is a semiconductor, of which the most important application is its use in computer chips that are largely made of this material. The contrast in density between Mo and Si - Mo being the denser material - is important for the functioning of Mo-Si multilayer mirrors.

[†]The wavelength of EUV light is much smaller than that of visible light and is just above that of X-ray radiation.

In Chapter 4 an STM study of the initial stages of Mo deposition onto Si is presented. The STM movie that I recorded with the new STM, shows how the Mo reacts with the Si atoms of the substrate to form the Mo-Si alloy. I found that the transport of Si atoms to deposited Mo atoms is an important part of the reaction mechanism. If this transport could be blocked somehow, the Mo-Si alloy interlayer would be thinner and the performance of the mirror would be better. The results allow me to speculate how to block the transport of Si atoms.

After the initial stage, with the alloy formation, the deposition of Mo was not stopped and I continued recording images of the surface of the Mo film that was forming. The analysis and the conclusions that I could draw on the basis of the STM movie that I obtained, are given in Chapter 5. The movie shows how the growing Mo film develops a rough surface during the deposition. The film consists of a very large number of connected Mo crystalline grains. Per mm^2 there are about 60 billion grains in the Mo film. Once a single atom is deposited onto the surface of the growing film, it can move around a bit, but it cannot move away from the grain on which it landed. The consequence is that height differences that arise between grains[*], cannot be reduced by the transport of atoms from the higher to the lower grain. By supplying more energy to the Mo atoms, for example by mildly bombarding the surface with ions at the right moment during deposition, the transport could be activated and the surface of the Mo film would be much smoother.

Chapter 6 is devoted to a very special experiment. I used the new STM to image a Si substrate while bombarding it with ions. To my knowledge this is the very first experiment where the eroding effect of ion bombardment was studied with an STM *during* the process. The STM movie shows how the Si surface erodes, ion-impact after ion-impact. I found that not all incoming ions actually damage the substrate. Those parts of the surface that are undamaged, act as a mirror for the incoming ions. Simultaneously, if an ion strikes the surface at a region that is already heavily damaged, additional damage is done. As a consequence, material is not removed equally fast everywhere, which leads to the formation of a nanometer-sized pattern in the Si surface.

Using what I had learned from the ion erosion experiment of Chapter 6, I applied the technique of ion bombarding and simultaneous STM imaging to a study of the effect of ion erosion of a thin Mo film, in order to see if ion bombardment could be applied for post-deposition smoothing. This investigation is the subject of Chapter 7. I found that the roughness of the film can be greatly reduced, if the ions strike the film at grazing incidence. If this 'ion shaving' would be implemented in the production process of Mo-Si multilayer mirrors, it would probably increase the reflectivity of the mirrors.

---

[*]Not all grains are equally high, as, simply by chance, some regions receive more Mo atoms than other regions.

Samenvatting (voor de leek)

In dit proefschrift beschrijf ik het onderzoek dat ik heb verricht naar enkele processen die belangrijk zijn voor de productie van dunne films. Een laagje materiaal wordt een dunne film genoemd, als de dikte in de orde van nanometers (nm) tot en met micrometers (μm) is*. In ons dagelijks leven spelen dunne films een zeer belangrijke rol. Het verzilveren van een sieraad is een voorbeeld van het aanbrengen van een dunne film. Dunne films vinden we terug op ontspiegelde brillenglazen, in computerchips en in tal van andere toepassingen.

Een dunne film wordt meestal gemaakt door materiaal te deponeren op een substraat. De depositiemethode die ik heb gebruikt, heet thermische depositie. Bij deze methode wordt het te deponeren materiaal, bijvoorbeeld in de vorm van een staafje of een schijf, zodanig verhit dat het gedeeltelijk verdampt en losse atomen of kleine clusters van atomen het hete oppervlak verlaten. Het substraat is zodanig geplaatst dat sommige van de afgedampte atomen erop landen. Wanneer een atoom op het substraat arriveert, is het vaak eerst nog behoorlijk beweeglijk. Het atoom beweegt over het oppervlak en gaat bindingen aan met andere atomen en zo worden clusters gevormd. Een cluster groeit doordat nieuwe atomen gedeponeerd worden op het cluster of doordat atomen die tussen clusters gedeponeerd worden, diffunderen naar het cluster, waaraan ze zich binden. Op het moment dat de clusters zo groot zijn dat zij elkaar raken en het hele substraat bedekken, is de film gesloten. Door verder te deponeren kan een film van de gewenste dikte gefabriceerd worden.

De procesparameters van de depositie, bijvoorbeeld de depositiesnelheid en de temperatuur van het substraat (deze is van invloed op de beweeglijkheid van de atomen) bepalen de vorm en de textuur van de film: zijn morfologie. Deze

---

*Een μm is gelijk aan 0,001 mm; een nm komt overeen met 0,000001 mm.

is sterk bepalend voor de eigenschappen en toepasbaarheid van de film. De elektrische geleidbaarheid, de sterkte van de film en zijn optische reflectiviteit zijn voorbeelden van filmeigenschappen die afhangen van de morfologie[*]. Door het depositieproces aan te passen kan men dus, via de morfologie, de eigenschappen van een film optimaliseren.

De filmmorfologie kan niet alleen tijdens de depositie, maar ook erna worden veranderd. Een manier om dat te doen is door een film te bombarderen met geladen deeltjes: ionen. Door een ionenbombardement worden de atomen in de film door elkaar gehusseld en meestal worden ook atomen van het oppervlak van de film weggeschoten, hetgeen sputteren wordt genoemd. Net als met het depositieproces kan ook het ionenbombardement worden geoptimaliseerd. Men kan bijvoorbeeld de massa van de ionen variëren of de kracht waarmee de ionen inslaan. Ook de invalshoek van de ionen speelt een zeer belangrijke rol.

Om de gewenste film te produceren zijn er dus heel wat parameters die kunnen worden geoptimaliseerd, hetgeen kan geschieden door simpelweg een parameter te variëren en vervolgens vast te stellen of de filmeigenschappen zijn verbeterd of verslechterd. Deze *trial-and-error* manier kan goed werken, maar wordt erg ingewikkeld als er meerdere parameters, die meestal niet onafhankelijk zijn, moeten worden geoptimaliseerd. Er is echter ook een andere aanpak, welke de motivatie vormt voor mijn onderzoek. Door op een fundamenteel niveau te begrijpen hoe de verschillende processen tijdens de fabricage van een film zijn morfologie beïnvloeden, kan het productieproces gericht en dus zeer effectief worden verbeterd, zodat uiteindelijk de ultieme dunne film, voor de gewenste toepassing, kan worden gemaakt.

Het instrument dat ik tijdens mijn onderzoek heb gebruikt om materiaaldepositie en ionenbombardement te bestuderen, is een bijzondere microscoop waarmee de bouwstenen van een film, de atomen, zichtbaar kunnen worden gemaakt[†]. Ik heb gewerkt met een rastertunnelmicroscoop (Engels: *scanning tunneling microscope, STM*). Een STM heeft een zeer scherpe naaldvormige punt, waarmee het oppervlak wordt afgetast en de atomen als 'hobbeltjes' in het oppervlak worden waargenomen. Een afbeelding wordt gemaakt door lijn voor lijn het oppervlak af te tasten en het zo in kaart te brengen.

Een STM is zeer geschikt om materiaaldepositie en ionenbombardement op atomair niveau te onderzoeken, maar er kleeft een groot nadeel aan het gebruik van een dergelijk microscoop voor dit type onderzoek. Met een standaard STM-opstelling is het onmogelijk, of in ieder geval extreem moeilijk, een film te deponeren of te modificeren met ionenbombardement en tegelijkertijd met de STM

---

[*]Beschouw als voorbeeld van het belang van de filmmorfologie voor de toepasbaarheid van een film een dunne metaalfilm, die wordt gebruikt als spiegel. Voor de hoogste reflectiviteit dient het oppervlak van de film zo vlak mogelijk zijn.

[†]Met een 'gewone' microscoop, een lichtmicroscoop, kunnen geen atomen zichtbaar gemaakt worden. De afstand tussen twee naburige atomen in een vaste stof is typisch 0.3 nm, terwijl het oplossend vermogen van de beste lichtmicroscoop rond de 200 nm ligt.

de veranderende filmstructuur in beeld te brengen. Bijna alle STM-studies van depositie en ionenbombardement zijn uitgevoerd *nadat* de film vervaardigd was, waardoor een direct inzicht in de verschillende processen die leiden tot een specifieke filmmorfologie ontbreekt. Om in staat te zijn deze processen *live* te kunnen volgen, met atomaire resolutie, was het ontwikkelen van een bijzondere STM een onderdeel van mijn promotieonderzoek. In hoofdstuk 2 van dit proefschrift wordt de nieuwe microscoop gepresenteerd.

Een nadeel van de manier waarop een STM werkt, is dat het vrij veel tijd kost om een enkele afbeelding te verkrijgen. Een opnametijd van enkele minuten is geen uitzondering. Lijn voor lijn wordt de naald over het oppervlak bewogen en de snelheid waarmee dat gebeurt, is beperkt. Het te snel bewegen van de naald over het oppervlak gaat gepaard met het heftig trillen van bepaalde onderdelen van de microscoop. Dit is te vergelijken met het resoneren van onderdelen van een auto, wanneer deze met een bepaalde snelheid rijdt. Als tijdens het meten met de STM de trillingen zo groot worden dat de naald het oppervlak niet meer goed kan volgen, resulteert dit in aanzienlijke beeldvervorming. De nieuwe STM is zo ontworpen dat het probleem van de resonanties geminimaliseerd is, en dat het mogelijk is met de microscoop meerdere afbeeldingen per seconde op te nemen. De berekeningen die nodig waren voor het ontwerpen van de snelle STM, zijn het onderwerp van hoofdstuk 3.

Na de opbouw van de nieuwe STM heb ik deze gebruikt om een specifiek systeem van dunne films te bestuderen: zogenaamde molybdeen-silicium* multilaag-coatings. Typisch bestaan deze coatings uit 100 lagen van afwisselend Mo en Si. Een enkele laag is slechts een paar nm dik. Deze Mo-Si multilaag-structuren worden toegepast als spiegel voor extreem-ultraviolet (EUV) licht†. EUV-spiegels worden gebruikt in de nieuwste machines die computerchips produceren. Een Mo-Si multilaagspiegel wordt geproduceerd door eerst een dunne Si-film te deponeren, daarna een Mo-film, gevolgd door weer een Si-film, enzovoort. De reflectiviteit van de resulterende spiegel hangt af van hoe scherp en vlak de overgangen tussen de Mo- en Si-lagen zijn en daar zitten stevige beperkingen aan. Tijdens de depositie van een nieuwe laag op een laag die net gedeponeerd is, wordt een Mo-Si legering gevormd. Dit resulteert in een ongewenste tussenlaag. Daarnaast is een gedeponeerde laag behoorlijk ruw. Hierdoor is het grensvlak met de volgende laag niet vlak. De negatieve effecten van de Mo-Si legering en van de ruwheidsontwikkeling zijn het grootst wanneer Mo op Si wordt gedeponeerd; andersom gaat het beter. Daarom heb ik met de nieuwe STM de atomaire processen bestudeerd tijdens de depositie van Mo op een Si-substraat.

In hoofdstuk 4 wordt een studie gepresenteerd van de eerste fases van Mo deposi-

---

*Molybdeen (Mo) is een sterk metaal met een zeer hoog smeltpunt, dat o.a. gebruikt wordt in versterkt staal. Silicium (Si) is een halfgeleider, waarvan de belangrijkste toepassing het gebruik in computerchips is. De dichtheid van Mo is aanzienlijk hoger dan die van Si. Dit contrast is belangrijk voor Mo-Si multilaagspiegels.

†De golflengte van EUV-licht is veel kleiner dan die van zichtbaar licht en net groter dan die van Röntgenstraling.

tie op Si. De STM-opnames die ik heb gemaakt, laten zien hoe het gedeponeerde Mo reageert met de Si-atomen en hoe de Mo-Si legering wordt gevormd. De mobiliteit van de Si-atomen blijkt een belangrijke rol te spelen in de vorming van de legering. Als dit transport zou kunnen worden geblokkeerd of bemoeilijkt, zou de ongewenste tussenlaag dunner zijn. Door mijn metingen ben ik in staat te speculeren hoe het transport van Si-atomen verhinderd zou kunnen worden.

Na de fase waarin de Mo-Si legering wordt gevormd, heb ik de depositie voortgezet om te onderzoeken hoe de morfologie van de Mo-film zich ontwikkelt. Deze studie is het onderwerp van hoofdstuk 5. Ik heb een STM-opname gemaakt waarin in detail te zien is hoe de ruwheid van de film ontstaat. De Mo-film is een netwerk van een zeer groot aantal, aaneengesloten, zeer kleine Mo-kristallieten, ook wel korrels genoemd. Per mm^2 zijn er ongeveer 60 miljard van deze korrels in de Mo-film. Wanneer een Mo-atoom op een bepaalde korrel arriveert, zal het eerst nog wat bewegen, maar het is zo goed als uitgesloten dat het atoom naar een naburige korrel diffundeert. Hierdoor kunnen hoogteverschillen die tussen korrels ontstaan* niet worden verkleind door het transport van Mo-atomen van een hoge naar een lage korrel. Als tijdens de depositie de Mo-atomen meer energie zouden hebben, zouden de atomen wel in staat zijn over te steken naar een andere korrel en zou de film aanzienlijk vlakker zijn. Dit zou bijvoorbeeld bereikt kunnen worden door op het juiste moment het oppervlak te bombarderen met ionen, zodat de Mo-atomen net het laatste zetje krijgen.

Hoofdstuk 6 is gewijd aan een bijzonder experiment. Ik heb de nieuwe STM gebruikt om een Si-substraat te bestuderen, terwijl het werd gebombardeerd met ionen. Voor zover mij bekend is dit het eerste experiment waar het effect van een ionenbombardement *tijdens* het proces is vastgelegd met een STM. In de STM-opname is te zien hoe het oppervlak door de ene na de andere inslag erodeert. Ik heb kunnen vaststellen dat niet alle ionen in het oppervlak inslaan. Als de baan van een ion uitkomt op een onbeschadigd deel van het oppervlak, wordt het ion gereflecteerd en beschadigt het het oppervlak dus niet. Als een ion uitkomt bij een reeds beschadigd deel van het oppervlak, volgt wel een succesvolle inslag. Omdat het oppervlak dus niet gelijkmatig erodeert, ontstaat een interessant patroon in het Si-oppervlak.

Ik heb de techniek van gelijktijdig meten en bombarderen vervolgens toegepast om het effect van een ionenbombardement op een gedeponeerde Mo-film te bestuderen. Dit is het onderwerp van hoofdstuk 7. Ik wilde onderzoeken, of een dergelijke behandeling het oppervlak van de film vlakker zou kunnen maken. Zo vond ik, dat ik de ruwheid van de film aanzienlijk kon verkleinen, wanneer ik de hoek van de baan van de ionen en het oppervlak van de film klein maakte (scherende inval). Als deze techniek zou worden geïmplementeerd in het productieproces van Mo-Si multilaagsspiegels, zou dat de reflectiviteit van de spiegels hoogstwaarschijnlijk ten goede komen.

---

*Niet alle korrels zijn even hoog, doordat, door toeval, op sommige plaatsen meer atomen landen dan op andere.

Nawoord

In 2006 was travee 'West 10' in het Kamerlingh Onnes Laboratorium in Leiden een lege plek; het gat in de vloer herinnerde nog aan de cryostaat die er had gestaan. Nu staat er op die plek een zelfgebouwde opstelling, een bijzondere microscoop, gevat in een imposante vacuümkamer, omgeven door een keur aan regel- en meetelektronica, en andere apparatuur. Zonder de bijdrage van velen zou die opstelling daar nu niet hebben gestaan en zou ik de experimenten die ik ermee gedaan heb, niet hebben kunnen uitvoeren.

Zeer belangrijk was de ondersteuning vanuit de fijnmechanische dienst. In eerste instantie maakte Arjen Geluk de werktekeningen, bedacht slimme oplossingen voor tal van kleine problemen die we onderweg tegenkwamen, en produceerde de eerste componenten van de microscoop. Zijn werk werd later overgenomen door Gijsbert Verdoes, die tevens betrokken was bij de opbouw van de opstelling in het laboratorium. Ook Fred Schenkel, Ruud van Egmond en Ewie de Kuyper hebben met hun kennis en kunde op het gebied van de fijnmechanica bijgedragen aan de totstandkoming van de experimentele opstelling.

Voor de ontwikkeling van nieuwe elektronica, en verbeteringen en reparaties van allerhande apparatuur kon ik rekenen op Peter Schakel, Bert Crama, René Overgauw, Raymond Koehler, Ton Tampung en Co Janmaat. Als een van de computers kuren vertoonde, was Fred Kranenburg altijd in staat snel een oplossing te bieden.

In het begin van mijn promotieonderzoek werkte ik samen met Mark den Heijer, die in het kader van zijn afstudeerstage bij het project was betrokken. Mark werkte mee aan het ontwerpen van het hart van de opstelling, de snelle STM-scankop, waarvoor hij de *eindige-elementenmethode* toepaste om het optimale

ontwerp te berekenen. Dit werk vormt de basis van hoofdstuk 3. Ook vond Mark uit hoe we de piezo-elektrische naderingsmotoren van de STM het beste konden aansturen. Het karakteriseren van de STM-scankop met de *vibrometer* deden we bij de TU Delft (*Delft Center for Systems and Control*) met de hulp van Georg Schitter, die thans verbonden is aan de TU Wenen.

Mijn promotieonderzoek was gevat in een STW-project waarbij ik samenwerkte met Erwin Zoethout, Eric Louis en Fred Bijkerk van het FOM-Instituut voor Plasmafysica Rijnhuizen, alwaar onderzoek wordt gedaan naar multilaagspiegels, zoals die worden toegepast in de nieuwste lithografiemachines van ASML. Bij mijn onderzoek heb ik heb veel profijt gehad van hun expertise.

De discussies met vakgroepsgenoten resulteerden vaak in de oplossingen voor de technische problemen die ik tegenkwam en gaven mij dikwijls de juiste richting voor het aanpakken van wetenschappelijke vraagstukken. Zo heb ik van Guocai Dong geleerd hoe ik het silicium-preparaat schoon kon krijgen en waren de discussies met Dirk van Baarle zeer waardevol voor de analyse van de data van het ionenerosie-experiment, beschreven in hoofdstuk 6.

Ik heb bij mijn experimenten gebruik gemaakt van de regel- en meetelektronica van Leiden Probe Microscopy (LPM). Dankzij Gertjan van Baarle verliep de integratie van de LPM-elektronica in de nieuwe opstelling nagenoeg vlekkeloos.

Als laatste wil ik graag de bijdrage van Jan Verhoeven noemen. Hij hielp mij bij het 'sleutelen' aan de vacuümkamer, waarbij ik kon profiteren van zijn ervaring met ultrahoog-vacuüm. Na de opbouwfase kon ik rekenen op zijn uitgebreide kennis op het gebied van multilaagstructuren. In de vele gesprekken die we hebben gevoerd over de experimenten en de interpretatie van de data, kwamen we al discussiërend vaak tot interessante inzichten.

Curriculum vitae

Vincent Fokkema is geboren in Vlaardingen op 16 januari 1982. In 2000 rondde hij de gymnasiumopleiding van scholengemeenschap Spieringshoek in Schiedam af, waarna hij natuurkunde ging studeren aan de Universiteit Leiden. In 2006 studeerde hij af in de experimentele natuurkunde, waarvoor hij twee onderzoeksprojecten deed. Het eerste onderzoek betrof de ontwikkeling van een lage temperaturen NMR-opstelling onder begeleiding van dr. R. Jochemsen. Voor het tweede onderzoek werkte hij onder supervisie van prof. dr. ir. T. H. Oosterkamp en dr. ir. W. M. van Spengen met een atomaire-krachtmicroscoop (AFM), die hij ook gebruikte als wrijvingsmicroscoop (FFM). Hij onderzocht de capillaire condensatie van water tussen de *tip* van de microscoop en het oppervlak tijdens AFM/FFM metingen. Na zijn afstuderen begon hij zijn promotieonderzoek aan de Universiteit Leiden in het Kamerlingh Onnes Laboratorium als lid van de *Interface Physics* vakgroep van prof. dr. J. W. M. Frenken onder directe begeleiding van dr. M. J. Rost. Het onderzoek dat hij heeft verricht, staat beschreven in dit proefschrift.

References

[1] H. Lüth, *Solid surfaces, interfaces and thin films* (Springer, 2010), 5th ed.

[2] H. A. Macleod, *Thin-film optical filters* (CRC Press, Taylor & Francis Group, 2010), 4th ed.

[3] D. S. Stone, K. B. Yoder, and W. D. Sproul, J. Vac. Sci. Technol. A **9**, 2543 (1991).

[4] C.-K. Hu and J. M. E. Harper, Mater. Chem. Phys. **52**, 5 (1998).

[5] J. S. Moodera, L. R. Kinder, T. M. Wong, and R. Meservey, Phys. Rev. Lett. **74**, 3273 (1995).

[6] D. M. Mattox, *Handbook of physical vapor deposition (PVD) processing* (Elsevier, 2010), 2nd ed.

[7] Y. D. Gamburg and G. Zangari, *Theory and practice of metal electrodeposition* (Springer, 2011).

[8] Y. Xu and X.-T. Yan, *Chemical vapour deposition - an integrated engineering design for advanced materials* (Springer, 2010).

[9] G. Dhanaraj, K. Byrappa, V. Prasad, and M. Dudley (Eds.), *Springer handbook of crystal growth* (Springer, 2010).

[10] B. A. Movchan and A. V. Demchishin, Fiz. Met. Metalloved. **28**, 83 (1969).

[11] J. A. Thornton, Annu. Rev. Mater. Sci. **7**, 239 (1977).

[12] C. V. Thompson, Annu. Rev. Mater. Sci. **30**, 159 (2000).

[13] I. Petrov, P. B. Barna, L. Hulltman, and J. E. Greene, J. Vac. Sci. Technol. A **21**, S117 (2003).

[14] M. J. Rost, D. A. Quist, and J. W. M. Frenken, Phys. Rev. Lett. **91**, 026101 (2003).

[15] G. Carter, J. Phys. D: Appl. Phys. **31**, R1 (2001).

[16] H. J. Levinson, *Principles of lithography* (SPIE Press, 2010), 3rd ed.

[17] EUV lithography machine NXE:3100 from ASML offers a resolution of 27 nm. NXE:3300B is due 2012 with a resolution of 22 nm (http://www.asml.com).

[18] The Mo-Si multilayer optics for the EUV lithography machines of ASML are produced by Carl Zeiss AG.

[19] S. Yulin, in *Extreme ultraviolet lithography*, edited by B. Wu and A. Kumar (McGraw Hill, 2009), p. 225.

[20] O. S. Heavens, *Optical properties of thin solid films* (Dover, 1965).

[21] Z. Knittl, *Optics of thin films (an optical multilayer theory)* (Wiley, 1976).

[22] B. L. Henke, E. M. Gullikson, and J. C. Davis, Atomic data and nuclear data tables **54**, 181 (1993).

[23] The center for X-ray optics, Lawrence Berkeley National Laboratory (http://henke.lbl.gov/optical_constants).

[24] E. Spiller, Rev. Phys. Appl. **23**, 1687 (1988).

[25] D. G. Stearns, D. P. Gaines, D. W. Sweeney, and E. M. Gullikson, J. Appl. Phys. **84**, 1003 (1998).

[26] G. Binnig, H. Rohrer, C. Gerber, and E. Weibel, Appl. Phys. Lett. **40**, 178 (1982).

[27] G. Binnig, H. Rohrer, C. Gerber, and E. Weibel, Phys. Rev. Lett. **49**, 59 (1982).

[28] http://www.nobelprize.org.

[29] M. J. Rost, L. Crama, P. Schakel, E. van Tol, G. B. E. M. van Velzen-Williams, C. F. Overgauw, H. ter Horst, H. Dekker, B. Okhuijsen, M. Seynen, A. Vijftigschild, P. Han, A. J. Katan, K. Schoots, R. Schumm, W. van Loo, T. H. Oosterkamp, and J. W. M. Frenken, Rev. Sci. Instrum. **75**, 053710 (2005).

[30] Examples of companies selling scanning probe microscopes: JEOL Ltd., Leiden Probe Microscopy B.V., Omicron NanoTechnology GmbH, RHK Technology, and SPECS Surface Nano Analysis GmbH.

[31] M. Bott, T. Michely, and G. Comsa, Rev. Sci. Instrum. **66**, 4135 (1995).

[32] M. S. Hoogeman, D. Glastra van Loon, R. W. M. Loos, H. G. Ficke, E. de Haas, J. J. van der Linden, H. Zeijlemaker, L. Kuipers, M. F. Chang, M. A. J. Klik, and J. W. M. Frenken, Rev. Sci. Instrum. **69**, 2072 (1998).

[33] S. H. Pan, E. W. Hudson, and J. C. Davis, Rev. Sci. Instrum. **70**, 1459 (1999).

[34] M. Morgenstern, A. Schwarz, and U. D. Schwarz, in *Nanotribology and nanomechanics*, edited by B. Bhushan (Springer, 2005), pp. 185–242.

[35] P. B. Rasmussen, B. L. M. Hendriksen, H. Zeijlemaker, H. H. Ficke, and J. W. M. Frenken, Rev. Sci. Instrum. **69**, 3879 (1998).

[36] R. Sonnenfeld and P. K. Hansma, Science **232**, 211 (1986).

[37] H.-Y. Liu, F.-R. F. Fan, C. W. Lin, and A. Bard, J. Am. Chem. Soc. **108**, 3838 (1986).

[38] B. Voigtländer and A. Zinner, Appl. Phys. Lett. **63**, 3055 (1993).

[39] B. Voigtländer, Surf. Sci. Rep. **43**, 127 (2001).

[40] M. J. Rost, Phys. Rev. Lett. **99**, 266101 (2007).

[41] G. Schitter and M. J. Rost, Materials Today **11**, 40 (2008).

[42] L. Petersen, M. Schunack, B. Schaefer, T. R. Linderoth, P. B. Rasmussen, P. T. Sprunger, E. Laegsgaard, I. Stensgaard, and F. Besenbacher, Rev. Sci. Instrum. **72**, 1438 (2001).

[43] W. Allers, A. Schwarz, U. D. Schwarz, and R. Wiesendanger, Appl. Surf. Sci. **140**, 247 (1999).

[44] C. J. Chen, *Introduction to scanning tunneling microscopy* (Oxford University Press, 1993).

[45] G. Binnig and D. P. E. Smith, Rev. Sci. Instrum. **57**, 1688 (1986).

[46] M. J. Rost, G. J. C. van Baarle, A. J. Katan, W. M. van Spengen, P. Schakel, W. A. van Loo, T. H. Oosterkamp, and J. W. M. Frenken, Asian J. of Control **11**, 110 (2009).

[47] Leiden Probe Microscopy B.V. (http://www.leidenprobemicroscopy.com).

[48] A. D. L. Humphris, M. J. Miles, and J. K. Hobbs, Appl. Phys. Lett. **86**, 034106 (2005).

[49] EBL Products Inc. (http://www.eblproducts.com).

[50] Piezo LEGS® Linear, vacuum version from PiezoMotor AB.

[51] M. den Heijer, *Towards the ultimate STM; design, modelling and characterization* (2008), MSc thesis, Leiden University, The Netherlands.

[52] Piezo LEGS® Rotary, vacuum version from PiezoMotor AB.

[53] The UHV chamber was designed at the Kamerlingh Onnes Laboratory and manufactured by VG Scienta.

[54] Stabilizer I-2000 pneumatic isolators with automatic re-leveling from Newport Corporation.

[55] TMU 200 MP (pumping speed for N_2 180 l/s) from Pfeiffer Vacuum.

[56] VacIon Starcell® (pumping speed 300 l/s) from Varian Inc., now part of Agilent Technologies.

[57] Home-built (not at the Kamerlingh Onnes Laboratory) cryo-shield, with a 3 Ti filament insert from Balzers.

[58] UHV-24p with W filaments from Varian Inc., now part of Agilent Technologies.

[59] QMS 112 (with QMA 120 analyser) from Balzers.

[60] Custom made flexible isolating bake-out tent from TEVAC Surface Science Technology; heater fan from Tectra GmbH.

[61] A. Stupnik and M. Leisch, Vacuum **81**, 748 (2007).

[62] EGCO4 mini e-beam evaporator from Oxford Applied Research.

[63] IQ100 ion source with Wien-filter from Kremer Vakuumphysik GmbH.

[64] Navitar Zoom 7000 with $2\times$ focal length extender and USB camera from Edmund Optics.

[65] LPM Video Rate STM Control Electronics from Leiden Probe Microscopy B.V., operated in conjunction with a home-built low-noise 3 channel driver for the coarse approach motors.

[66] Rear View LEED/AES system from VG Microtech.

[67] Ultrastat from Oxford Instruments.

[68] J. H. Kindt, G. E. Fantner, J. A. Cutroni, and P. K. Hansma, Ultramicroscopy **100**, 259 (2004).

[69] Q. Sun and R. A. Wolkow, Rev. Sci. Instrum. **77**, 113701 (2006).

[70] C. R. Ast, M. Assig, A. Ast, and K. Kern, Rev. Sci. Instrum. **79**, 093704 (2008).

[71] K.-J. Bathe, *Finite element procedures in engineering analysis* (Prentice-Hall, Inc., 1982).

[72] R. W. Clough and J. Penzien, *Dynamics of structures* (Computers & Structures, Inc., 1995), 3rd ed.

[73] O. C. Zienkiewicz and R. L. Taylor, *The finite element method for solid and structural mechanics* (Elsevier Butterworth-Heinemann, 2005), 6th ed.

[74] Lord Rayleigh, *Theory of sound* (Dover, 1877).

[75] B. J. Lazan, *Damping of materials and members in structural mechanics* (Pergamon Press, 1968), 1st ed.

[76] W. Duffy, Jr., Physica B **169**, 463 (1991).

[77] COMSOL, multiphysics modelling and simulation software, version 3.3.

[78] CAD drawings were exported from Autodesk Inventor, several versions.

[79] *IEEE standard definitions and methods of measurement for piezoelectric vibrators*, IEEE standard 177, 1966.

[80] G. Binnig, H. Rohrer, C. Gerber, and E. Weibel, Phys. Rev. Lett. **50**, 120 (1983).

[81] MSA-500 laser Doppler vibrometer from Polytec.

[82] G. E. Fantner, P. Hegarty, J. H. Kindt, G. Schitter, G. A. G. Cidade, and P. K. Hansma, Rev. Sci. Instrum. **76**, 026118 (2005).

[83] E. C. M. Disseldorp, F. C. Tabak, A. J. Katan, M. S. B. Hesselberth, T. H. Oosterkamp, J. W. M. Frenken, and W. M. van Spengen, Rev. Sci. Instrum. **81**, 043702 (2010).

[84] T. Ando, N. Kodera, E. Takai, D. Maruyama, K. Saito, and A. Toda, Proc. Natl. Acad. Sci. **98**, 12468 (2001).

[85] A. K. Petford-Long, M. B. Stearns, C.-H. Chang, S. R. Nutt, D. G. Stearns, N. M. Ceglio, and A. M. Hawryluk, J. Appl. Phys. **61**, 1422 (1987).

[86] K. Holloway, K. B. Do, and R. Sinclair, J. Appl. Phys. **65**, 474 (1989).

[87] D. G. Stearns, M. B. Stearns, Y. Cheng, J. H. Stith, and N. M. Ceglio, J. Appl. Phys. **67**, 2415 (1990).

[88] M. B. Stearns, C.-H. Chang, and D. G. Stearns, J. Appl. Phys. **71**, 187 (1992).

[89] D. L. Windt, R. Hull, and W. K. Waskiewicz, J. Appl. Phys. **71**, 2677 (1992).

[90] S. Yulin, T. Feigl, T. Kuhlmann, N. Kaiser, A. I. Fedorenko, V. V. Kondratenko, O. V. Poltseva, V. A. Sevryukova, A. Yu. Zolotaryov, and E. N. Zubarev, J. Appl. Phys. **92**, 1216 (2002).

[91] J. A. Venables, Surf. Sci. **299**, 798 (1994).

[92] H. Brune, Surf. Sci. Rep. **31**, 121 (1998).

[93] J. A. Venables, P. A. Bennett, H. Brune, J. Drucker, and J. H. Harding, Phil. Trans. R. Soc. Lond. A **361**, 311 (2003).

[94] P. A. Bennett and H. von Känel, J. Phys. D: Appl. Phys. **32**, R71 (1999).

[95] A. H. Reader, A. H. van Ommen, P. J. W. Weijs, R. A. M. Wolters, and D. J. Oostra, Rep. Prog. Phys. **56**, 1397 (1992).

[96] A. Hiraki, Surf. Sci. Rep. **3**, 357 (1984).

[97] E. J. van Loenen, J. F. van der Veen, and F. K. LeGoues, Surf. Sci. **157**, 1 (1985).

[98] P. A. Bennett, D. G. Cahill, and M. Copel, Phys. Rev. Lett. **73**, 452 (1994).

[99] J. Alvarez, A. L. V. de Parga, J. J. Hinarejos, J. de la Figuera, E. G. Michel, C. Ocal, and R. Miranda, Phys. Rev. B **47**, 16048 (1993).

[100] K. N. Tu, Appl. Phys. Lett. **27**, 221 (1975).

[101] P. J. Bedrossian, Surf. Sci. **320**, 247 (1994).

[102] E. Chi, J. Shim, J. Kwak, and H. Baik, J. Mat. Sci. **31**, 3567 (1996).

[103] J. M. Slaughter, A. Shapiro, P. A. Kearney, and C. M. Falco, Phys. Rev. B **44**, 3854 (1991).

[104] P. J. Bedrossian, Surf. Sci. **322**, 73 (1995).

[105] K. Takayanagi, Y. Tansihiro, M. Takahashi, and S. Takahashi, J. Vac. Sci. Technol. A **3**, 1502 (1985).

[106] R. J. Hamers, R. M. Tromp, and J. E. Demuth, Phys. Rev. Lett. **56**, 1972 (1986).

[107] F. J. Giessibl, Science **267**, 68 (1995).

[108] F. J. Giessibl, S. Hembacher, H. Bielefeldt, and J. Mannhart, Science **289**, 422 (2000).

[109] Y.-L. Wang, H.-M. Guo, Z.-H. Qin, H.-F. Ma, and H.-J. Gao, J. Nanomaterials **2008**, 874213 (2008).

[110] The STM movie is available as supplementary material: **movie1**. The movie plays 16 times faster than the rate at which it was recorded. In the movie, the deposition starts after 8 s.

[111] The STM movie is available as supplementary material: **movie2**. The movie plays 30 times faster than the rate at which it was recorded.

[112] Q. Jiang, J. C. Li, and B. Q. Chi, Chem. Phys. Lett. **366**, 551 (2001).

[113] A. Guivarc'h, P. Auvray, L. Berthou, M. L. Cun, J. P. Boulet, P. Henoc, G. Pelous, and A. Martinez, J. Appl. Phys. **49**, 233 (1978).

[114] T. H. McDaniels, J. A. Venables, and P. A. Bennett, Phys. Rev. Lett. **87**, 176105 (2001).

[115] E. Zoethout (FOM Institute for Plasma Physics Rijnhuizen), private communication.

[116] D.-E. Kim, S.-M. Lee, I.-J. Jeon, and M. Yanagihara, Appl. Surf. Sci. **127**, 531 (1998).

[117] S. Braun, R. Dietsch, M. Haidl, T. Holz, H. Mai, S. Müllender, and R. Scholz, Microelec. Eng. **57**, 9 (2001).

[118] V. I. T. A. de Rooij-Lohmann, A. E. Yakshin, E. Zoethout, J. Verhoeven, and F. Bijkerk, Appl. Surf. Sci. **257**, 6251 (2011).

[119] T. Young, Phil. Trans. R. Soc. Lond. **95**, 65 (1805).

[120] B. C. Allen, J. Less-Common Metals **17**, 403 (1969).

[121] W. R. Tyson and W. A. Miller, Surf. Sci. **62**, 267 (1977).

[122] S. Hara, S. Izumi, T. Kumagai, and S. Sakai, Surf. Sci. **585**, 17 (2005).

[123] X. Fan and T. Ishigaki, J. Crystal Growth **171**, 166 (1997).

[124] S. Bajt, J. B. Alameda, T. W. Barbee, J. A. Folta, B. Kaufmann, and E. A. Spiller, Opt. Eng. **41**, 1797 (2002).

[125] S. Braun, H. Mai, M. Moss, R. Scholz, and A. Leson, Jpn. J. Appl. Phys. **41**, 4074 (2002).

[126] I. Nedelcu, R. W. E. van de Kruijs, A. E. Yakshin, and F. Bijkerk, Appl. Opt. **48**, 155 (2009).

[127] R. Schlatmann, J. D. Schindler, and J. Verhoeven, Phys. Rev. B **54**, 10880 (2002).

[128] J. Verhoeven, *Engineering of surfaces and interfaces using low energy ions* (2005), PhD thesis, Eindhoven University of Technology, The Netherlands.

[129] R. Schlatmann, C. Lu, J. Verhoeven, E. J. Puik, and M. J. van der Wiel, Appl. Surf. Sci. **78**, 147 (1994).

[130] R. W. E. van de Kruijs, E. Zoethout, A. E. Yakshin, I. Nedelcu, E. Louis, G. Enkisch, G. Sipos, S. Müllender, and F. Bijkerk, Thin Solid Films **515**, 430 (2006).

[131] S. Bajt, D. G. Stearns, and P. A. Kearney, J. Appl. Phys. **90**, 1017 (2001).

[132] A. Fillon, G. Abadias, A. Michel, C. Jaouen, and P. Villechaise, Phys. Rev. Lett. **104**, 096101 (2010).

[133] C. Polop, C. Rosiepen, S. Bleikamp, R. Drese, J. Mayer, A. Dimyati, and T. Michely, New J. Phys. **9**, 74 (2007).

[134] E. Spiller, A. Segmüller, J. Rife, and R.-P. Haelbich, Appl. Phys. Lett. **37**, 1048 (1980).

[135] P. Meakin, *Fractals, scaling and growth far from equilibrium* (Cambridge University Press, 1998).

[136] G. Palasantzas and J. Krim, Phys. Rev. B **48**, 2873 (1993).

[137] G. Palasantzas, Phys. Rev. B **48**, 14472 (1993).

[138] Y.-P. Zhao, H.-N. Yang, G.-C. Wang, and T.-M. Lu, Phys. Rev. B **58**, 1922 (1998).

[139] T. Michely and J. Krug, *Islands, mounds and atoms: patterns and processes in crystal growth far from equilibrium* (Springer-Verlag, 2004).

[140] A.-L. Barabási and H. E. Stanley, *Fractal concepts in surface growth* (Cambridge University Press, 1995).

[141] C. Herring, J. Appl. Phys. **21**, 301 (1950).

[142] W. W. Mullins, J. Appl. Phys. **30**, 77 (1959).

[143] M. Kardar, G. Parisi, and Y.-C. Zhang, Phys. Rev. Lett. **56**, 889 (1986).

[144] G. Ehrlich and F. G. Hudda, J. Chem. Phys. **44**, 1039 (1966).

[145] R. L. Schwoebel and E. J. Shipsey, J. Appl. Phys. **37**, 3682 (1966).

[146] J. Villain, J. Phys. I **1**, 19 (1990).

[147] J. A. Stroscio, D. T. Pierce, M. D. Stiles, A. Zangwill, and L. M. Sander, Phys. Rev. Lett. **75**, 4246 (1995).

[148] M. Siegert and M. Plischke, Phys. Rev. E **53**, 307 (1996).

[149] L. Golubović, Phys. Rev. Lett. **78**, 90 (1997).

[150] M. Siegert, Phys. Rev. Lett. **81**, 5481 (1998).

[151] J. G. Amar and F. Family, Phys. Rev. Lett. **77**, 4584 (1996).

[152] D. E. Wolf and J. Villain, Europhys. Lett. **13**, 389 (1990).

[153] S. Das Sarma and P. Tamborenea, Phys. Rev. Lett. **66**, 325 (1991).

[154] S. Das Sarma, P. Punyindu, and Z. Toroczkai, Surf. Sci. **457**, L369 (2000).

[155] P. Punyindu Chatraphorn, Z. Toroczkai, and S. Das Sarma, Phys. Rev. B **64**, 205407 (2001).

[156] O. Pierre-Louis, M. R. D'Orsonage, and T. L. Einstein, Phys. Rev. Lett. **82**, 3661 (1999).

[157] N. Néel, T. Maroutian, L. Douillard, and H.-J. Ernst, Phys. Rev. Lett. **77**, 4584 (1996).

[158] The STM movie is available as supplementary material. The movie is divided into two parts for a better colour contrast in either part. The first part shows the growth between a nominal thickness of 0.1 nm and 0.8 nm: **movie3a**. The second part shows the growth between 0.8 and 4.0 nm: **movie3b**. Both movies play 390 times faster than the rate at which the STM movie was recorded.

[159] C. R. M. Grovenor, H. T. G. Hentzell, and D. A. Smith, Acta Metall. **32**, 773 (1984).

[160] J. M. López, M. A. Rodriguez, and R. Cuerno, Phys. Rev. E **56**, 3993 (1997).

[161] M. Giesen, G. Schulze Icking-Konert, and H. Ibach, Phys. Rev. Lett. **80**, 552 (1998).

[162] M. Giesen, G. Schulze Icking-Konert, and H. Ibach, Phys. Rev. Lett. **82**, 3101 (1999).

[163] M. Giesen and H. Ibach, Surf. Sci. **464**, L697 (2000).

[164] K. Morgenstern, G. Rosenfeld, G. Comsa, M. R. Sørensen, B. Hammer, E. Laegsgaard, and F. Besenbacher, Phys. Rev. B **63**, 045412 (2001).

[165] M. I. Larsson, Phys. Rev. B **64**, 115428 (2001).

[166] J. W. Evans, D. E. Sanders, P. A. Thiel, and A. E. DePristo, Phys. Rev. B **41**, 5410 (1990).

[167] J. W. Evans, Phys. Rev. B **43**, 3897 (1991).

[168] J. Yu and J. G. Amar, Phys. Rev. B **69**, 045426 (2004).

[169] R. Stumpf and M. Scheffler, Phys. Rev. Lett. **72**, 254 (1994).

[170] S. C. Wang and G. Ehrlich, Phys. Rev. Lett. **75**, 2964 (1995).

[171] G. Ehrlich, Surf. Sci. **331**, 865 (1995).

[172] W. T. Read and W. Shokley, Phys. Rev. **78**, 275 (1950).

[173] H. van Swygenhoven, D. Farkas, and A. Caro, Phys. Rev. B **62**, 831 (2000).

[174] L. S. Shvindlerman and B. B. Straumal, Acta Metall. **33**, 1735 (1985).

[175] V. Randle, Scripta Mater. **54**, 1011 (2005).

[176] E. V. Albano, R. C. Salvarezza, L. Vázquez, and A. J. Arvia, Phys. Rev. B **59**, 7354 (1999).

[177] S. Das Sarma, S. V. Ghaisas, and J. M. Kim, Phys. Rev. E **49**, 122 (1994).

[178] J. M. López, Phys. Rev. Lett. **83**, 4594 (1999).

[179] A. S. Mata, S. C. Ferreira, Jr., I. R. B. Ribeiro, and S. O. Ferreira, Phys. Rev. B **78**, 115305 (2008).

[180] C. V. Thompson, Annu. Rev. Mater. Sci. **20**, 245 (1990).

[181] J. E. Burke and D. Turnbull, Prog. Metal Phys. **3**, 220 (1952).

[182] H. V. Atkinson, Acta Metall. **36**, 469 (1969).

[183] M. Hillert, Acta Metall. **13**, 227 (1965).

[184] E. Zoethout, V. Fokkema, E. Louis, F. Bijkerk, J. W. M. Frenken, and M. J. Rost (to be published).

[185] I. Nedelcu, R. W. E. van de Kruijs, A. E. Yakshin, and F. Bijkerk, J. Appl. Phys. **103**, 083549 (2008).

[186] E. Spiller, Appl. Phys. Lett. **54**, 2293 (1989).

[187] T. Chassé, H. Neumann, and B. Rauschenbach, Nuclear Inst. and Meth. in Phys. Research B **206**, 377 (2003).

[188] TEM sample preparation tips from FEI Company (http://www.fei.com).

[189] F. Frost, R. Fechner, B. Ziberi, J. Völlner, D. Flamm, and A. Schindler, J. Phys.: Condens. Matter **21**, 224026 (2009).

[190] S. P. Wolsky, Phys. Rev. **108**, 1131 (1957).

[191] M. V. R. Murty, T. Curcic, A. Judy, B. H. Cooper, A. R. Woll, J. D. Brock, S. Kycia, and R. L. Headrick, Phys. Rev. Lett. **80**, 4713 (1998).

[192] B. Poelsema, L. K. Verheij, and G. Comsa, Phys. Rev. Lett. **53**, 2500 (1984).

[193] K. G. Nakamura and M. Kitajima, J. Appl. Phys. **71**, 3645 (1992).

[194] T. Michely and G. Comsa, Nuclear Inst. and Meth. in Phys. Research B **82**, 207 (1993).

[195] J. Erlebacher, M. J. Aziz, E. Chason, M. B. Sinclair, and J. A. Floro, Phys. Rev. Lett. **82**, 2330 (1999).

[196] S. Facsko, T. Dekorsy, C. Koerdt, C. Trappe, H. Kurz, A. Vogt, and H. L. Hartnagel, Science **285**, 1551 (1999).

[197] U. Valbussa, C. Boragno, and F. B. de Mongeot, J. Phys.: Condens. Matter **14**, 8153 (2002).

[198] W. L. Chan and E. Chason, J. Appl. Phys. **101**, 121301 (2007).

[199] A 2D and a 3D version of the STM movie are available as supplementary material: **movie4a** and **movie4b**. Both versions play 110 times faster than the rate at which the movie was recorded.

[200] H. Niehus, W. Heiland, and E. Taglauer, Surf. Sci. Reports **17**, 213 (1993).

[201] H. Hansen, C. Polop, and T. Michely, Phys. Rev. Lett. **92**, 246106 (2004).

[202] T. Michely and G. Comsa, Phys. Rev. B **44**, 8411 (1991).

[203] K. Cho and E. Kaxiras, Europhys. Lett. **39**, 287 (1997).

[204] T. Sato, S. Kitamura, and M. Iwatsuki, J. Vac. Sci. Technol. A **18**, 960 (2000).

[205] R. M. Bradley and J. M. E. Harper, J. Vac. Sci. Technol. A **6**, 2390 (1988).

[206] P. Sigmund, Phys. Rev. **184**, 383 (1969).

[207] P. Sigmund, J. Mat. Sci. **8**, 1645 (1973).

[208] J. D. Erlebacher, M. J. Aziz, E. Chason, M. B. Sinclair, and J. A. Floro, J. Vac. Sci. Technol. A **18**, 115 (2000).

[209] A.-D. Brown and J. Erlebacher, Phys. Rev. B **72**, 075350 (2005).

[210] J. D. Erlebacher and M. J. Aziz, MRS Symposia Proceedings **440**, 461 (1997).

[211] E. Chason, T. M. Mayer, B. K. Kellerman, D. T. McIlroy, and A. J. Howard, Phys. Rev. Lett. **72**, 3040 (1994).

[212] G. Costantini, F. B. de Mongeot, C. Boragno, and U. Valbusa, Phys. Rev. Lett. **86**, 838 (2001).

[213] S. van Dijken, D. de Bruin, and B. Poelsema, Phys. Rev. Lett. **86**, 4608 (2001).

[214] J.-H. Kim, M. Joe, S.-P. Kim, N.-B. Ha, K.-R. Lee, B. Kahng, and J.-S. Kim, Phys. Rev. B **79**, 205403 (2009).

[215] A. Pimpinelli, J. Villain, D. E. Wolf, J. J. Métois, J. C. Heyraud, I. Elkinani, and G. Uimin, Surf. Sci. **295**, 143 (1993).

[216] A. V. Latyshev, A. B. Krasilnikov, and A. L. Aseev, Phys. Rev. B **54**, 2586 (1996).

[217] H. Hansen, A. Redinger, S. Messlinger, G. Stoian, Y. Rosandi, H. M. Urbassek, U. Linke, and T. Michely, Phys. Rev. B **73**, 235414 (2006).

[218] A. Redinger, H. Hansen, U. Linke, Y. Rosandi, H. M. Urbassek, and T. Michely, Phys. Rev. Lett. **96**, 106103 (2006).

[219] J. F. Ziegler, J. P. Biersack, and M. D. Ziegler, *SRIM, the stopping and range of ions in matter* (James Ziegler, 2008).

[220] E. Zoethout, E. Louis, and F. Bijkerk, (to be published).

[221] J. M. Freitag and B. M. Clemens, J. Appl. Phys. **89**, 1101 (2001).

[222] J. Verhoeven, L. Chunguang, E. J. Puik, M. J. van der Wiel, and T. P. Huijgen, Appl. Surf. Sci. **55**, 97 (1992).

[223] Y. Hasegawa, Y. Fujimoto, and F. Okuyama, Surf. Sci. **163**, L781 (1985).

[224] H. A. Atwater, C. V. Thompson, and H. I. Smith, Phys. Rev. Lett. **60**, 112 (1988).

[225] H. A. Atwater, C. V. Thompson, and H. I. Smith, J. Appl. Phys. **64**, 2337 (1988).

[226] D. E. Alexander and G. S. Was, Phys. Rev. B **47**, 2983 (1993).

[227] G. Carter, Phys. Rev. B **62**, 8376 (2000).

[228] M. Seita, C. M. Pecnik, S. Frank, and R. Spolenak, Acta Mater. **58**, 6513 (2010).

[229] R. P. Webb, *SUSPRE, Surrey university sputter profile resolution from energy deposition, version 2.1.3* (Surrey Ion Beam Centre, 2001).

[230] E. Louis, A. E. Yakshin, P. C. Görts, S. Oestreich, R. Stuik, E. L. G. Maas, M. J. H. Kessels, F. Bijkerk, M. Haidl, S. Müllender, M. Mertin, D. Schmitz, F. Scholze, and G. Ulm, SPIE 3997-44, Microlithography, Santa Clara (2000).

[231] E. Spiller, Opt. Eng. **29**, 609 (1990).

[232] S. A. Barnett, K. C. Ruthe, and P. M. Deluca, Mat. Res. Soc. Symp. Proc. **585**, 91 (2000).

[233] M. Holzwarth, M. Wißing, D. S. Simeonova, S. Tzanev, K. J. Snowdon, and O. I. Yordanov, Surf. Sci. **331**, 1093 (1995).

[234] M. Wißing, M. Batzill, and K. J. Snowdon, Nanotechnology **8**, 40 (1997).

[235] The STM movie is available as supplementary material: **movie5**. The movie plays 760 times faster than the rate at which it was recorded.

[236] W. Ensinger, Surfaces and Coatings Tech. **65**, 90 (1994).

[237] R. Spolenak, L. Sauter, and C. Eberl, Scripta Mater. **53**, 1291 (2005).

[238] R. Spolenak and M. T. Pérez Prado, Scripta Mater. **55**, 103 (2006).

[239] D. Förster, S. Bleikamp, and T. Michely, Thin Solid Films **519**, 598 (2010).

[240] H.-J. Voorma, E. Louis, F. Bijkerk, and S. Abdali, J. Appl. Phys. **82**, 1876 (1997).

[241] B. Ziberi, M. Cornejo, F. Frost, and B. Rauschenbach, J. Phys.: Condens. Matter **21**, 224003 (2009).

[242] S. Macko, F. Frost, B. Ziberi, D. F. Förster, and T. Michely, Nanotechnology **21**, 085301 (2010).

[243] R. Schlatmann, A. Keppel, Y. Xue, J. Verhoeven, and M. J. van der Wiel, Appl. Phys. Lett. **63**, 3297 (1993).